
Chairman: Prof. Dr. Jan Colpaert, Hasselt University

Promoter: Prof. Dr. Tanja Junkers, Hasselt University, Monash University

Copromoter: Prof. Dr. Patrick Wagner, KU Leuven

Members of the Jury: Prof. Dr. Ronald Thoelen, Hasselt University

Prof. Dr. Wanda Guedens, Hasselt University

Prof. Dr. Christophe Detrembleur, Université de Liège

Dr. Alexander Welle, Karlsruhe Institute of Technology

Dr. Jaroslav Mosnáček, Slovak Academy of Sciences

*"The cleverest of all, in my opinion,
is the man who calls himself a fool
at least once a month."*

Fyodor M. Dostoyevsky

Table of Contents

1	Introduction.....	1
1.1	Miniaturization of sensors	2
1.2	Polymer synthesis.....	4
1.2.1	Atom Transfer Radical Polymerization	7
1.2.2	Reversible-addition fragmentation degenerative chain transfer and iniferter polymerization	9
1.3	Surface functionalization and polymer grafting	12
1.3.1	Surface modification using photomediated RDRP	13
1.4	Molecularly imprinted polymers	16
1.5	Sensor set-up	21
1.5.1	Chemical sensors.....	21
1.5.2	Electrical impedance spectroscopy	22
1.6	Step-growth polymerization towards the production of biomaterials	24
1.6.1	Michael addition reactions.....	24
1.6.2	Morita-Baylis-Hillman reactions	25
1.7	Goal and general overview.....	27
1.8	References	29
2	Organocatalyzed Photo-Atom Transfer Radical Polymerization of Methacrylic Acid in Flow Synthesis and Surface Grafting	39
2.1	Abstract	40
2.2	Introduction.....	41

2.3 Experimental Section	45
2.3.1 Synthesis of 10-phenyl(phenothiazine)	45
2.3.2 Synthesis of 11-(trichlorosilyl)undecyl 2-bromo-2-phenylethanoate	45
2.3.3 Metal-free ATRP batch polymerization procedure	46
2.3.4 Metal-free ATRP flow polymerization procedure	46
2.3.5 Metal-free ATRP surface grafting procedure	47
2.4 Results and Discussion	48
2.4.1 Organocatalyzed photoATRP in batch	48
2.4.2 Polymerization in flow	50
2.4.3 Grafting of PMAA brushes	52
2.5 Conclusions	55
2.6 References	57
3 Laser-grafted Molecularly Imprinted Polymers for the Detection of Histamine From Organocatalyzed Atom Transfer Radical Polymerization.....	61
3.1 Abstract	62
3.2 Introduction.....	63
3.3 Experimental Section	68
3.3.1 Electrochemical Impedance Spectroscopy (EIS)	68
3.3.2 Measurement cell	68
3.3.3 Silanization of substrates	69
3.3.4 MIP surface grafting	69
3.4 Results and Discussion	70
3.4.1 Surface grafting of MIPs.	70
3.4.2 Biomimetic measurements.....	74

3.5 Conclusion.....	78
3.6 References	80
4 Photoiniferter surface grafting of poly(methyl acrylate) using xanthates	85
4.1 Introduction	86
4.2 Experimental Section	89
4.2.1 Synthesis of 4-hydroxybutyl 2-bromopropanoate	89
4.2.2 Synthesis of xanthate silane precursor	90
4.2.3 Synthesis of xanthate silane.....	90
4.2.4 Silanization of silicon substrates	91
4.2.5 Surface grafting of poly(methyl acrylate)	92
4.3 Results and Discussion	93
4.4 Conclusion.....	100
4.5 References	101
5 Development of functional polymer resins for two-photon polymerization	105
5.1 Introduction	106
5.2 Experimental Section	110
5.2.1 Synthesis of Bis(dodecylsulfanyl thiocarbonyl)disulfide....	110
5.2.2 Synthesis of CDP-TTC.....	111
5.2.3 Synthesis of PMMA macroRAFT	111

Table of Contents

5.2.4 Production of Microstructures using Two-Photon Polymerization (2PP).....	112
5.2.5 Cell Experiments	113
5.2.6 Post-modification of the Polymers	113
5.3 Results and Discussion	114
5.3.1 Synthesis of PMMA macroRAFT	114
5.3.2 Optimization of resin composition and two-photon polymerization	117
5.3.3 Biocompatibility assays	122
5.3.4 Post-modification	122
5.4 Conclusions	124
5.5 Future outlook	125
5.6 References	126
6 Synthesis of functional polymer particles from Morita-Baylis-Hillman polymerization	129
6.1 Abstract	130
6.2 Introduction.....	131
6.3 Experimental section.....	133
6.3.1 Morita-Baylis-Hillman polymerization (MBH polymerization).....	133
6.3.2 Suspension Polymerization.....	133
6.3.3 Polymer degradation study.....	134
6.3.4 Schiff base modification on particle surfaces.....	134
6.3.5 Cytotoxicity study.....	135
6.4 Results and discussion	136
6.4.1 Morita-Baylis-Hillman polymerization.....	136

6.4.2	Suspension polymerization and polymer degradation	138
6.4.3	Cytotoxicity tests.....	141
6.5	Conclusion.....	143
6.6	References	144
7	Appendix.....	147
7.1	Figures	148
7.2	Tables.....	166
8	Materials & Characterization	169
8.1	Materials	170
8.1.1	Surface grafting	170
8.1.2	Side projects.....	171
8.2	Characterization	172
8.3	References	176
9	Summary & Outlook	177
9.1	Summary	178
9.2	Nederlandse samenvatting.....	181
9.3	Outlook.....	185
	Publications.....	189
	Dankwoord.....	191

List of Abbreviations

^1H NMR	proton nuclear magnetic resonance
2PA	two-photon absorption
2PP	two-photon polymerization
2-VP	2-vinylpyridine
3-HQD	3-hydroquinolidone
AA	acrylic acid
Abs	antibodies
Abs.	absolute
AC	alternating current
ACVA	4,4'-azobis(4- cyanovaleric acid)
AFM	atomic force microscopy
APTES	3-aminopropyltriethoxysilane
at%	atomic percent
ATR	attenuated total reflection
ATRP	atom transfer radical polymerization
CDP-TTC	4-cyano4-[(dodecylsulfanylthiocarbonyl) sulfanyl]pentanoic acid
co	copolymer

List of Abbreviations

CTA	chain transfer agent
DABCO	1,4-diazabicyclo[2.2.2]octane
DC	direct current
DCM	dichloromethane
DLW	direct laser writing
DMAc	dimethylacetamide
DMAP	4-dimethylaminopyridine
DMSO	dimethylsulfoxide
<i>DP</i>	degree of polymerization
DVB	divinylbenzene
<i>D</i>	dispersity
EBPA	ethyl 2-bromo-2-phenylacetate
ECM	extracellular matrix
EDC	1-ethyl-3-(3-dimethylaminopropyl)carbodiimide
EDTA	ethylenediaminetetraacetic acid
EIS	electrical impedance spectroscopy
EGDMA	ethylene glycol dimethacrylate
Eq.	equivalent
ESI-MS	electrospray ionization mass spectrometry
EtOH	ethanol

FTIR	Fourier transform infrared
GAATR-IR	grazing angle attenuated total reflection infrared
GM	Göppert-Meyer
GPC	gel permeability chromatography
HDDA	hexanediol diacrylate
HTM	heat transfer method
HUVEC	human umbilical vein endothelial cell
I	initiator
IR	infrared
LCST	lower critical solution temperature
LED	light-emitting diode
MAA	methacrylic acid
MBH	Morita-Baylis-Hillman
MeOH	methanol
MIP	molecularly imprinted polymer
M_n	number average molecular weight
M_w	weight average molecular weight
MWD	molecular weight distribution
NIP	non-imprinted polymer
NMP	nitroxide mediated radical polymerization

List of Abbreviations

O-ATRP	organocatalyzed atom transfer radical polymerization
PBS	phosphate buffer saline
PC	photocatalyst
PEEK	polyether ether ketone
PEGA	poly(ethylene glycol) methyl ether acrylate
PETMP	pentaerythriol tetrakis(3-mercaptopropionate)
PET-RAFT	photoinduced electron transfer reversible-addition fragmentation degenerative chain transfer
PID	proportional-integral-derivative
PFA	perfluoroalkoxy alkanes
PMA	poly(methyl acrylate)
PMAA	poly(methacrylic acid)
PMMA	poly(methyl methacrylate)
ppb	parts per billion
ppm	parts per million
PSF	porcine skin fibroblast
PTH	10-phenyl(phenothiazine)
PVA	poly(vinyl alcohol)
QCM	quartz crystal microbalance

RAFT	reversible–addition fragmentation degenerative chain transfer
RDRP	reversible deactivation radical polymerization
RGD	arginylglycylaspartic acid
SAM	self-assembled monolayer
SEC	size exclusion chromatography
SEM	scanning electron microscopy
SPR	surface plasmon resonance
SI-ARGET-ATRP	surface initiated activators regenerated by electron transfer atom transfer radical polymerization
TA	terephthalaldehyde
TEA	triethylamine
TEGDA	tetra(ethylene glycol) diacrylate
THF	tetrahydrofuran
ToF-SIMS	time-of-flight secondary ion mass spectrometry
TRIM	trimethylolpropane trimethacrylate
TTC	trithiocarbonate
UV	ultraviolet
WCA	water contact angle
XPS	x-ray photoelectron spectroscopy

List of figures

Figure 1.1.	Schematic representation of a chain-growth and step-growth polymerization	4
Figure 1.2.	Molecular weight vs conversion plot.....	6
Figure 1.3.	Mechanism of classical ATRP.....	7
Figure 1.4.	Mechanism of PhotoRDRP.....	8
Figure 1.5.	Mechanism of O-ATRP.....	9
Figure 1.6.	Mechanism of RAFT polymerization.....	10
Figure 1.7.	Schematic representation of using a shadow mask or direct laser writing	12
Figure 1.8.	Surface initiated RDRP.....	14
Figure 1.9.	Schematic representation of a MIP	16
Figure 1.10.	Schematic representation of a surface grown MIP.....	19
Figure 1.11.	General chemical sensor set-up.....	21
Figure 1.12.	Randles cell.....	22
Figure 1.13.	Bode plot.....	23
Figure 1.14.	Mechanism of Michael addition.....	25
Figure 1.15	Mechanism for Morita-Baylis-Hillman reaction	26
Figure 2.1.	M_n vs conversion plot for PMMA using O-ATRP.....	49
Figure 2.2.	M_n vs conversion plot of MAA using O-ATRP in flow	51
Figure 2.3.	ToF-SIMS and XPS spectra confirming the presence of methacrylic acid	53

Figure 2.4.	AFM scratch test of PMAA brushes	54
Figure 3.1.	Schematic representation of the MIP sensor production	67
Figure 3.2.	IR spectra of grafted P(MAA- <i>co</i> -EGDMA).....	71
Figure 3.3.	ToF-SIMS spectra of grafted P(MAA- <i>co</i> -EGDMA).....	73
Figure 3.4.	Bode plot of a MIP sensor measurement.....	76
Figure 3.5.	Dose-response curve of the MIP and NIP sensors	77
Figure 4.1.	Schematic representation of photoiniferter mechanism	88
Figure 4.2.	ToF-SIMS of immobilized xanthates and grafted PMA	94
Figure 4.3.	XPS spectra of PMA grafted sample	95
Figure 4.4.	Plots displaying the evolution of the carbonyl vibration at 1740 cm ⁻¹ (grazing angle FTIR).....	97
Figure 4.5.	AFM images of the scratch of PMA grafted wafers	98
Figure 5.1.	Jablonksi diagram	107
Figure 5.2.	Schematic representation of photoRAFT in 2PP.....	110
Figure 5.3.	Molecular weight vs conversion plot using Blue light initiated photoRAFT polymerization of MMA.....	115
Figure 5.4.	ESI-MS spectrum displaying a distribution of PMMA .	116
Figure 5.5.	Microscopy images of 2PP optimization array	117
Figure 5.6.	Profilometer analysis of the parameter array test	119
Figure 5.7.	SEM image of printed structures and EDX mapping ..	121
Figure 5.8.	Optical microscopy image taken from cross array subjected to cell studies.....	122
Figure 5.9.	ATR-IR spectra of modified polymer structures.....	123

Figure 6.1. Schematic representation of MBH polymerization.....132

Figure 6.2. SEC elugrams of MBH polymers137

Figure 6.3. Degradation study of MBH particles139

Figure 6.4. FTIR spectra comparing MBH particles before and
after modification.....140

Figure 6.5. Cytotoxicity test of MBH particles142

Chapter 1

Introduction

1.1 Miniaturization of sensors

“There’s plenty of room at the bottom”. Just like the desire to get to the moon in the 1960’s, modern science has its mind set on a challenge. Similar to 50 years ago it has its effect on society, though without a cramped political situation on the matter. Almost every person with sufficiently working senses noticed the downsizing of technologies. The famous quote by Richard Feynman in 1959 motivated scientists and companies to make devices as small as possible, sometimes beyond practicality. Is it necessary to make a smartphone almost as flat as a piece of paper, making it less comfortable to handle? Of course this expertise can be picked up for relevant applications in the near future. Despite the phone being flat, it contains many sensors to provide detailed information on your physiological status and has much more computing power than was required to get to the moon in 1969.

This reduction of volume also worked its way into the medical field. Implants are for example equipped with nanoscopic (nanometer = 10^{-9} meter) features to improve compatibility with the host tissue. Equipping these nano- and microscopic structures with smart features, might allow clinicians to obtain real-time information on the patient’s progress. This would be comparable to the smartphone example given earlier, where a miniaturized integrated sensor provides (chemical) information. The use of these so-called *in vivo* sensors would be an enormous step forward as it would enable clinicians to follow concentration fluctuations of biomarkers and thereby facilitate clinical studies and theragnostics.

Nowadays, biological receptors are often used for the detection of biological analytes. In most cases antibodies (Abs) are employed which can be developed to target a selected analyte in a very specific manner. However, drawbacks of working with biomolecules are their limited shelf-life and issues regarding their survival in harsh environmental conditions. Furthermore, the production of Abs

can be costly.^[1,2] As an alternative, molecularly imprinted polymers (MIPs) or synthetic Abs, can be considered. They have comparable specificity, but do not suffer from the listed drawbacks. To be able to miniaturize these so-called MIP sensors, control over their synthesis is desirable in means of temporal and spatial control. This would allow for the production of sensitive polymeric features, produced in complex patterns, sometimes within the nanoscale. Its production is, however, accompanied by several challenges. To understand this we have to know how polymers are made, how MIPs function and how this control can be achieved.

The goal of this thesis is therefore to develop a synthesis route which overcomes these challenges. This can be achieved by the surface-growing of polymerfilms from the surface of a substrate using a light source to mediate the reaction. Ultimately these synthesis procedures are optimized to produce MIP films, which are tested in a sensor set-up.

1.2 Polymer synthesis

Polymers, or macromolecules, are made of smaller repeating units called monomers, linked together by a so-called polymerization reaction. Polymers can be found in nature, where the best-known examples are DNA, polysaccharides and proteins. Alternatively, synthetic polymers reside in plastics, electronics and a vast variety of industrial products such as adhesives and coatings.^[3]

Polymerization reactions can be divided into two main classes, namely step-growth and chain-growth polymerization. This division is based on the reaction mechanics and is depicted in **Figure 1.1**. In a step-growth polymerization, monomers are linked through reaction of their functional moieties in a step wise fashion, without requiring an initiator. This means that from monomers dimers are formed, two dimers form tetramers while a monomer and dimer form trimers and so on. These combinations gradually combine into larger macromolecules. This takes place at a relatively slow pace due to the fact that high conversions are required to obtain high molecular weight polymers. No monomers or large polymers can coexist.

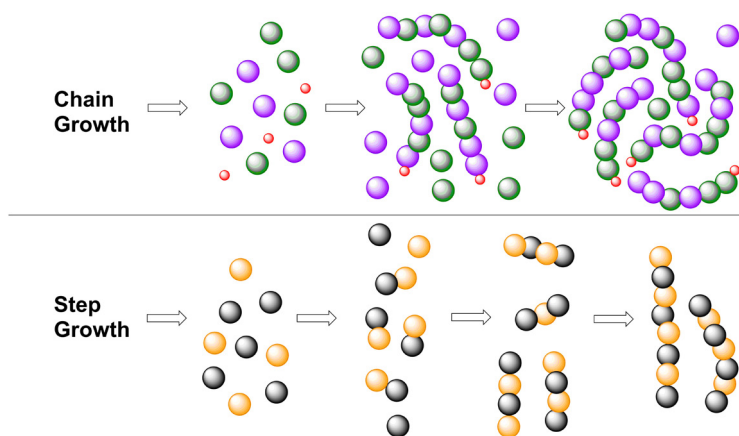


Figure 1.1. Schematic representation of a chain-growth (Top) and step-growth polymerization (bottom)

In a chain-growth polymerization, monomers are linked together by adding to a growing polymer chain, one by one. Following an "initiation" step with the formation of the reactive center, monomers are linked to the reactive center. Chain-growth methods include radical, cationic, anionic or ring-opening metathesis polymerization. After addition of the monomer to the growing chain, the reactive center is regenerated on the newly added monomer, making it available for another monomer addition. This step is better known as "propagation". Following this mechanistic pathway, high molecular weight polymers are obtained at low conversions and only polymers and monomers can be found in the reaction mixture (next to initiator fragments). Propagation is ceased via "termination" events, which proceed via recombination of radicals or disproportionation for radical polymerization. Ionic polymerizations are terminated by chain-breaking events or by combination with a counter ion. Since only radical chain-growth polymerization is addressed in this thesis, this route will be discussed further.

Unlike in free radical polymerization where high molecular weight polymers are produced at the first instance, in some radical chain-growth pathways the number average molecular weight (M_n) is linearly increasing with conversion. This is achieved by suppressing termination events or by reversible transfer reactions. Hereby, the apparent lifetime of the radical is prolonged. Such reactions are better known as reversible deactivation radical polymerizations (RDRP). An RDRP is additionally characterized by a narrow molecular weight distribution (which requires fast initiation) and high end-group fidelity. The evolution of molecular weight with increasing conversion for step-growth and chain-growth (free radical and RDRP) polymerizations is displayed in **Figure 1.2**.

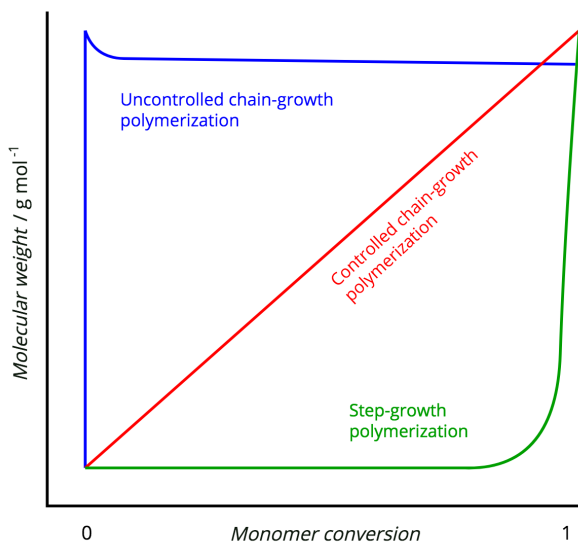


Figure 1.2. Molecular weight vs conversion plot for step-growth, controlled and uncontrolled chain-growth polymerization.

Some of the best known RDRPs are atom transfer radical polymerization (ATRP),^[4,5] reversible-addition fragmentation degenerative chain transfer (RAFT) polymerization^[6] and iniferter polymerization.^[7] These techniques are separately discussed in the next sections.

Depending on the polymerization strategy, different modes of initiation can be considered. While initially thermolysis (RAFT) and redox initiation (ATRP) were the conventional activation routes, photomediation of controlled radical polymerization has been explored with increasing attention.^[8] Photoinitiation has the advantage of providing good spatial and temporal control while allowing mild reaction conditions. The developments in photoinitiation with respect to RAFT and ATRP are touched upon in their respective sections.

1.2.1 Atom Transfer Radical Polymerization

Sawamoto^[4] and coworkers and Matyjaszewski and coworkers^[5] first described ATRP in 1995. The general mechanism of classical ATRP according to Matyjaszewski is depicted in **Figure 1.3**.^[9]

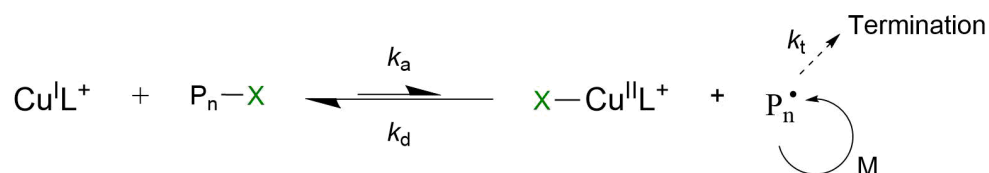


Figure 1.3. Simplified mechanism of classical ATRP.

Radicals are generated through the activation of a so-called ATRP initiator or activator. Typically, an ATRP initiator is equipped with a halide, which is kept in a redox equilibrium with a metal/ligand complex. Such a complex often comprises a cuprous halide, but other metal complexes are reported as well.^[4,10,11] The metal catalyst is kept in solution through complexation with the ligand often consisting of (tertiary) amines. Activation of the initiator is achieved through extraction and reversible transfer of the halide from the initiator to the metal/ligand complex. This yields a radical species, which can undergo propagation. The termination events in this case are suppressed by favoring the dormant or inactive state in the redox equilibrium, through the addition of the persistent copper halide radical or deactivator. Because of this mechanism, all polymers are allowed to grow at the same pace, which results in a linear increase in the number average molecular weight with increasing monomer conversion.

A limitation of classical ATRP is the rather limited pool of compatible monomers. These limitations and challenges arise from interaction with the ligand through competition (amines) and protonation (acids). Furthermore, purification steps are required to remove any remaining metal contamination.

With the introduction of photo-induced ATRP^[10,12] these challenges were addressed. Light exposure contributes to the regeneration of the copper(I) species (activator) and therefore stimulates polymerization. This is suggested to be achieved by exciting the metal/ligand complex. Free ligand, which is added in excess compared to the copper(II) species will act as a reducing agent, generating copper(I). Additionally, multiple other pathways were suggested to contribute to the reduction of the catalyst as proposed in **Figure 1.4**.^[13] This way the copper concentrations can be drastically reduced to levels below 100 ppm.^[14-16]

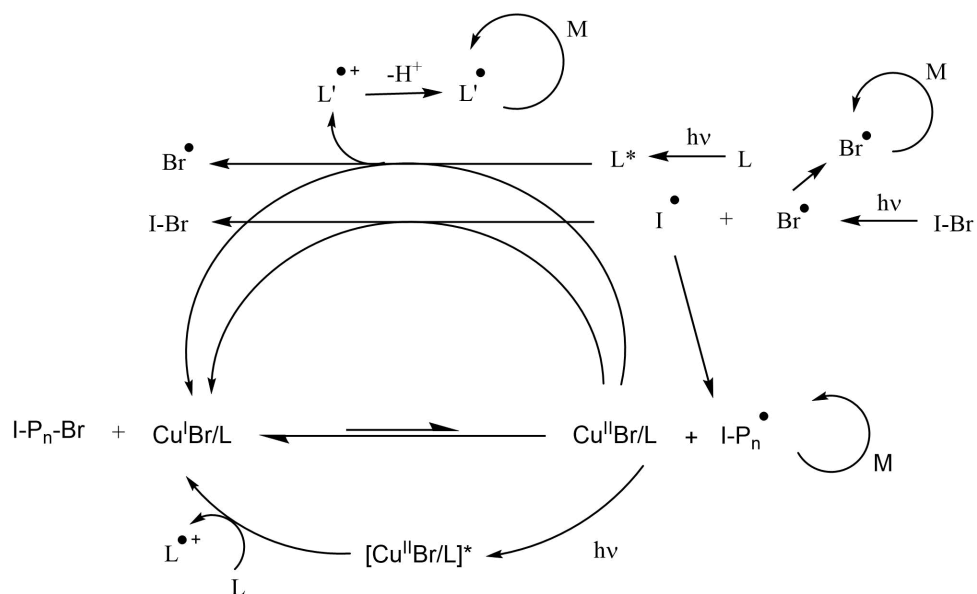


Figure 1.4. Mechanism of PhotoRDRP as proposed by Frick *et al.*^[13]

Eventually organocatalysts were introduced for the catalysis of photochemical ATRP reactions also known as O-ATRP.^[17-20] This made the use of metal catalyst and their concomitant ligands redundant. A suitable organo photocatalyst (PC)

is an excellent reductor in excited state. After reducing the alkyl halide and thus activating radical propagation, the obtained radical cation can efficiently oxidize the propagating chain back to a dormant state (**Figure 1.5**).^[21,22] This reversible behavior is usually confirmed and visualized via cyclic voltammetry.^[22,23]

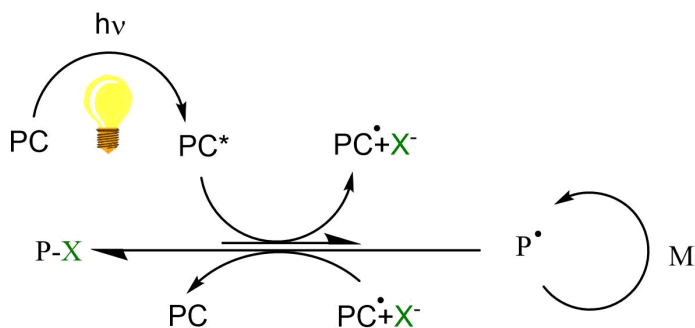


Figure 1.5. Mechanism of O-ATRP.^[22]

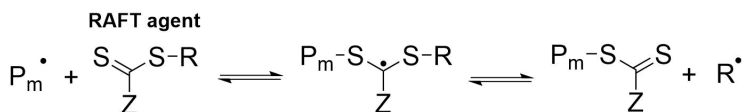
1.2.2 Reversible-addition fragmentation degenerative chain transfer and iniferter polymerization

Another RDRP procedure is RAFT polymerization.^[6] Its mechanism is depicted in **Figure 1.6**. With the aid of a so-called RAFT agent, the radical is reversibly transferred and distributed between an excessive number of dormant chains. The radical source is in this case a conventional radical initiator, as often used in free radical polymerization. After initiation, the radical of the propagating chain adds to the RAFT agent forming an intermediate radical species, entering the pre-equilibrium. Subsequently this species fragments, allowing reinitiation via the radical R-group stemming from the RAFT agent. Herewith, the reaction proceeds to the main RAFT equilibrium where dormant polymer chains are reactivated through continuous reversible activation.

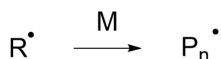
Initiation



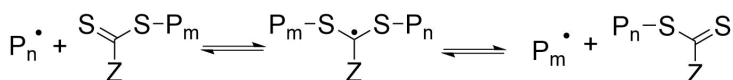
Pre equilibrium



Reinitiation



Main equilibrium



Termination



Figure 1.6. Mechanism of RAFT polymerization.

The composition of the RAFT agent plays a significant role in the success of the reaction, which is determined by a narrow dispersity, high end-group fidelity and narrow molecular weight distributions. It generally consists of a dithioester moiety, R-group and Z-group. In an ideal case the radical is equally stabilized at the propagating polymer chain and the intermediate dithioester specimen ($K = 1$). This allows for easy and quick transfer and therefore rapid deactivation. The stabilization of the radical on the R-group similarly determines the monomer compatibility of the specific RAFT agent. The further chemical nature of the R-group can be selected to have a specific function as end-groups of the RAFT polymers. The Z-group furthermore stabilizes the intermediate radical species and

has an influence on the transfer event. Control over the polymerization reaction is obtained by using an excess of RAFT agent compared to radical initiator. By maximizing chain transfer, termination is, although the same as for a free radical polymerization, at a negligible rate compared to the rate of transfer. For RAFT the degree of polymerization is determined by the monomer and RAFT agent concentration.

To photoinitiate a RAFT polymerization, the photostability of the RAFT agent must be considered, making this a challenging combination as RAFT agents absorb in the UV-vis range and may decompose upon light exposure. When using an additional photoinitiator to perform photoRAFT, the absorption spectra of the initiator and thiocarbonylthio compound should preferably not overlap to avoid decomposition of the RAFT agent. A more direct approach is to use the RAFT agent directly as the main radical source. This strategy is better known as photoiniferter where the RAFT agent serves as the *initiator*, *transfer* agent and *terminating* agent. After initiation, which follows a reversible deactivation mechanism, the intact transfer agents control the polymerization through degenerative transfer similar to RAFT. This is valid if the decomposition of the RAFT agent is within limits to preserve the RAFT control mechanism. Photoiniferter is considered the first reported successful photoRDRP reaction and is therefore a predecessor of RAFT.^[24]

Another option to circumvent the photolability of the RAFT agent is by using photoinduced electron transfer RAFT (PET-RAFT).^[25] In this method, a photoredox catalyst, comparable to those used for photoATRP, is used to initiate the reaction. The excitation spectrum can be shifted by selecting a catalyst whose absorption spectrum has minimal overlap with the absorption range of the RAFT agent. Undesired decomposition of the transfer agent can then be avoided.

1.3 Surface functionalization and polymer grafting

Lithography is the method to produce patterns on substrates. Micropatterns can be generated via a variety of specialized techniques. Several examples are Dip-pen nanolithography, micro-contact printing and interference lithography, but there are many more.^[26] In photolithography, patterns are generated upon light irradiation. Photomasks are mostly employed for the production of polymer patterns.^[27,28] The photomasks cast a shadow on the substrate. Polymerization is only driven in the illuminated regions, creating the negative pattern of the casted shadow, as depicted in **Figure 1.7**. The opposite is also possible when a positive photoresist is used. In that case the light is destructive for the resist, leaving the non-illuminated areas intact.

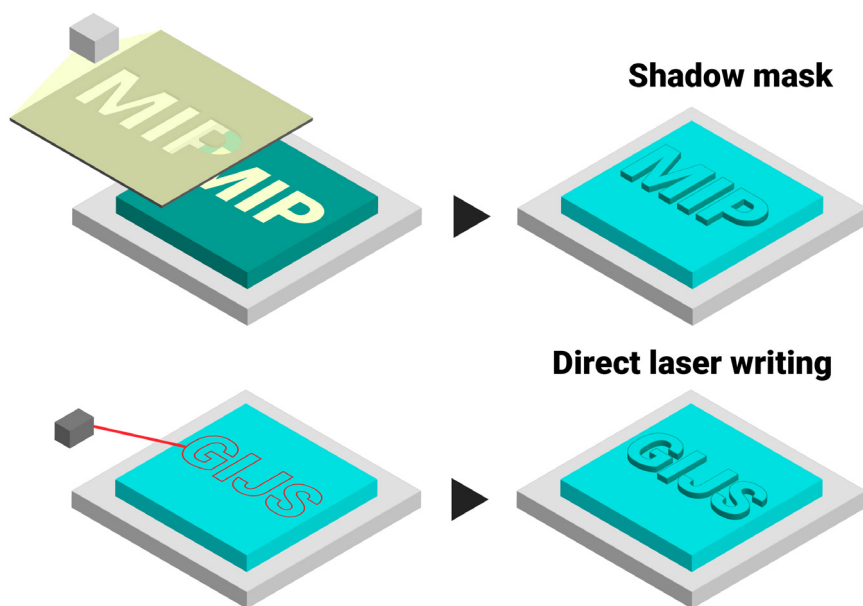


Figure 1.7. Schematic representation of the generation of polymer patterns using a shadow mask (top) or direct laser writing (bottom).

When applying greyscale photomasks, different regions are exposed to varying light intensities. In this way, a local variation in film thickness can be introduced to the polymer film.^[29] When applying photomasks the resolution is heavily depending on the resolution limitations for the fabrication of the mask. Additionally, for different patterns, different masks need to be made, which can be quite tedious. An alternative is provided by directly writing a pattern on the substrate, as illustrated in **Figure 1.7**.^[30] Laun *et al.* reported the direct laser writing (DLW) for copper mediated photoATRP where a pulsed UV laser (351 nm) was used to produce computer generated motives (checkerboard).^[31] Here the resolution was limited to optical effects. A film thickness of up to 39 nm was observed.

All methods discussed in this thesis are “grafting-from” approaches, where polymers are directly grown from a substrate. In the “grafting-to” approach polymers are synthesized prior to grafting. Although better control and easier characterization of the polymerization is obtained for the latter, grafting densities are low due to steric hindrance. To properly assess to which extent surface polymerization is controlled in a grafting-from approach, polymers are often cleaved off and analyzed via size exclusion chromatography (SEC).^[32]

1.3.1 Surface modification using photomediated RDRP

RDRP strategies are investigated for surface modifications with increasing interest.^[33] The advantages of RDRPs, like control over brush size and end-group fidelity can then also be applied to surfaces, as schematically displayed in **Figure 1.8**. Thermal RDRP are mainly conducted for surface modification using RAFT. The photolabile RAFT groups avoid irradiation in the process.^[34] Thermal RAFT is, however, a popular route for the grafting from non-planar substrates, where spatial control is less important or where light irradiation is less homogenous.^[34-36] For planar substrates the reports about photomediated RDRP greatly outnumber thermal initiated routes.^[33] In this approach the advantages of photoinitiation and

controlled polymer brush formation is combined.^[37] It allows for the grafting of complex polymer patterns in three dimensions and by controlling the film thickness predetermined profiles can be obtained through spatial and temporal control. Layered polymer films can be constructed with each layer displaying distinctive properties with the production of (block) copolymers.

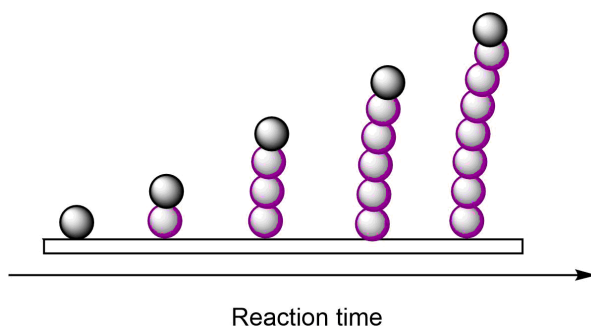


Figure 1.8. Schematic presentation of surface initiated RDRP, providing good over end-group fidelity and control over brush size.

The first surface initiated copper mediated photoATRP was reported in 2013. The ATRP initiator was immobilized through the formation of a self assembled monolayer (SAM) on a gold substrate using thiol end-groups. TiO_2 was added as photosensitizer for the UV initiated reaction. Brush lengths of more than 200 nm were reported.^[38] As generally the case with the formation of SAMs, a long alkyl spacer (around 12 carbons) was preferred to stabilize the monolayer formation.^[39] Without using a sensitizer, PMMA films were grafted up to 15 nm film thickness within 5 hours of exposure time, using a household fluorescent lamp.^[40] Interestingly, gradual evolution and optimization of this technique showed the continuous reduction in copper catalyst concentrations, down to ppb levels.^[27,41] Also with respect to surface grafting, O-ATRP was conducted. Hawker and coworkers reported the grafting of PMMA (up to 30 nm) with 10-phenyl phenothiazine as the catalyst using a 405 nm conical lamp and sunlight.^[28] This work was elaborated by

the group of Matyjaszewski, who compared efficiency between two different ATRP initiators for the polymerization of PMMA from silica particles.^[42] They confirm that ethyl 2-bromo-2-phenylacetate (EBPA) is most suitable for grafting methacrylates.

When using photoRAFT, the RAFT agent can be immobilized via the Z- or R-group.^[33,34] To ensure direct surface grafting, immobilizing the R-group is in most cases the better strategy since radicals, and thus propagation chains, are kept on the surface. However, the additional radical initiator is in this case always added in solution, which automatically enables polymerization in solution. A third option is to attach the initiator to the surface. Here brush length and concomitant film thickness are greatly depending on the RAFT agent concentration, which is in this case preferably low.^[43]

A more direct approach is photoinitiated photo-iniferter, which was already reported in 1996, when triblock copolymers could be grafted from polymer substrates using dithiocarbamates.^[44,45] Until recently, dithiocarbamates were the established iniferters concerning surface initiated polymer grafting. In 2018 surface initiated photoiniferter was reported using trithiocarbonates immobilized on nanoparticles.^[46]

1.4 Molecularly imprinted polymers

Molecularly imprinted polymers (MIPs), also known as synthetic Abs, are synthetic receptor elements (**Figure 1.9**).^[47] Its concept is based on the lock and key model where a template molecule fits the specific molecular lock, represented by the MIP. The binding of specific molecules makes it a suitable structure for a variety of applications such as solid phase extraction, (wastewater) purification,^[48-50] affinity chromatography^[51,52] and sensor applications.^[53-55]

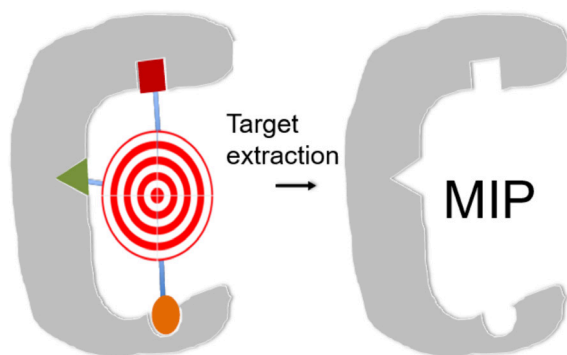


Figure 1.9. Schematic representation of a molecularly imprinted polymer (MIP)

MIPs generally consist of functional monomer and cross-linker molecules. In the production phase, the functional monomer arranges itself around the target molecule, driven by different types of intermolecular interactions both covalent and non-covalent. For covalent interaction, the formation of a covalent bond needs to be easily reversible. Although the recognition of the target by these MIPs is highly specific, the requirements are rather demanding.^[56] The most popular route is therefore the non-covalent method, where interactions are based on the formation of hydrogen bonds, π - π stacking and electrostatic interactions.^[57] The binding sites of the MIPs are formed through the arrangement of functional monomers into a so-called pre-polymerization complex around the target.^[58] By

polymerizing these monomers and with the addition of a cross-linker molecule, this complex is fixated into a rigid polymer matrix. An extraction or washing procedure is subsequently required to extract the target molecule, which produces the specific binding sites.

Good recognition is dependent on a number of parameters. First, the target molecule and functional monomers are required to have functional groups suitable for interaction. Popular functional monomers are therefore acids, such as methacrylic acid (MAA) and acrylic acid (AA) for the formation of H-bonds,^[59] or contain aromatic rings like 2-vinyl pyridine (2-VP) and divinyl benzene (DVB)^[48,60] for π - π stacking. Secondly, the reaction conditions are of significant importance and greatly influence the binding efficiency. Several examples are pH, temperature, solvent and monomer concentration. The pH of the solution determines whether the acidic monomers and target molecules serve as H-acceptor or donor, depending on their respective pK_as. The pH therefore has to be carefully considered to ensure the possibility of H-bond formation. Furthermore, the use of polar and protic solvents can interfere with the formation with H-bonds and must be chosen with care.^[61]

Temperature plays an important role in how the pre-polymerization complex is formed. Lower temperatures stabilize the pre-polymerization complex, while higher temperatures allow for a better interaction between the template and functional monomer. However, high temperatures are considered to be rather disruptive for the pre-polymerization complex and should therefore be avoided. It is therefore beneficial to opt for a photoinitiated procedure that is not performed at high temperatures.^[62]

Solvent does not only play a role in dissolving the involved monomers and targets but also serves as porogen. The porogen makes the polymeric structures weaker, more brittle and the binding sides more accessible. It can induce swelling of the polymer structure and interfere with the intermolecular interaction as stated

earlier.^[63]

Lastly the selected monomers and their respective concentrations need to be optimized.^[64] An increasing amount of functional monomer (with respect to target molecule) will result in an increased number of binding sites, which benefits the sensitivity of the MIP. However, when exceeding the optimal amount of monomer, aspecific binding is increased. This harms the MIP's selectivity, possibly to an extent of being not selective at all. The concentration of cross-linker furthermore affects the rigidity of the polymer matrix. This amount has to be optimized to preserve the MIP's efficiency and thus binding sites per gram polymer. Spivak reported the use of a functional cross-linker, which negates the latter optimization process.^[65]

The most reported polymerization strategy for MIPs is a free radical polymerization, mainly because of its straightforward procedure. The reaction is often initiated via thermolysis (60 °C - 120 °C) of a radical initiator.^[62] Recently more and more data is reported for the use of RDRP strategies for the production of MIPs. Because of the achieved control of propagation and termination of the polymerization, the heterogeneity of the binding sites is improved and concomitantly their quality.^[66] The considered RDRP routes are iniferter,^[67] nitroxide-mediated radical polymerization (NMP),^[68] RAFT^[69] and ATRP^[70]. Although each reaction has been demonstrated to improve the MIP quality, not each strategy is equally beneficial. NMP is carried out at elevated temperatures to be able to break the C-ON bond. Classical ATRP on the other hand is not compatible with acidic monomers and will exhibit low conversions for several types of functional monomers. The additional purification procedure to remove the metal catalysts is an extra disadvantage. RAFT and iniferter have good compatibility with a wide variety of monomers. The dormant RAFT species will furthermore not interfere with polar or ionic groups present on the functional monomer or molecular template.^[71] RAFT can however be problematic for the production of MIP thin films, as it requires a tedious

optimization. This is mainly to avoid undesired polymerization as propagation would be possible from the exogenous initiator as well as the reversibly released R-groups.

MIPs can be produced in a variety of shapes and forms. These include MIP beads, bulk polymers, membranes or thin films.^[72] To implement MIPs into a sensor, presynthesized MIP particles are often stamped or sprayed on a substrate.^[73,74] This can lead to relatively low coverage of the substrate, poor reproducibility due to random detachment of the particles and a bulky sensor. An alternative is to directly and covalently graft a MIP thin film from a substrate in a controlled fashion, as schematically displayed in **Figure 1.10**.^[70,71,75] This strategy is explored within this thesis.

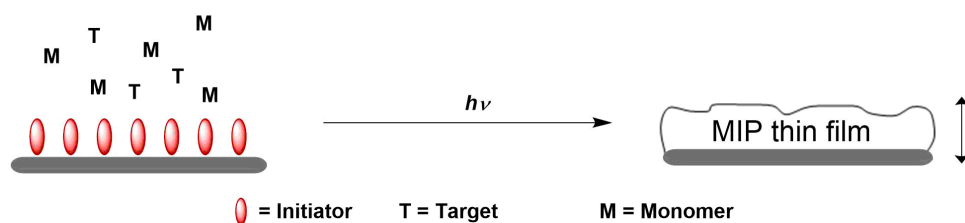


Figure 1.10. Schematic representation of a surface grown MIP procedure using a photomediated RDRP.

MIP thin films are produced on a variety of substrates such as particles, planar substrates and nano-rods.^[52,76] They are mainly reported to be used for the recognition of small molecules.^[77] Imprinting of macromolecules like proteins remains challenging. The larger cavity allows smaller molecules to interact, which reduces selectivity. Furthermore, the conformational changes in macromolecules like proteins can impede recognition^[78]

When grafting a thin polymer film, imprints are more likely to be situated at the surface of the polymer matrix. By this so-called surface imprinting, cavities are

more readily accessible for target recognition and allow for more efficient target removal. This comes with increased binding efficiencies.^[76] The morphology of the films is generally characterized by scanning electron microscopy (SEM) or atom force microscopy (AFM). Methods to generate surface imprinted thin film include drop-casting, spin coating, mini-emulsion, micro-contact printing and grafting. This leads to a variety of possible applications of which a few are listed below.^[76]

MIP thin films can be grafted directly from quartz crystal microbalance (QCM) chips to obtain a QCM sensor. This was previously done by applying the drop casting method and subsequently using UV exposure to cure the monomer mixture.^[79,80] A popular material for such applications is polydopamine. It is known for its simplicity, as the coating is formed over time at ambient conditions by mixing the dopamine in an alkaline buffer solution.^[81,82] Another example is the modification of quantum dots, where amino propyl triethoxysilane (APTES) was used as a functional monomer for the detection of proteins. Quantum dots are generally known for their use in fluorescence spectroscopy.^[83] Similar to QCM sensors, gold sensor chips can be coated for their use in surface plasmon resonance (SPR). Bier and coworkers presented the production of (ultra)thin films of around 4 nm.^[84] Poly-scopoletin was precipitated on the gold chip using electropolymerization after the target peptide was immobilized.^[85] This resulted in all templates generating a cavity accessible for binding after extraction, illustrating the efficiency of surface imprinting with the production of (ultra)thin MIP films. An example of direct grafting was given by Yin *et al.* where an ATRP initiator was immobilized on a membrane to produce *tert*-butylmethacrylate brushes which were subsequently hydrolyzed to obtain MAA.^[86] Imprints were eventually realized by cross-linking the brushes in the presence of the target analyte with the addition of N,N'-methylenebisacrylamide and exposure to UV light. A last example is the production of a MIP thin film through micro-contact imprinting.^[87] A glass cover slide was functionalized with target molecule. First, the target was embedded in functional monomer to allow

the formation of the pre-polymerization complex. Subsequently the cover slide was placed on a support containing initiator and cross-linker. After cross-linking was induced by UV irradiation, the cover slide was removed. The embedded target was subsequently extracted to free the surface imprints. Several other targets and strategies were reported, proving the versatility of this technique.^[47,76]

1.5 Sensor set-up

1.5.1 Chemical sensors

A chemical sensor is a device that translates chemical input into an electrical signal.^[88] This chemical input can vary from a conformational change of an analyte to a chemical reaction, a concentration change or composition change. The input acts on a sensitive layer or receptor layer. Subsequently this information is translated via a transducer, which converts it into a processable signal. Such transducers can be electrical, optical, magnetic or based on mass or temperature. The signal is transformed into an electrical output, which can be processed into interpretable data (**Figure 1.11**). The sensing is required to be continuous and the interaction of the analyte with the transducer needs to be reversible.^[89]

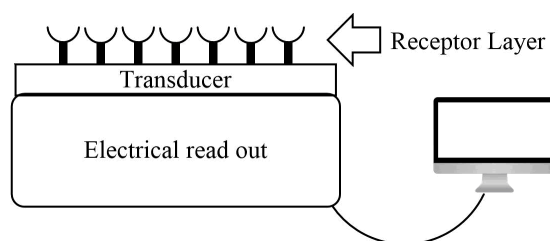


Figure 1.11. General schematic representation of a general chemical sensor set-up.

To measure concentration fluctuations a transducing system is coated with a receptor layer. Due to their comparable specificity to Abs, surface grown MIPs are a suitable alternative. The binding of target molecules to MIPs could then be transduced using electrical impedance spectroscopy.

1.5.2 Electrical impedance spectroscopy

Impedance is comparable to electrical resistance but does not only account for the ratio in magnitude of the electrical potential and the current but also the phase. ^[90-92] This means impedance is measured in a system with an alternating electrical current (AC). Impedance spectroscopy in an AC system does not only provide information on the resistive properties, like in DC, but additionally gives information on the capacitive properties of the system. Furthermore, measurements in a DC sensor set-up only provide information on the complete cell, as the voltage is fixed. For AC, different components can be separately characterized by sweeping the AC's frequency.

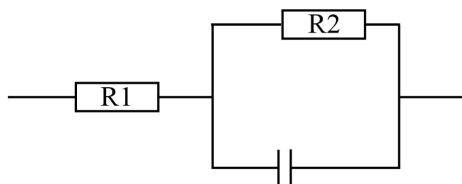


Figure 1.12. Randles cell used as a model in electrical impedance spectroscopy. R1 representing the solution resistance, R2 representing the charge transfer resistance and the electrochemical double layer represented by the capacitor.

The electrical cell which can be used as a model for electrical impedance spectroscopy is better known as the Randles cell, depicted in **Figure 1.12**. R1 represents the solution resistance, which is in series with the charge transfer resistance (R2) parallel to a capacitor. This capacitor represents an electrochemical

double layer, in this case the interface between the liquid and the MIP film.^[73,74] The optimal frequency range, or sensor region, has to be determined. In other words, at which frequency is the signal to noise ratio optimal. Limit of detection is typically three times the noise intensity. Output of a Randles cell can be displayed in a Bode plot as depicted in **Figure 1.13** showing an upper and lower plateau phase representing the combination of R1 and R2, and R1 respectively. The impact of multiple parameters affecting the double layer can be monitored in between the plateau phases, including the binding of target molecules. This can be used to directly characterize and visualize the binding properties of the surface grown MIPs.

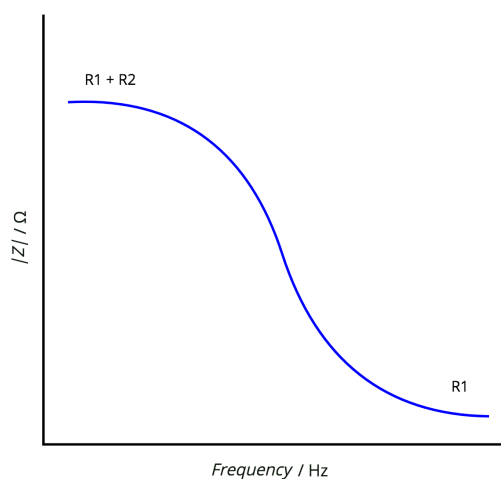


Figure 1.13. Simplified Bode plot for a Randles cell (both axes logarithmic). Upper plateau represents the sum of R1 and R2. Lower plateau phase represents R1.

1.6 Step-growth polymerization towards the production of biomaterials

Side projects discussed in this thesis revolved around the development of synthesis procedures to produce biomaterials for the formation of microstructures including particles or more complex 3D printed structures. These were produced to assess their potential use in tissue engineering. Reactions used for conjugation, post-modification or step-growth polymerizations within these projects are briefly introduced in the next sections.

1.6.1 Michael addition reactions

Thiol-ene Michael additions are reactions between activated, electron poor vinyl groups and nucleophilic thiols yielding a thioether. They are generally used to efficiently link small molecules to each other or to bigger structures and surfaces.^[93] Furthermore, by using bifunctional precursors, polymers can be synthesized via a step-growth polymerization^[94,95] and cross-linked polymer networks can be formed.^[96] Additionally, such materials can be made degradable when using acrylic linkers to introduce ester moieties to the polymer chain making them interesting for bio-applications.

The thiol-ene Michael addition reaction is classified as a click reaction. Requirements to be classified as such are described by Sharpless.^[97,98] Several examples are a high reaction rate, orthogonality and generation of high yields. The reaction is often used in polymerization chemistry for post-modification of polymeric materials because of the straightforward conversion of RAFT end-groups into thiols (through aminolysis).^[99]

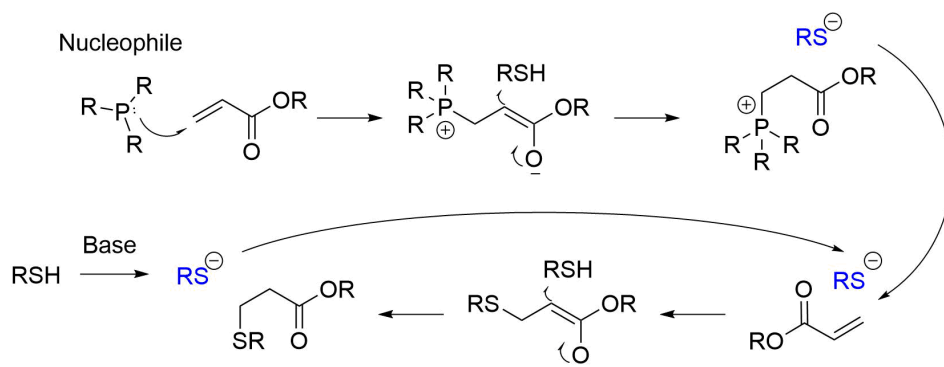


Figure 1.14. Mechanism of nucleophile or base catalyzed Michael addition.

The reaction is catalyzed by a base or nucleophile initiating the mechanistic cycle, as depicted in **Figure 1.14**. In both cases, a nucleophile will add to the activated vinyl group.^[100] For the base catalyzed route, the thiol will be deprotonated by the base, allowing it to act as a nucleophile before entering the same mechanistic cycle. The hereby formed zwitterion will deprotonate a thiol which will then add to an available vinyl group, forming the thioether.^[101–103]

1.6.2 Morita-Baylis-Hillman reactions

The Morita-Baylis-Hillman (MBH) reaction yields interesting adducts, producing densely functionalized molecules.^[104] This makes it possible to post-modify MBH products through a variety of reactions. MBH reaction is an addition reaction involving an electron poor double bond (acrylates) and aldehydes. Similar to Michael additions, a base is required to catalyze the reaction.^[105] For MBH additions, a tertiary or hindered amine or phosphine is preferred. The reaction is known for its low reaction rates, despite several reported improvements.^[106] A simplified mechanistic cycle is depicted in **Figure 1.15**.^[106] An enolate is formed after addition of the nucleophilic catalyst (int1). This allows the addition of the aldehyde to form the second zwitterionic intermediate (int2). From int2 to int3,

a proton transfer is involved, whereafter the base is released, yielding the MBH product. The rate determining step in the early phase of the reaction is the proton transfer. Aggarwal proposed that the reaction was autocatalyzed through the formation of the alcohol groups above 20% conversion.^[106] These moieties were found to catalyze the proton transfer.^[107] Aggarwal confirmed higher reaction rates through the addition of methanol.

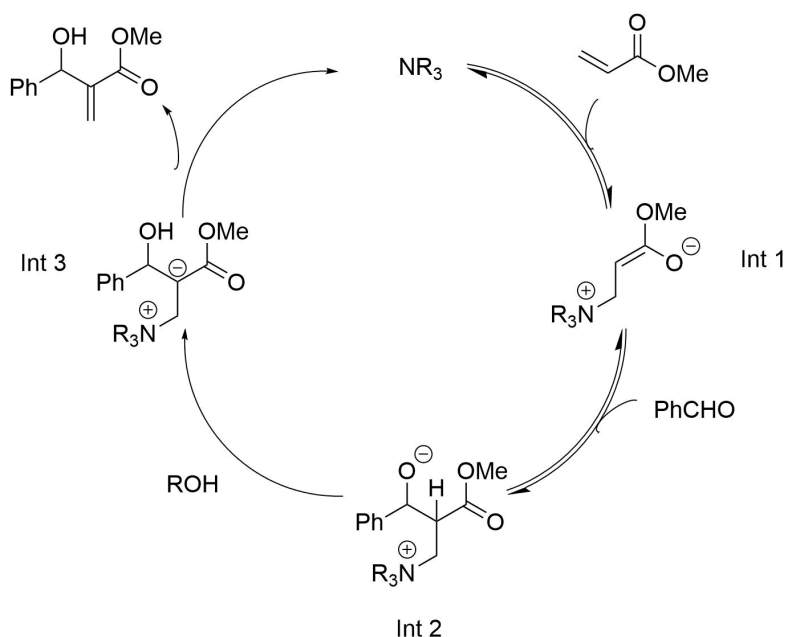


Figure 1.15 Proposed mechanism for Morita-Baylis-Hillman reaction.^[105]

Klok and coworkers^[108–110] elaborated on the applications of MBH reactions with the production of densely functionalized polymers through a step-growth mechanism. Different procedures and catalyst/monomer combinations were tested and optimized. Polymerization was slow, yielding polymers up to 1700 g·mol⁻¹, which is in line with the reputation of this reaction.

1.7 Goal and general overview

This thesis reports the investigation and development of synthesis routes to produce surface-grown MIPs. Photomediated polymerization is a key component to progress this field towards miniature designs and multi target arrays. Therefore, both photoiniferter and photoATRP were developed towards these applications with the latter being optimized and tested for the detection of histamine. Furthermore, side projects revolving around the development of novel polymeric materials towards their use in tissue engineering are presented.

Chapter 2 embarks the beginning of this journey with the exploration of metal-free ATRP (or O-ATRP). Since classical ATRP is not compatible with acidic monomers, which are very popular for their use in MIPs, the possibilities of the metal-free procedure are investigated in this context. This was assessed with the polymerization of methacrylic acid (MAA) in solution and elaborated to polymerization in a continuous flow process. Ultimately, PMAA brushes were grafted from silicon wafers.

The development of titanium-grown MIPs targeting histamine is described in **Chapter 3**. Polymer films were grafted using the metal-free ATRP procedure explored in Chapter 2, using a UV-laser. Detailed chemical characterization of the MIP film was reported to support the discussion on the optimization process. The performance of the MIP films in a sensor set-up was directly visualised using impedance spectroscopy.

In **Chapter 4** a surface initiated photoiniferter procedure was presented as an alternative to metal-free ATRP. Xanthates were used as iniferter agents and immobilized on silicon wafers. PMA brushes were grafted upon UV-exposure and characterized.

Chapter 5 covers the development of functional polymer resins for their application in two-photon polymerization (2PP). This was achieved by adding trithiocarbonates to the resin and subsequently inducing a RAFT mechanism. The 3D printing of microstructures in 2PP and preliminary post-modification experiments via the RAFT end-groups were presented.

A Morita-Baylis-Hillman step-growth polymerization to produce functional polymer particles was described in **Chapter 6**. The MBH polymers were cross-linked by exploiting the MBH adducts via thiol-ene Michael additions. The microparticles were subjected to degradation experiments, post-modification through the formation of imines and to cell studies.

An appendix with additional data (figures and tables) can be found in **Chapter 7**. The reader is referred to the appendix when "A" precedes a figure or table number (e.g. Figure A1). The used materials and characterization methods are listed in **Chapter 8**. A general summary (samenvatting), conclusion and outlook can be found in **Chapter 9**.

At the end a list of **publications and contributions** is added before ultimately concluding with the **acknowledgements (dankwoord)**.

1.8 References

- [1] S. Yaqub, U. Latif, F. L. Dickert, *Sensors Actuators B Chem.* **2011**, *160*, 227–233.
- [2] G. Luka, A. Ahmadi, H. Najjaran, E. Alocilja, M. DeRosa, K. Wolthers, A. Malki, H. Aziz, A. Althani, M. Hoorfar, *Sensors* **2015**, *15*, 30011–30031.
- [3] W. R. Ashcroft, *Industrial Polymer Applications : Essential Chemistry and Technology*, **2016**.
- [4] M. Kato, M. Kamigaito, M. Sawamoto, T. Higashimura, *Macromolecules* **1995**, *28*, 1721–1723.
- [5] J.-S. Wang, K. Matyjaszewski, *J. Am. Chem. Soc.* **1995**, *117*, 5614–5615.
- [6] J. Chiefari, Y. K. Chong, F. Ercole, J. Krstina, J. Jeffery, T. P. T. Le, R. T. A. Mayadunne, G. F. Meijs, C. L. Moad, G. Moad, E. Rizzardo, S. H. Thang, *Macromolecules* **1998**, *31*, 5559–5562.
- [7] T. Otsu, M. Yoshida, T. Tazaki, *Die Makromol. Chemie, Rapid Commun.* **1982**, *3*, 133–140.
- [8] X. Pan, M. A. Tasdelen, J. Laun, T. Junkers, Y. Yagci, K. Matyjaszewski, *Prog. Polym. Sci.* **2016**, *62*, 73–125.
- [9] T. G. Ribelli, F. Lorandi, M. Fantin, K. Matyjaszewski, *Macromol. Rapid Commun.* **2018**, 1800616.
- [10] B. P. Fors, C. J. Hawker, *Angew. Chemie Int. Ed.* **2012**, *51*, 8850–8853.
- [11] X. Pan, N. Malhotra, S. Dadashi-Silab, K. Matyjaszewski, *Macromol. Rapid Commun.* **2016**, 1600651.
- [12] Z. Guan, B. Smart, *Macromolecules* **2000**, *33*, 6904–6906.

- [13] E. Frick, A. Anastasaki, D. M. Haddleton, C. Barner-Kowollik, *J. Am. Chem. Soc.* **2015**, *137*, 6889–6896.
- [14] D. Konkolewicz, K. Schröder, J. Buback, S. Bernhard, K. Matyjaszewski, *ACS Macro Lett.* **2012**, *1*, 1219–1223.
- [15] A. Anastasaki, V. Nikolaou, Q. Zhang, J. Burns, S. R. Samanta, C. Waldron, A. J. Haddleton, R. McHale, D. Fox, V. Percec, P. Wilson, D. M. Haddleton, *J. Am. Chem. Soc.* **2014**, *136*, 1141–9.
- [16] J. Mosnáček, M. Ilčíková, *Macromolecules* **2012**, *45*, 5859–5865.
- [17] N. J. Treat, H. Sprafke, J. W. Kramer, P. G. Clark, B. E. Barton, J. Read de Alaniz, B. P. Fors, C. J. Hawker, *J. Am. Chem. Soc.* **2014**, *136*, 16096–101.
- [18] G. M. Miyake, J. C. Theriot, *Macromolecules* **2014**, *47*, 8255–8261.
- [19] Z. Huang, Y. Gu, X. Liu, L. Zhang, Z. Cheng, X. Zhu, *Macromol. Rapid Commun.* **2017**, *38*, DOI 10.1002/marc.201600461.
- [20] C. Kutahya, F. S. Aykac, G. Yilmaz, Y. Yagci, *Polym. Chem.* **2016**, *7*, 6094–6098.
- [21] X. Pan, C. Fang, M. Fantin, N. Malhotra, W. Y. So, L. A. Peteanu, A. A. Isse, A. Gennaro, P. Liu, K. Matyjaszewski, *J. Am. Chem. Soc.* **2016**, *138*, 2411–2425.
- [22] J. C. Theriot, B. G. McCarthy, C.-H. Lim, G. M. Miyake, *Macromol. Rapid Commun.* **2017**, *38*, 1700040.
- [23] X. Pan, C. Fang, M. Fantin, N. Malhotra, W. Y. So, L. A. Peteanu, A. A. Isse, A. Gennaro, P. Liu, K. Matyjaszewski, *J. Am. Chem. Soc.* **2016**, *138*, 2411–2425.

- [24] T. Otsu, T. Matsunaga, T. Doi, A. Matsumoto, *Eur. Polym. J.* **1995**, *31*, 67–78.
- [25] J. C. Theriot, G. M. Miyake, C. A. Boyer, *ACS Macro Lett.* **2018**, *7*, 662–666.
- [26] J. C. Theriot, G. M. Miyake, C. A. Boyer, *ACS Macro Lett.* **2018**, *7*, 662–666.
- [27] J. Laun, M. Vorobii, A. De Los Santos Pereira, O. Pop-Georgievski, V. Trouillet, A. Welle, C. Barner-Kowollik, C. Rodriguez-Emmenegger, T. Junkers, *Macromol. Rapid Commun.* **2015**, *36*, 1681–1686.
- [28] E. H. Discekici, C. W. Pester, N. J. Treat, J. Lawrence, K. M. Mattson, B. Narupai, E. P. Toumayan, Y. Luo, A. J. McGrath, P. G. Clark, J. Read de Alaniz, C. J. Hawker, *ACS Macro Lett.* **2016**, *5*, 258–262.
- [29] E. H. Discekici, C. W. Pester, N. J. Treat, J. Lawrence, K. M. Mattson, B. Narupai, E. P. Toumayan, Y. Luo, A. J. McGrath, P. G. Clark, J. Read de Alaniz, C. J. Hawker, *ACS Macro Lett.* **2016**, *5*, 258–262.
- [30] S. Telitel, F. Dumur, S. Telitel, O. Soppera, M. Lepeltier, Y. Guillaneuf, J. Poly, F. Morlet-Savary, P. Fioux, J.-P. Fouassier, D. Gigmes, J. Iallevée, *Polym. Chem.* **2015**, *6*, 613–624.
- [31] J. Laun, Y. De Smet, E. Van de Reydt, A. Krivcov, V. Trouillet, A. Welle, H. Möbius, C. Barner-Kowollik, T. Junkers, *Chem. Commun.* **2018**, *54*, 751–754.
- [32] E. Larsson, S. A. Pendergraph, T. Kaldéus, E. Malmström, A. Carlmark, *Polym. Chem.* **2015**, *6*, 1865–1874.

- [33] J. O. Zoppe, N. C. Ataman, P. Mocny, J. Wang, J. Moraes, H. A. Klok, *Chem. Rev.* **2017**, *117*, 1105–1318.
- [34] J. Moehrke, P. Vana, *Macromol. Chem. Phys.* **2017**, *218*, 1600506.
- [35] L. G. Bach, B. T. P. Quynh, V. T. T. Ho, *J. Nanosci. Nanotechnol.* **2017**, *17*, 4127–4131.
- [36] S. Hosseinzadeh, H. Hosseinzadeh, S. Pashaei, Z. Khodaparast, *Ecotoxicol. Environ. Saf.* **2018**, *161*, 34–44.
- [37] T. Chen, I. Amin, R. Jordan, *Chem. Soc. Rev.* **2012**, *41*, 3280.
- [38] G. Zeng, M. Liu, R. Jiang, C. Heng, Q. Huang, L. Mao, J. Hui, F. Deng, X. Zhang, Y. Wei, *Mater. Sci. Eng. C* **2017**, *77*, 420–426.
- [39] J. Yan, X. Pan, Z. Wang, J. Zhang, K. Matyjaszewski, *Macromolecules* **2016**, *23*, 9283–9286.
- [40] T. Zhang, T. Chen, I. Amin, R. Jordan, *Polym. Chem.* **2014**, *5*, 4790–4796.
- [41] M. Vorobii, A. de los Santos Pereira, O. Pop-Georgievski, N. Y. Kostina, C. Rodriguez-Emmenegger, V. Percec, *Polym. Chem.* **2015**, DOI 10.1039/C5PY00506J.
- [42] J. Yan, X. Pan, M. Schmitt, Z. Wang, M. R. Bockstaller, K. Matyjaszewski, *ACS Macro Lett.* **2016**, *5*, 661–665.
- [43] E. D. Bain, K. Dawes, A. E. Özçam, X. Hu, C. B. Gorman, J. Šrogl, J. Genzer, *Macromolecules* **2012**, *45*, 3802–3815.
- [44] Y. Nakayama, T. Matsuda, **1996**, *Macromolecules* **1996**, *96*, 8622–8630.
- [45] B. de Boer, H. K. Simon, M. P. L. Werts, E. W. van der Vegte, G. Hadziioannou, *Macromolecules* **2000**, *2*, 349–356.

- [46] A. Bagheri, Z. Sadrearhami, N. N. M. Adnan, C. Boyer, M. Lim, *Polymer (Guildf)*. **2018**, *151*, 6–14.
- [47] J. J. BelBruno, *Chem. Rev.* **2018**, acs.chemrev.8b00171.
- [48] B. Ara, M. Muhammad, M. Salman, R. Ahmad, N. Islam, T. ul H. Zia, *Appl. Water Sci.* **2018**, *8*, 41.
- [49] Z. Li, Z. Qian, S. Hu, T. Gong, Q. Xian, *Chemosphere* **2018**, *212*, 872–880.
- [50] I. Ahmad, W. A. Siddiqui, S. Qadir, T. Ahmad, *J. Mater. Res. Technol.* **2018**, *7*, 270–282.
- [51] C. Giovannoli, C. Passini, F. di Nardo, L. Anfossi, C. Baggiani, I. A. Nicholls, *Polymers (Basel)*. **2018**, *10*, 192.
- [52] Q. Liu, J. Wan, X. Cao, *Process Biochem.* **2018**, *70*, 168–178.
- [53] M. E. E. Alahi, S. C. Mukhopadhyay, L. Burkitt, *Sensors Actuators B Chem.* **2018**, *259*, 753–761.
- [54] R. Hu, R. Tang, J. Xu, F. Lu, *Anal. Chim. Acta* **2018**, *1034*, 176–183.
- [55] Y. Yang, X. Liu, G. Ye, S. Zhu, Z. Wang, X. Huo, K. Matyjaszewski, Y. Lu, J. Chen, *ACS Appl. Mater. Interfaces* **2017**, *9*, 13637–13646.
- [56] G. Wulff, **1986**, pp. 186–230.
- [57] R. Arshady, K. Mosbach, *Die Makromol. Chemie* **1981**, *182*, 687–692.
- [58] I. Chianella, M. Lotierzo, S. A. Piletsky, I. E. Tothill, B. Chen, K. Karim, A. P. F. Turner, *Anal. Chem.* **2002**, *6*, 1288–1293.

- [59] M. Peeters, P. Csipai, B. Geerets, a Weustenraed, B. van Grinsven, R. Thoelen, J. Gruber, W. De Ceuninck, T. J. Cleij, F. J. Troost, P. Wagner, *Anal. Bioanal. Chem.* **2013**, *405*, 6453–60.
- [60] P. Zhang, X. Ji, H. Zhang, B. Xia, *Comput. Theor. Chem.* **2017**, *1108*, 76–85.
- [61] C. Yu, K. Mosbach, *J. Chromatogr. A* **2000**, *888*, 63–72.
- [62] D. J. O’Shannessy, B. Ekberg, K. Mosbach, *Anal. Biochem.* **1989**, *177*, 144–9.
- [63] S. A. Nabavi, G. T. Vladislavljević, A. Wicaksono, S. Georgiadou, V. Manović, *Colloids Surfaces A Physicochem. Eng. Asp.* **2017**, *521*, 231–238.
- [64] S. Li, Y. Ge, S. A. Piletsky, A. P. F. Turner, *Adv. Funct. Mater.* **2011**, *21*, 3344–3349.
- [65] M. Sibrian-Vazquez, D. A. Spivak, *J. Am. Chem. Soc.* **2004**, *126*, 7827–7833.
- [66] V. D. Salian, A. D. Vaughan, M. E. Byrne, *J. Mol. Recognit.* **2012**, *25*, 361–369.
- [67] G. Wulff, B.-O. Chong, U. Kolb, *Angew. Chemie Int. Ed.* **2006**, *45*, 2955–2958.
- [68] S. Boonpangrak, M. J. Whitcombe, V. Prachayasittikul, K. Mosbach, L. Ye, *Biosens. Bioelectron.* **2006**, *22*, 349–354.
- [69] P. A. G. Cormack, F. S. Mehamod, *Sains Malaysiana* **2013**, *42*, 529–535.
- [70] Z. Adali-Kaya, B. Tse Sum Bui, A. Falcimaigne-Cordin, K. Haupt, *Angew. Chemie* **2015**, *127*, 5281–5284.

- [71] M. J. Garcia-Soto, K. Haupt, C. Gonzato, *Polym. Chem.* **2017**, *8*, 4830–4834.
- [72] A. Biffis, G. Dvorakova, A. Falcimaigne-Cordin, Springer, Berlin, Heidelberg, **2010**, pp. 29–82.
- [73] M. Peeters, F. J. Troost, R. H. G. Mingels, T. Welsch, B. van Grinsven, T. Vranken, S. Ingebrandt, R. Thoelen, T. J. Cleij, P. Wagner, *Anal. Chem.* **2013**, *85*, 1475–83.
- [74] M. Peeters, F. J. Troost, B. van Grinsven, F. Horemans, J. Alenus, M. S. Murib, D. Keszthelyi, A. Ethirajan, R. Thoelen, T. J. Cleij, P. Wagner, *Sensors and Actuators B-Chemical* **2012**, *171*, 602–610.
- [75] M. Peeters, S. Kobben, K. L. Jiménez-Monroy, L. Modesto, M. Kraus, T. Vandeneyt, a. Gaulke, B. van Grinsven, S. Ingebrandt, T. Junkers, P. Wagner, *Sensors Actuators B Chem.* **2014**, *203*, 527–535.
- [76] R. I. Boysen, L. J. Schwarz, D. V. Nicolau, M. T. W. Hearn, *J. Sep. Sci.* **2017**, *40*, 314–335.
- [77] M. C. Blanco-Lopez, S. Gutiérrez-Fernandez, M. J. Lobo-Castanon, A. J. Miranda-Ordieres, P. Tunon-Blanco, *Anal. Bioanal. Chem.* **2004**, *378*, 1922–1928.
- [78] M. J. Whitcombe, I. Chianella, L. Larcombe, S. A. Piletsky, J. Noble, R. Porter, A. Horgan, *Chem. Soc. Rev.* **2011**, *40*, 1547–1571.
- [79] D. Tai, C. Lin, T. Wu, L.-K. Chen, *Anal. Chem.* **2005**, *16*, 5140–5143
- [80] D.-F. Tai, M.-H. Jhang, G.-Y. Chen, S.-C. Wang, K.-H. Lu, Y.-D. Lee, H.-T. Liu, *Anal. Chem.* **2010**, *82*, 2290–2293.

- [81] C.-H. Lu, Y. Zhang, S.-F. Tang, Z.-B. Fang, H.-H. Yang, X. Chen, G.-N. Chen, *Biosens. Bioelectron.* **2012**, *31*, 439–444.
- [82] J. H. Ryu, P. B. Messersmith, H. Lee, *ACS Appl. Mater. Interfaces* **2018**, *10*, 7523–7540.
- [83] Y.-Q. Yang, X.-W. He, Y.-Z. Wang, W.-Y. Li, Y.-K. Zhang, *Biosens. Bioelectron.* **2014**, *54*, 266–272.
- [84] N. Gajovic-Eichelmann, E. Ehrentreich-Förster, F. F. Bier, *Biosens. Bioelectron.* **2003**, *19*, 417–422.
- [85] D. Dechtrirat, K. J. Jetzschmann, W. F. M. Stöcklein, F. W. Scheller, N. Gajovic-Eichelmann, *Adv. Funct. Mater.* **2012**, *22*, 5231–5237.
- [86] D. Yin, M. Ulbricht, *Biomacromolecules* **2013**, *14*, 4489–4496.
- [87] P.-C. Chou, J. Rick, T.-C. Chou, *Anal. Chim. Acta* **2005**, *542*, 20–25.
- [88] W. Wang, in *Progresses Chem. Sens.*, InTech, **2016**.
- [89] J. Janata, *Chem. Rev.* **2008**, 327–328.
- [90] H. Cesiulis, N. Tsyntsaru, A. Ramanavicius, G. Ragoisha, Springer, Cham, **2016**, 3–42.
- [91] N. Storey, *Electronics, A Systems Approach*, Pearson Educated Limited, **2009**.
- [92] F. Lisdat, D. Schäfer, *Anal. Bioanal. Chem.* **2008**, *391*, 1555–1567.
- [93] C.-R. Xu, L. Qiu, C.-Y. Pan, C.-Y. Hong, Z.-Y. Hao, *Bioconjug. Chem.* **2018**, acs.bioconjchem.8b00531.
- [94] J. Vandenberg, G. Ramakers, L. van Lokeren, G. van Assche, T. Junkers,

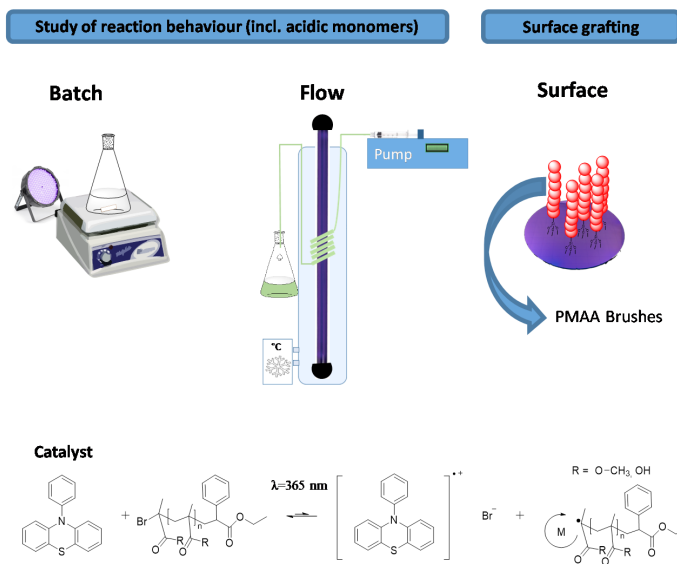
RSC Adv. **2015**, *5*, 81920–81932.

- [95] D. Zhang, M.-J. Dumont, *Macromol. Chem. Phys.* **2018**, *219*, 1800039.
- [96] E. Hachet, N. Sereni, I. Pignot-Paintrand, V. Ravaine, A. Szarpak-Jankowska, R. Auzély-Velty, *J. Colloid Interface Sci.* **2014**, *419*, 52–55.
- [97] H. C. Kolb, M. G. Finn, K. B. Sharpless, *Angew. Chemie-International Ed.* **2001**, *40*, 2004.
- [98] C. Barner-Kowollik, F. E. Du Prez, P. Espeel, C. J. Hawker, T. Junkers, H. Schlaad, W. Van Camp, *Angew. Chemie-International Ed.* **2011**, *50*, 60–62.
- [99] C. Boyer, A. Granville, T. P. Davis, V. Bulmus, *J. Polym. Sci. Part a-Polymer Chem.* **2009**, *47*, 3773–3794.
- [100] J. W. Chan, C. E. Hoyle, A. B. Lowe, M. Bowman, *Macromolecules* **2010**, *43*, 6381–6388.
- [101] J. W. Chan, H. Y. Wei, H. Zhou, C. E. Hoyle, *Eur. Polym. J.* **2009**, *45*, 2717–2725.
- [102] G. Z. Li, R. K. Randev, A. H. Soeriyadi, G. Rees, C. Boyer, Z. Tong, T. P. Davis, C. R. Becer, D. M. Haddleton, *Polym. Chem.* **2010**, *1*, 1196–1204.
- [103] S. Huang, J. Sinha, M. Podgórski, X. Zhang, M. Claudino, C. N. Bowman, *Macromolecules* **2018**, *51*, 5979–5988.
- [104] K. Morita, Z. Suzuki, H. Hirose, *Bull. Chem. Soc. Jpn.* **1968**, *41*, 2815–2815.
- [105] V. K. Aggarwal, I. Emme, S. Y. Fulford, *J. Org. Chem.* **2003**, *68*, 692–700.
- [106] R. Robiette, V. K. Aggarwal, J. N. Harvey, **2007**, DOI 10.1021/JA0717865.

- [107] K. E. Price, S. J. Broadwater, B. J. Walker, D. T. McQuade, *J. Org. Chem.* **2005**, *70*, 3980–3987.
- [108] S. H. Ji, B. Bruchmann, H. A. Klok, *Macromol. Chem. Phys.* **2011**, *212*, 2612–2618.
- [109] S. Ji, B. Bruchmann, F. Wurm, H.-A. Klok, *J. Polym. Sci. Part A Polym. Chem.* **2012**, *50*, 25–34.
- [110] S. Ji, B. Bruchmann, H.-A. Klok, *Macromolecules* **2011**, *44*, 5218–5226.

Chapter 2

Organocatalyzed Photo-Atom Transfer Radical Polymerization of Methacrylic Acid in Flow Synthesis and Surface Grafting



G. Ramakers, A. Krivcov, V. Trouillet, A. Welle, H. Möbius, T. Junkers, *Macromol. Rapid Commun.* **2017**, *38*, 1700423.

2.1 Abstract

The organocatalyzed photo-atom transfer radical polymerization (photoATRP) using 10-phenylphenothiazine (PTH) as catalyst was studied towards its use in methacrylic acid polymerization and surface grafting. The organocatalyzed photoATRP of methyl methacrylate (MMA) was first optimized for continuous flow synthesis in order to assess the livingness of the polymerization. MMA can be polymerized in batch and in flow, however, conversions are limited by the loss of bromine functionality and hence high conversions have to be traded in with increasing dispersities. Also methacrylic acid (MAA) is polymerized successfully in continuous flow with similar limitations. Flow conditions have been transferred to surface grafting from silanized silicon wafers. Presence of ATRP initiators after silanization is confirmed by secondary ion mass spectrometry and x-ray photoelectron spectroscopy. Dense PMAA brush films are successfully produced, which is not directly accessible via classical copper-mediated ATRP techniques.

2.2 Introduction

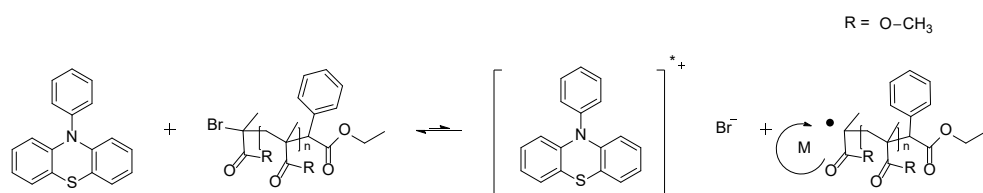
The grafting of polymer brushes from planar substrates or from 3-dimensional particles is a widely used strategy for the modification of surface properties of objects.^[1] The surface of an object is the first barrier in contact with the environment and determines the longevity, toxicity and destination of materials.^[2,3] Therefore, its characteristics are of the highest importance in, for example, biology, medical sciences and generally in materials engineering.^[4] The discovery of reversible deactivation radical polymerization (RDRP) has enabled the exploration of high-value polymer materials with complex architectures. And this with relative synthetic ease.^[5] RDRP allows the precise fine-tuning of materials towards their desired properties. The three most reported controlled radical polymerization strategies are reversible addition fragmentation transfer (RAFT),^[6] nitroxide mediated polymerization (NMP)^[7] and atom transfer radical polymerization (ATRP).^[8,9] All of these techniques are available for surface grafting if the respective initiators or control agents are immobilized on surfaces prior to polymerization. Yet, with the selection of a suitable polymerization strategy for surface chemistry, a few issues have to be considered, such as the generation of radicals in solution (and thus polymerization in solution) or harsh reaction conditions (*e.g.* high temperature). ATRP is in this case a good choice as the initiator can be immobilized on the substrate, thereby keeping in principle all growing chains on its surface. In combination with photoinduced ATRP, which was recently introduced, spatial control can be easily realized, which serves as an additional benefit.^[10,11]

ATRP is, as the name implies, based on the transfer of the halide from the initiator to a metal/ligand complex. The resulting radical propagates to form a polymer in a chain like fashion. Controllability is driven by a persistent radical effect resulting in an excess of dormant polymer species, reversibly deactivated by the halide. This

limits termination reactions and provides control over the polymerization process.^[5,12] A limitation of conventional ATRP is the use of a metal catalyst and the corresponding ligand.^[13] In general, the metal/ligand complex does not permit to polymerize acidic or amine carrying monomers, setting a quite stringent limitation to the technique. Fantin *et al.*^[14] proposed several strategies to overcome the issue with acidic monomers, presenting chain end cyclization as the main cause of termination next to competition with the ligand or its protonation.^[15] Solutions were offered by exchanging bromine for chlorine (less effective leaving group) or by lowering the pH to avoid carboxylate anion formation. Twelve years after the effect of light on ATRP was assessed for the first time,^[16] Hawker presented a photocontrolled ATRP reaction using an iridium based photoredox catalyst,^[17] showing the ability to use methacrylic acid (MAA) in a statistical copolymer with benzyl methacrylate. Haupt later built on that research by surface grafting PMAA in a polymer network using ethylene glycol dimethacrylate as crosslinker towards the production of surface grafted molecularly imprinted polymers (MIPs).^[18] With both groups obtaining satisfying results while using an excess of non-acidic monomers, success could be achieved possibly by avoiding end cyclization to a large extent. Yet, in their study crosslinking polymerization (creating a network rather than individual brushes) was employed so that livingness of polymerizations could not be assessed. Next to iridium based chemistry, also organocatalysts were introduced recently for photoATRP.^[19–30]

In there, photoredox catalysts fulfill the role of the metal catalyst creating propagating radicals after halide abstraction. This is achieved through the oxidative quenching cycle after photoexcitation of the organocatalyst. Issues with the metal/ligand complex are in this case avoided, allowing organocatalyzed photoATRP to work in a broader pH window than classical copper-mediated ATRP. Hence a test in how far these organocatalysts are suitable for acidic monomer polymerization and for surface grafting is highly promising.

Treat et al. reported the successful use of 10-phenylphenothiazine (PTH) as photo-organocatalyst for the polymerization of methyl methacrylate (MMA) (Scheme 2.1) and benzyl methacrylate.^[19] Good polydispersity (≤ 1.2) was obtained (given below 30% conversion) for PMMA. M_n vs conversion was presented with molecular weight data obtained via proton nuclear magnetic resonance ($^1\text{H NMR}$). End-group fidelity was confirmed by performing chain extensions, although ESI-MS data seemed to show peaks, which correspond to species with loss of bromine functionalities.



Scheme 2.1. Schematic representation of metal-free ATRP using 10-phenylphenothiazine.

Miyake first reported the use of perylene as a visible light catalyst^[20], and achieved good end-group fidelity. Over time the same group reported the development of better catalysts and their design in the visible light range, giving better control over molecular weight.^[27,31] The procedure was also optimized for polymerization in a continuous flow reactor.^[25] The results were in line with the general observation that flow chemistry for controlled radical polymerizations increases polymerization rate and improve polymerization performance.^[32-39] However the optimized conditions to preserve the quality of the polymer products (*i.e.* low polydispersity) came with the cost of reaching only intermediate conversions, often around 70%. Furthermore metal-free ATRP was mechanistically studied in detail by Matyjaszewski^[40]. In parallel to these publications, reports were made about the use of different organocatalysts for metal-free ATRP, like anthracene and pyrene^[22], eosin Y and erythrosin B^[28] or about metal-free ATRP in an applied context like thermo responsive gels^[30] or surface engineering of magnetic

nanoparticles for bio-applications.^[41]

Surface grafting of PMMA brushes using PTH as organocatalyst was reported by Hawker on planar wafers^[23] and on SiO₂ nanoparticles by Matyjaszewski.^[42] No report has yet been made for brush formation of acidic monomers, which may have interesting biomedical application due to their polyelectrolyte character. Also the employment of amine carrying functional monomers^[43] is via such route enabled due to absence of ligand competition.

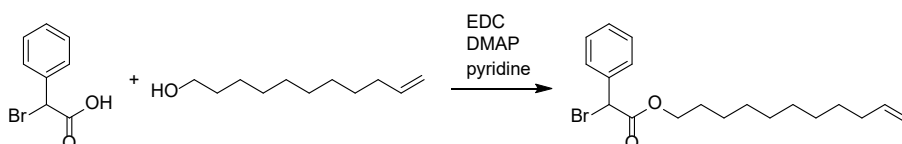
In here, the potential of metal-free ATRP is further explored. Batch and flow polymerization techniques were exploited to gain a more thorough understanding of the reaction using PTH as photo-organocatalyst. Subsequently the applicability in surface-induced ATRP of MAA was investigated on silicon wafers.

2.3 Experimental Section

2.3.1 Synthesis of 10-phenyl(phenothiazine)

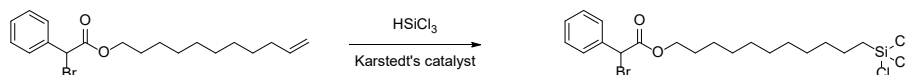
The protocol to synthesize the organocatalyst 10-phenyl(phenothiazine) was adopted from Treat *et al.*^[19] ¹H-NMR spectrum was displayed in Figure A1.

2.3.2 Synthesis of 11-(trichlorosilyl)undecyl 2-bromo-2-phenylethanoate



Scheme 2.2. Synthesis of undec-10-en-1-yl 2-bromo-2-phenylethanoate, precursor of the eventual trichlorosilane

2-Bromo-2-phenyl acetic acid (2.0 g, 9.3 mmol, 1.0 eq.) and 10-undecen-1-ol (1.9 mL; 9.3 mmol; 1.0 mmol) were dissolved in ethyl acetate (50 mL). The mixture was cooled to 0 °C. Subsequently DMAP (113 mg; 0.93 mmol; 0.1 eq.), EDC (1.96 g; 10.2 mmol; 1.1 eq.), and pyridine (0.83 mL; 10.2 mmol; 1.1 eq.) were added. The mixture was stirred overnight and left to cool down to room temperature. The organic phase was washed with 1 M HCl (50 mL) and with brine (2 × 50 mL). Subsequently, the organic phase is dried over MgSO₄. The product is isolated via flash chromatography.



Scheme 2.3. Synthesis of 11-(trichlorosilyl)undecyl 2-bromo-2-phenylethanoate

A round bottom flask was loaded with the isolated precursor molecule under argon. 2 drops of Karstedt's catalyst and 20 mL of trichlorosilane were added subsequently and the mixture was stirred overnight. The unreacted trichlorosilane was removed under vacuum and the remaining product was stored in the freezer inside the glovebox. NMR indicates 100% conversion (missing vinyl protons) ^1H NMR (400 MHz, CDCl_3) δ : 7.67-7.45 (m, 2H), 7.45-7.28 (m, 3H), 5.35(s, 1H), 4.32-4.01 (m, 2H), 1.71-1.51 (m, 4H), 1.47-1.36 (m, 4H), 1.36-1.19 (m, 12H) ppm. Spectrum given in Figure A2.

2.3.3 Metal-free ATRP batch polymerization procedure

For every reported batch polymerization the same procedure was carried out. A GPC vial (1.5 mL) was filled with PTH (1 mg, $3.75 \cdot 10^{-3}$ mmol, 0.05 eq), monomer (3.75 mmol, 50 eq.) and dissolved in DMAc (0.8 g). Subsequently the vial was flushed with Argon and finally EBPA was added, the amount depending on the targeted degree of polymerization (Table A1). The UV-LEDs (370 nm, $0.65 \text{ mW} \cdot \text{cm}^{-2}$ at a distance of 4 cm, Figure A29) were switched on and the mixture was vigorously stirred. Aliquots for GPC and NMR analysis were taken at predetermined times. Preparation for analysis with ESI-MS comprised three times precipitation of the polymer in cold hexane.

2.3.4 Metal-free ATRP flow polymerization procedure

For every reported flow reaction the same procedure was carried out. A Schlenkflask was loaded with PTH (5 mg, $1.88 \cdot 10^{-2}$ mmol, 0.05 eq.), monomer (37.5 mmol, 100 eq), EBPA (65.6 μL , 0.375 mmol, 1 eq.) and 10 mL of DMAc. The mixture was deoxygenated by five freeze-pump-thaw cycles and backfilled with N_2 . The mixture was stored in the freezer inside the glovebox. To perform the flow reaction two gas tight syringes (SGE) of 1 mL were wrapped in aluminium foil and filled with the prepared mixture. Subsequently the syringes were attached to a syringe pump

(Chemtrix) operating at varying flowrates to obtain reaction times of 10, 20, 40, 60, 90 and 120 minutes. All reactions were carried out in the same 200 μL reactor, consisting of PFA tubing (0.5 μm inner \varnothing) wrapped around a UV fluorescent lamp (365 nm emission maximum, $\pm 6 \text{ mW}\cdot\text{cm}^{-2}$). The reactor was placed in a temperature controlled water bath, and monitored using a thermocouple. The temperature of the lamp was in this way always kept below 30 $^{\circ}\text{C}$.

2.3.5 Metal-free ATRP surface grafting procedure

Surface grafting of PMAA was performed on silicon wafers of 1 cm^2 . To clean the wafers they were treated with piranha solution, HCl (pH 3) and Ammonium solution/ H_2O_2 mixture (1:1). The cleaned wafers were transferred to the glovebox for silanization. The synthesized silane was added in excess to the in toluene submerged wafers together with a minimum of 3 equivalents of dry TEA. Ultimately the wafers were rinsed with toluene, THF, EtOH and demineralized water. The silanized wafers were analysed with XPS, ToF-SIMS.

For the surface grafting PTH (1 mg) and MAA (250 μL) were dissolved in DMAc (1 mL). This mixture was flushed with argon for 15 minutes and added to the silanized wafer in an airtight costum-made chamber with a quartz glass window, kept under argon pressure (Figure A3). For reactions with a shadow mask, the mask was placed directly on the wafer inside the reaction chamber. The chamber was directly placed under a UV fluorescent lamp (365 nm, $\pm 2 \text{ mW}\cdot\text{cm}^{-2}$) and left to react for three hours. After the reaction, the wafer was cleaned with THF, EtOH and MilliQ and analysed by XPS, ToF-SIMS and AFM.

2.4 Results and Discussion

2.4.1 Organocatalyzed photoATRP in batch

The reaction was first carried out in batch as described in literature^[19] and optimized for use in a continuous flow reactor on the example of MMA polymerization.

Figure 2.1 compares the molecular weights for organocatalyzed photoATRP of MMA obtained by gel permeability chromatography (GPC) and calculated via ¹H NMR. While both methods are known to be generally reliable, a considerable mismatch is observed at conversions below 20%. While the number average molecular weights obtained via ¹H NMR ($M_{n,NMR}$) follow the calculated theoretical molecular weight, $M_{n,GPC}$ displays a semi-controlled behavior with a stagnating M_n up to about 20% conversion, where it merges with the theoretical plot. Experiments targeting different degrees of polymerization (DP) suggest that $M_{n,GPC}$ merges with the theoretical molecular weight at lower conversions when lower initiator concentrations are employed. Closer inspection of literature data reveals that to varying degree the same effect had been observed before.^[44] Even though extensive tests were carried out, no reason for the mismatch could be identified, leaving a question mark on low conversion data obtained via the method.

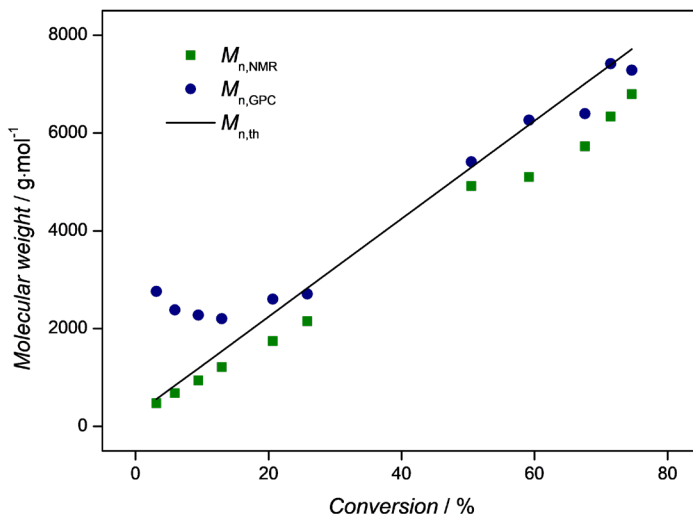


Figure 2.1. M_n vs conversion plot for PMMA using 10-phenylphenothiazine (MMA/I/PTH=100/1/0.05) demonstrating a mismatch between GPC and ^1H NMR data.

Concomitantly – well-fitting to this discrepancy – a comparatively high dispersity (\mathcal{D}) was obtained for the polymers (Table A1). Electrospray ionization - mass spectrometry (ESI-MS) revealed that a certain fraction of polymer chains had their bromine eliminated (Figure A4), which was also seen in literature – but which can also be explained by bromine elimination during the ESI process.^[19] Still, the observed loss in chain-end functionality assumingly contributes to a rather high \mathcal{D} of 1.55 (at $DP = 100$). Regardless, the results from the synthesis of PMMA are well in line with literature^[19,40] and were hence used for benchmarking the polymerization of MAA (Figure A5) which needs to be methylated in order to be measured on regular tetrahydrofuran-size exclusion chromatography setups.

2.4.2 Polymerization in flow

The reaction conditions for polymerization in batch were then transferred and adjusted to a continuous flow process. Due to an improved light efficiency of photo flow reactors compared to their batch counterparts, a faster reaction rate and thus shorter reaction times are expected.^[32,33] For the polymerization of MMA the reaction time required to reach about 50% conversion was reduced from 12 hours to 2 hours (Table A2), a reduction that is well in line with experience gathered on a variety of photoRDRP systems.^[33] However, \mathcal{D} was increased to 2.2 which is on first glance unusual. Also for this reaction ESI-MS confirmed loss of bromine groups (Figure A6). Increasing $M_{n,\text{GPC}}$ with conversion shows the apparent living nature from the start, which is in contrast with the results from the batch reaction. However, between 20 and 30% conversion, the $M_{n,\text{GPC}}$ seems to stagnate, which is hypothesized to be caused by the high light efficiencies reached in the flow reactor. This makes the polymers more vulnerable to the loss of end-groups at longer reaction times (Figure A7) due to bimolecular termination. The employed flow reactor could hence be already too efficient to carry out successful high conversion polymerizations. Reducing light intensity might improve end group fidelity. However, the concomitant increasing reaction time would make this strategy barely feasible for this set-up.

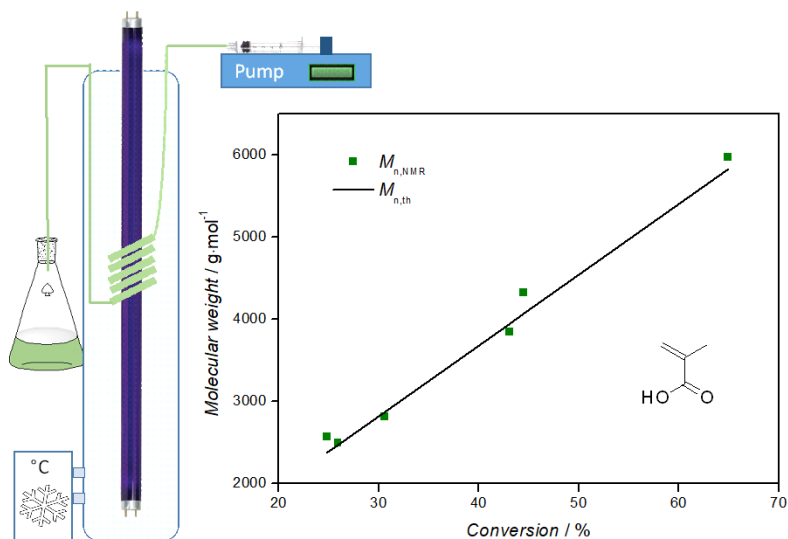


Figure 2.2. Schematic display of the used photo flow reactor. On the r.h.s. the M_n vs conversion plot is given for the polymerization of MAA using metal-free ATRP in such reactor.

Yet, flow polymerization offers interesting insights into the kinetics of the reactions, and is very well suited for screening of reaction conditions. Thus, also for PMAA the procedure was optimized for flow (**Figure 2.2**), The polymerization rate was increased tremendously going from 10 h reaction time for 35% conversion to 2 hours for 65% (Table A3). Since SEC analysis of PMAA is tedious, only $M_{n,NMR}$ was obtained. Again, molecular weights were in excellent agreement with the theoretical values. While flow operation gives advantages over the polymerization with regards to reaction rate, no fully satisfying yields (at concomitantly low dispersities) could be reached. For this type of polymerization, flow chemistry is an excellent tool for the kinetic assessment of the reaction, but serves only poorly as a method of production. The general observations made herein are generally in good agreement with the study by Miyake and coworkers.^[25] No further

optimization of the flow process was hence made, as the data gathered were sufficient for transfer of reaction conditions to surface grafting. Flow chemistry and surface grafting are comparable in the sense that also in surface reactions, typically small optical pathlengths are realized. Hence, surface grafting is in its reaction efficiency and end group conservation probably more comparable to a flow process than its batch counterpart in case of photoinduced reactions.

2.4.3 Grafting of PMAA brushes

In order to prepare for surface reactions a silicon wafer was treated with piranha solution and subsequently silanized. The utilized silane was priorly coupled to an ATRP initiator, namely α -bromophenylacetate. The wafer was exposed to UV-light (365 nm, 2.5 mW·cm⁻²) for 3 hours in an airtight and custom-made reaction chamber provided with a quartz glass window. Water contact angle (WCA) confirmed a significant change of the wettability from an 80 ° contact angle for the silanized wafer to 50 ° contact angle after polymerization suggesting the successful formation of PMAA brushes (Figure A8). This result was supported by grazing angle infrared spectroscopy, where a carbonyl stretch vibration band demonstrates the presence of a polyacrylate on the surface.

While wetting and FTIR-ATR measurement give qualitatively good results, we proceeded to analyze the surfaces in depth for further characterization. In **Figure 2.3a** and **2.3b** a mass spectrum generated via Time-of-Flight Secondary Ion Mass Spectrometry (ToF-SIMS) is depicted. The presence or abundance of fragments from structures relevant to the different modification steps provide qualitative information on the success of the respective modification. In **Figure 2.3b** the intensity of the peak assigned to bromine, which represents the ATRP initiator and thus the silane, indicates a successful silanization. As no bromine is observed for the blank wafer (cleaned with piranha solution), silanization clearly causes the signal to appear. After surface grafting of PMAA the bromine signal is less

intense but still significantly prominent. This indicates the bromine end groups are maintained to a good extent during grafting. To confirm the polymer grafting the methacrylic acid fragment is analyzed in **Figure 2.3a**. As a reference a PMAA polymer indicated in green was drop casted on a silicon wafer. The wafer subjected to the polymer grafting procedure (blue) shows exactly the same peaks and hence confirm the presence of a PMAA polymer film. As expected both the blank and the silanized wafers do not show any according signal.

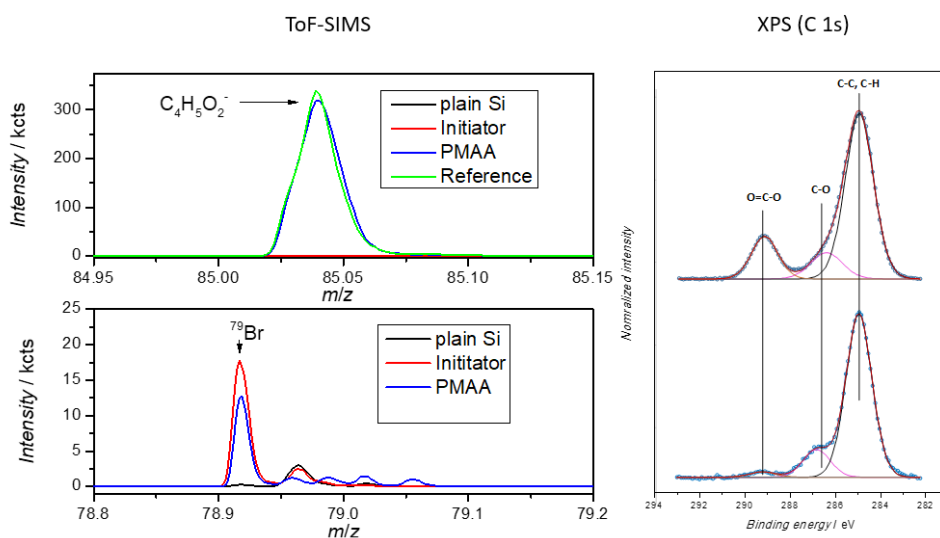


Figure 2.3. a) ToF-SIMS spectrum showing the presence of the methacrylic acid. b) ToF-SIMS spectrum showing the presence of the bromine after silanization and metal-free polymerization c) C 1s XPS spectra confirming the presence of methacrylic acid with the complying change in the intensity of the peak at 289,2 eV. All spectra were normalized to the maximum of intensity.

Additionally, x-ray photoelectron spectroscopy was performed to confirm the grafting of PMAA. **Figure 2.3c** shows the C 1s spectra of a silanized silicon wafer

and of a wafer subsequently grafted with PMAA. The spectrum representing the silanized silicon wafer shows the carbon-carbon bond mainly stemming from the alkyl spacer incorporated in the silane. C-O and O-C=O represent the ester moiety found in the ATRP initiator. The important increase of the intensity of the peak at 289,2 eV attributed to carboxylic acid moiety originating from PMAA shows that the polymerization was successful.^[11] Thus, also XPS confirms the presence of a PMAA film on the wafer. At the same time, the XPS spectrum shows signals corresponding to silicon, indicating that the film thickness is less than about 8-10 nm since this is the information depth of XPS by excitation with Al K α X-ray. A possible explanation for this limited film thickness is discussed below.

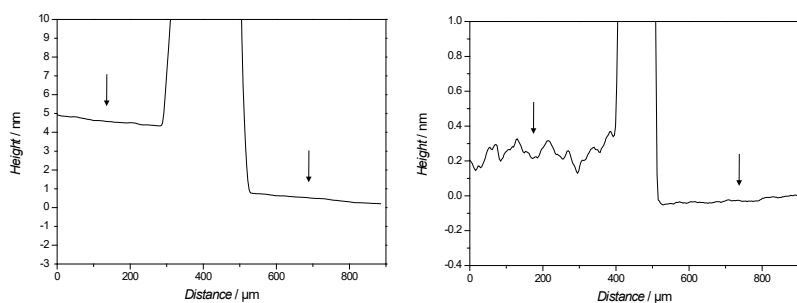


Figure 2.4. Topography of silicon wafer of the scratch test obtain via AFM. Left graph depicts scratch test for area exposed to light and right graph depicts topography for area in the dark.

Atomic force microscopy (AFM) was thus used to determine the exact layer thickness. To obtain additional information on spatial control a shadow mask was applied, exposing a rectangular pattern to the light source. A scratch test revealed a film thickness of 3-4 nm for the illuminated areas, as depicted in **Figure 2.4**, which is in good agreement with the XPS results. However, also in the dark region, a film thickness of maximum 0.3 nm was observed, indicating that patterning

does work via usage of shadow masks, but still leads to a slight homogenous grafting on the whole surface. This effect was seen before in copper-mediated photoATRP,^[11] and it can be hypothesized that this is due to light scattering or diffusion of radicals to non-illuminated areas. The obtained film thicknesses are compared to many other grafting methods relatively small, yet, the layers obtained do have a significant effect on the surface properties (see contact angle measurements). The fact that no bigger brushes were grafted may be explained by the loss of bromine functionality as observed in the flow polymerizations. By losing end group fidelity, chain growth is irreversibly stopped, and also extend illumination no longer has a beneficial effect in creating thicker layers.

2.5 Conclusions

The organocatalyzed photoATRP polymerization was studied towards its use in methacrylic acid polymerization and surface grafting with this polyelectrolyte. Using PTH as catalyst for photoATRP, successful polymerizations of methyl methacrylate and methacrylic acid are carried out. Reactions were optimized for continuous flow synthesis. It was shown that the PTH-mediated photoATRP is not overly suited for production of solution based polymers (in accordance to literature), but it allows for good assessment of the polymerization quality since the small optical pathlengths in the microreactor mimic the conditions of surface grafting. A somewhat confusing result is the observation of a mismatch between NMR and GPC-derived average molecular weights at lower conversions. Closer inspection of literature data reveals that this might not be an uncommon observation and the effect is well reproducible. An explanation for this effect can at this time not be given. Yet, when significant conversions are reached, good agreement of all data is observed, allowing for straightforward assessment of livingness of the polymerization. After MAA polymerization was likewise found to be successful under flow conditions, conditions were transferred to surface grafting of silicon

wafers. Successful grafting with linear MAA brushes was qualitatively confirmed by contact angle measurements and FTIR spectroscopy. Closer inspection of the grafting success by ToF-SIMS and XPS analysis unambiguously confirms this result. Film thicknesses are, however, relatively low. AFM scratch tests reveal a film thickness of 3-4 nm in illuminated areas on the wafer. While this layer is hence quite thin, wetting behavior shows that it is sufficient to change the surface characteristics of the wafer significantly.

Grafting polyelectrolytes is typically challenging and we have shown that PTH-catalyzed photoATRP is a good methodology to reach this aim. Via classical ATRP methods, this could not as easily be achieved. Future work will focus on improving the patterning of the surfaces. Being able to graft a large variety of monomers with apolar, polar or ionic moieties is of uttermost importance to tailor surfaces for biomedical application and PTH seems to be a good catalyst to mediate the grafting of all these monomers. Further, by removing copper from the reaction, potential toxicity of surfaces is completely avoided, which is an additional benefit for future applications.

2.6 References

- [1] R. Barbey, L. Lavanant, D. Paripovic, N. Schüwer, C. Sugnaux, S. Tugulu, H.-A. Klok, *Chem. Rev.* **2009**, *109*, 5437–5527.
- [2] A. Albanese, P. S. Tang, W. C. W. Chan, *Annu. Rev. Biomed. Eng.* **2012**, *14*, 1–16.
- [3] A. Verma, F. Stellacci, *Small* **2010**, *6*, 12–21.
- [4] K. Matyjaszewski, N. V. Tsarevsky, *J. Am. Chem. Soc.* **2014**, *136*, 6513–6533.
- [5] W. A. Braunecker, K. Matyjaszewski, *Prog. Polym. Sci.* **2007**, *32*, 93–146.
- [6] J. Chiefari, Y. K. Chong, F. Ercole, J. Krstina, J. Jeffery, T. P. T. Le, R. T. A. Mayadunne, G. F. Meijs, C. L. Moad, G. Moad, E. Rizzardo, S. H. Thang, *Macromolecules* **1998**, *31*, 5559–5562.
- [7] J. Nicolas, Y. Guillaneuf, C. Lefay, D. Bertin, D. Gigmes, B. Charleux, *Prog. Polym. Sci.* **2013**, *38*, 63–235.
- [8] M. Kato, M. Kamigaito, M. Sawamoto, T. Higashimura, *Macromolecules* **1995**, *28*, 1721–1723.
- [9] J.-S. Wang, K. Matyjaszewski, *J. Am. Chem. Soc.* **1995**, *117*, 5614–5615.
- [10] X. Pan, M. A. Tasdelen, J. Laun, T. Junkers, Y. Yagci, K. Matyjaszewski, *Prog. Polym. Sci.* **2016**, *62*, 73–125.
- [11] J. Laun, M. Vorobii, A. de los Santos Pereira, O. Pop-Georgievski, V. Trouillet, A. Welle, C. Barner-Kowollik, C. Rodriguez-Emmenegger, T. Junkers, *Macromol. Rapid Commun.* **2015**, *36*, 1681–1686.

- [12] V. Coessens, T. Pintauer, K. Matyjaszewski, *Prog. Polym. Sci.* **2001**, *26*, 337–377.
- [13] M. Fantin, A. A. Isse, A. Gennaro, K. Matyjaszewski, *Macromolecules* **2015**, *48*, 6862–6875.
- [14] M. Fantin, A. A. Isse, A. Venzo, A. Gennaro, K. Matyjaszewski, *J. Am. Chem. Soc.* **2016**, *138*, 7216–7219.
- [15] H. Mori, A. H. . Müller, *Prog. Polym. Sci.* **2003**, *28*, 1403–1439.
- [16] Z. Guan, B. Smart, *Macromolecules* **2000**, *33*, 6904–6906.
- [17] B. P. Fors, C. J. Hawker, *Angew. Chemie Int. Ed.* **2012**, *51*, 8850–8853.
- [18] Z. Adali-Kaya, B. Tse Sum Bui, A. Falcimaigne-Cordin, K. Haupt, *Angew. Chemie* **2015**, *127*, 5281–5284.
- [19] N. J. Treat, H. Sprafke, J. W. Kramer, P. G. Clark, B. E. Barton, J. Read de Alaniz, B. P. Fors, C. J. Hawker, *J. Am. Chem. Soc.* **2014**, *136*, 16096–101.
- [20] G. M. Miyake, J. C. Theriot, *Macromolecules* **2014**, *47*, 8255–8261.
- [21] X. Pan, C. Fang, M. Fantin, N. Malhotra, W. Y. So, L. A. Peteanu, A. A. Isse, A. Gennaro, P. Liu, K. Matyjaszewski, *J. Am. Chem. Soc.* **2016**, *138*, 2411–2425.
- [22] A. Allushi, S. Jockusch, G. Yilmaz, Y. Yagci, *Macromolecules* **2016**, *49*, 7785–7792.
- [23] E. H. Discekici, C. W. Pester, N. J. Treat, J. Lawrence, K. M. Mattson, B. Narupai, E. P. Toumayan, Y. Luo, A. J. McGrath, P. G. Clark, J. Read de Alaniz, C. J. Hawker, *ACS Macro Lett.* **2016**, *5*, 258–262.

- [24] Z. Huang, Y. Gu, X. Liu, L. Zhang, Z. Cheng, X. Zhu, *Macromol. Rapid Commun.* **2017**, *38*, 1600461.
- [25] B. L. Ramsey, R. M. Pearson, L. R. Beck, G. M. Miyake, *Macromolecules* **2017**, *50*, 2668–2674.
- [26] R. M. Pearson, C.-H. Lim, B. G. McCarthy, C. B. Musgrave, G. M. Miyake, *J. Am. Chem. Soc.* **2016**, *138*, 11399–11407.
- [27] J. C. Theriot, C.-H. Lim, H. Yang, M. D. Ryan, C. B. Musgrave, G. M. Miyake, *Science* **2016**, *352*, 1082–1086.
- [28] C. Kutahya, F. S. Aykac, G. Yilmaz, Y. Yagci, *Polym. Chem.* **2016**, *7*, 6094–6098.
- [29] X. Liu, L. Zhang, Z. Cheng, X. Zhu, *Polym. Chem.* **2016**, *7*, 689–700.
- [30] M. Chen, S. Deng, Y. Gu, J. Lin, M. J. MacLeod, J. A. Johnson, *J. Am. Chem. Soc.* **2017**, *139*, 2257–2266.
- [31] J. C. Theriot, B. G. McCarthy, C.-H. Lim, G. M. Miyake, *Macromol. Rapid Commun.* **2017**, 1700040.
- [32] C. Tonhauser, A. Natalello, H. Löwe, H. Frey, *Macromolecules* **2012**, *45*, 9551–9570.
- [33] T. Junkers, B. Wenn, *React. Chem. Eng.* **2016**, *1*, 60–64.
- [34] P. Derboven, P. H. M. Van Steenberge, J. Vandenberghe, M.-F. Reyniers, T. Junkers, D. R. D’hooge, G. B. Marin, *Macromol. Rapid Commun.* **2015**, *36*, 2149–2155.
- [35] B. Wenn, M. Conradi, A. D. Carreiras, D. M. Haddleton, T. Junkers, *Polym. Chem.* **2014**, *5*, 3053.

- [36] J. Gardiner, C. H. Hornung, J. Tsanaktsidis, D. Guthrie, *Eur. Polym. J.* **2016**, *80*, 200–207.
- [37] A. Melker, B. P. Fors, C. J. Hawker, J. E. Poelma, *J. Polym. Sci. Part A Polym. Chem.* **2015**, *53*, 2693–2698.
- [38] M. Chen, M. J. MacLeod, J. A. Johnson, *ACS Macro Lett.* **2015**, *4*, 566–569.
- [39] A. Kermagoret, B. Wenn, A. Debuigne, C. Jérôme, T. Junkers, C. Detrembleur, *Polym. Chem.* **2015**, *6*, 3847–3857.
- [40] X. Pan, C. Fang, M. Fantin, N. Malhotra, W. Y. So, L. A. Peteanu, A. A. Isse, A. Gennaro, P. Liu, K. Matyjaszewski, *J. Am. Chem. Soc.* **2016**, *138*, 2411–2425.
- [41] Y. Yang, X. Liu, G. Ye, S. Zhu, Z. Wang, X. Huo, K. Matyjaszewski, Y. Lu, J. Chen, *ACS Appl. Mater. Interfaces* **2017**, *9*, 13637–13646.
- [42] J. Yan, X. Pan, M. Schmitt, Z. Wang, M. R. Bockstaller, K. Matyjaszewski, *ACS Macro Lett.* **2016**, *5*, 661–665.
- [43] E. Kellens, H. Bové, M. Conradi, L. D’Olieslaeger, P. Wagner, K. Landfester, T. Junkers, A. Ethirajan, *Macromolecules* **2016**, *49*, 2559–2567.
- [44] X. Pan, M. Lamson, J. Yan, K. Matyjaszewski, *ACS Macro Lett.* **2015**, *4*, 192–196.

Chapter 3

Laser-grafted Molecularly Imprinted
Polymers for the Detection of Histamine
From Organocatalyzed Atom Transfer
Radical Polymerization.

G. Ramakers, G. Wackers, V. Trouillet, A. Welle, P. Wagner, T. Junkers, *Submitted*.

3.1 Abstract

Molecularly imprinted polymer (MIP) based biomimetic sensors are finding their way into the biomedical world. However the in vivo applications are to date left unexplored. To open up to this area, sensors need to have high reproducibility, require miniaturization and must be free of toxic materials (such as heavy metals). In here, to address these requirements, a metal-free photo atom transfer radical polymerization (ATRP) grafting procedure is described using a pulsed UV-laser as light source to create thin molecularly imprinted polymer (MIP) films on a sensor surface. Film formation and properties are analyzed and discussed. MIP films were templated towards the target molecule histamine, for which in vivo studies can reveal unknown pathological pathways of inflammatory bowel diseases. Using impedance spectroscopy, the biosensor surface is characterized in comparison to non-imprinted film grafts and a high sensitivity towards the target molecule is identified, revealing a limit of detection of 3.4 nM histamine solutions.

3.2 Introduction

Molecularly imprinted polymers (MIPs) are cross-linked polymers that have the ability to bind to specific target molecules with high affinity.^[1] The binding sites in MIPs are produced by polymerizing functional monomers into a cross-linked matrix in presence of a target molecule. By extracting the target, a cavity or imprint is formed, which specifically rebinds the target molecule. Target recognition is mainly based on molecular interaction via hydrogen bond formation, π - π stacking and electrostatic interactions. MIPs are in use for a variety of applications. Prominent examples are solid phase extraction (*e.g.* water purification),^[2-4] affinity chromatography,^[5,6] controlled release arrays (*e.g.* controlled drug release)^[7-9] and analytical detection in biomimetic sensors.^[10-13] The latter generally comprise a receptor layer deposited on top of a transducer to obtain an electrical or optical^[14,15] readout. In the realm of chemical sensors, MIPs are widely reported receptor type as they allow for high sensitivity, comparatively good selectivity and most of all extended shelf life stability.^[16,17] Typically, sensor substrates are planar,^[18,19] spherical or rod-like,^[20] and are coated with molecularly imprinted material. Ways to achieve this comprise the coating of sensor elements with MIP powder or – less often found in literature - the grafting of a polymeric matrix from the surface. When exposing the MIP sensor to analyte concentrations, the target can bind, changing the properties of the receptor layer. Detection methods include the heat transfer method (HTM),^[21,22] where the change in heat transfer can be related to the change of the insulating properties of the MIP layer, or electrochemical impedance spectroscopy, where the change in electrical resistance of the receptor layer under influence of the analyte is followed.^[23,24]

Conventionally MIPs are prepared in solution, where polymerization into a cross-linked matrix results in formation of a rigid monolith. Grinding of the MIP material is then required to obtain a powder suitable for sensor coating. A popular alternative

is the use of suspension polymerization,^[25,26] allowing for direct synthesis of MIP particles that can be deposited on a substrate. Both methods work well, yet result in reproducibility issues due to random detachment of MIP particles during sensor use and an uneven surface coverage. A way to circumvent these problems is the direct grafting of a MIP layer from the substrate. Additionally, grafting of polymer films allows for the creation of more complex sensor designs as this strategy is less robust compared to coating/stamping methods and would allow for miniaturization of the sensor.

Miniaturized biosensors attract an increasing interest from the biomedical side where small sensors allowing for *in vivo* studies would grant valuable information with respect to the mechanics of pathologies and theranostics. However, to reach this goal, sensors require improved MIP stability and a homogenous coverage of the involved sensor elements to yield reliable results.

The most commonly used synthesis route towards MIP materials is conventional free radical polymerization, which is relatively straightforward and effective. However, as applications become more specialized the use of reversible deactivation radical polymerization (RDRP) is more and more considered. The most-used RDRP routes are atom transfer radical polymerization (ATRP),^[27,28] reversible addition fragmentation degenerative chain transfer (RAFT)^[29] and nitroxide mediated polymerization (NMP).^[30] RDRPs have been investigated for the synthesis of MIPs in how they influence the quality of the MIPs and their eventual affinity to their target.^[19,31,32] Generally, they provide a better control over the polymer matrix, which results in several benefits. Depending on the chosen polymerization strategy, these include the ability to post-modify the MIP,^[19] control film thicknesses^[18] and graft patterned receptor layers.^[33]

The use of RDRP for MIP synthesis is, however, not without problems. Specifically ATRP is hindered due to the fact that typically acidic monomers (or other strongly

H-bonding monomers) must be used to form the required pre-polymerization complexes between monomers and a chosen target molecule. Since ATRP is very sensitive to such monomers, polymerizations do not proceed with ease in such case, and surface grafting is almost prohibitive. In recent years, several solutions were proposed to circumvent this issue. Fantin *et al.* suggested to work in an acidic environment to prevent end-group cyclization.^[34] Michl *et al.* built on this by selecting SI-ARGET-ATRP and were able to graft poly(methacrylic acid) (PMAA) brushes with a film thickness of approximately 60 nm within 1 hour reaction time.^[35] However, since recognition of targets in MIPS can greatly depend on the formation of H-bonds this can be a troublesome solution. Haupt and coworkers reported the grafting of P(MAA-co-EGDMA) MIP films from SiO₂ nanoparticles and planar substrates using iridium catalyzed photoATRP.^[36] Polymerization was successful and they report the binding characteristics of the MIP grafted SiO₂ nanoparticles targeting testosterone and S-propranolol. In this case the abundance of cross-linker possibly prevented end-cyclization, which allowed for continuation of the polymerization in presence of the acidic monomer. Yet, this approach makes use of a transition metal catalyst, which must be avoided when developing sensors that may later be used in *in vivo* applications. Lately, we had shown that photoinitiated metal-free ATRP could be the answer to this problem, using a photoredox organocatalyst, namely 10-phenylphenothiazine (PTH) to mediate the polymerization.^[37,38] Using this method, we were able to graft PMAA brushes, with film thicknesses of around 6 nm on planar surfaces.^[39]

For producing a MIP sensor based on a photoinduced MIP grafting method, histamine was chosen as target molecule due to its wide occurrence in biological environments and availability of MIP recipes for MIP monolith synthesis.^[40-42] The human body utilizes histamine as a neurotransmitter in the brain and as part of the immune response.^[43,44] Less known is histamine's function in gut motility and the deregulation of histamine concentration in various diseases such as irritable bowel

syndrome.^[44–46] Besides biomedical applications, histamine is also found in various food products such as fermented vegetables and in spoiling fish.^[47] Although food safety and biomedical applications are quite different, they share the need for quick and easy detection methods. Electrochemical impedance spectroscopy is one of these methods and involves the application of an AC voltage between the sensor chip, which acts as the working electrode, and a counter electrode while the current and phase shift are monitored. The method is safe to perform inside the human body as long as voltages stay below 65 mV,^[48] quick, and necessary equipment comes at low cost. Binding of target molecules onto the MIPs can be monitored with this method due to the displacement of aqueous solution in the cavities by the less conductive target molecule, which increases the impedance due to a drop in capacity at the interface of the chip and sample liquid.^[49] **Figure 3.1** gives an overview on the used grafting technique and the working principle of the impedimetric sensor.

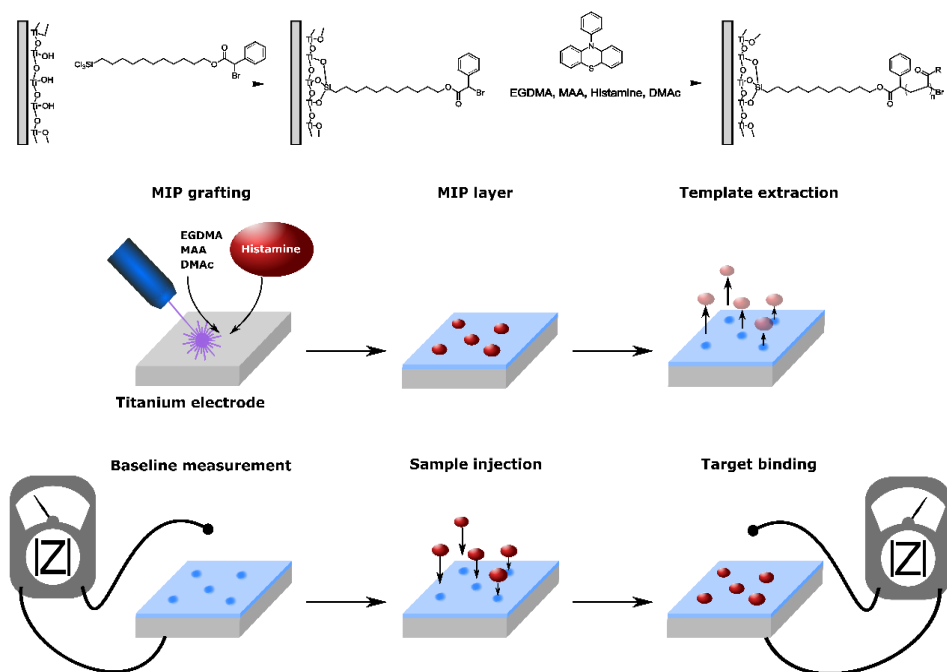


Figure 3.1. Schematic representation of the histamine MIP sensor production starting with the surface activation (top) with the immobilization of an ATRP initiator, MIP grafting through a metal-free ATRP procedure using phenyl phenothiazine (PTH) as the organocatalyst (middle) and sensor characterization (bottom).

In this work we present a metal-free synthesis route for the surface initiated grafting of a MIP film targeting histamine using a metal-free photoATRP. For this, MAA is copolymerized with ethylene glycol dimethacrylate (EGDMA) in presence of histamine to produce the cross-linked MIP matrix. The MIP films are grafted from planar titanium electrodes, which were chosen for their low resistivity and good biocompatibility, making them ideal for *in vivo* applications. We also introduce the usage of a pulsed UV excimer laser for initiation of the grafting reaction. In combination with a 2D scanner, this gives access to defined polymer patterns on a surface without the need of using a shadow mask, a feature that will be beneficial

in future studies towards multiple target MIP patterns (with the inclusion of non-imprinted planes).^[33] Yet, in here we focused on homogenous MIP layers that can be obtained from organocatalyzed ATRP laser grafting as a first proof of concept study. The composition of the obtained MIP films is discussed and subsequently the procedure is optimized and layers are characterized via impedance spectroscopy-based sensor measurements.

3.3 Experimental Section

3.3.1 Electrochemical Impedance Spectroscopy (EIS)

EIS measurements were performed with the Novocontrol Alpha-A High Performance Modular Measurement System (Novocontrol technologies GmbH & CO. KG, Montabaur, Germany) over a range of 100 mHz to 10 MHz at a signal amplitude of 65 mV. The Alpha Active Sample Cell which comes with the device contains reference capacitors and resistors which are used as a reference to increase accuracy.

3.3.2 Measurement cell

An in house developed measurement cell designed for impedance heat-transfer measurements as described by Stilman *et al.*^[52] was utilized for the impedance measurements. The measurement cell is composed of PEEK for chemical resistance and contains a viewing glass to allow visual inspection of the sensor chip. The connection to the back of the MIP or NIP sensor is made by connecting a wire to the copper heating table while the other wire is connected to the gold wire inside the liquid compartment through shielded cables. A PID controller regulates the temperature of the sensor cell to 37 °C to ensure a stable temperature during measurement.

3.3.3 Silanization of substrates

Titanium electrodes and silicon wafers ($1 \times 1 \text{ cm}^2$) were subsequently treated with Piranha solution, HCl (pH =1) and a $\text{NH}_4\text{OH}/\text{H}_2\text{O}_2$ mixture (1:1) with intermediate washing steps with demineralized water. The silicon wafers were functionalized additional to the titanium electrodes because the roughness of the titanium substrates didn't allow for proper GAATR-IR analysis. The substrates were transferred to the glove box in a Petri dish and submerged in dry toluene. The synthesized silane equipped with ATRP initiator was added in excess (10 μl for 10 substrates) together with a minimum of three equivalents of dry triethyl amine. ^1H NMR spectrum of the silane can be found in the appendix (Figure A2). The silanized samples were rinsed with toluene, THF, absolute EtOH and demineralized water and blown dry with a N_2 blowing gun. Reaction was confirmed via XPS (Figure A9) and ToF-SIMS (Figure A10)

3.3.4 MIP surface grafting

Purified stock solutions of MAA, EGDMA and Dimethyl acetamide (DMAc) were separately flushed with nitrogen for 15 minutes. Varying equivalents of both monomers (always 3 mmol in total) and 0.5 ml of DMAc were added to 1 mg of PTH under nitrogen atmosphere (^1H NMR spectrum of PTH is displayed in Figure A1). When producing MIPS a DMAc solution was saturated with histamine before use. A custom-made chamber loaded with a silanized substrate was thoroughly flushed with nitrogen and kept under pressure. The reaction mixture was subsequently transferred to the reaction chamber. The photo polymerization reaction was induced with a 351 nm pulsed excimer laser (ATLEX 1000-I, ATL Lasertechnik GmbH) featuring a $6 \times 8 \text{ mm}^2$ beam after passing through a prism. Energy was set to 1.5 mJ per pulse of around 4-6 ns. Pulse frequency was set to 100 Hz and the energy was reduced by a factor 100 by using a reflective filter. The laser was

set to pulse 60000 times, which equals a 10 min reaction procedure. Afterwards, the substrates were rinsed with THF, abs. EtOH and distilled water and blown dry with a N₂ blowing gun. The silicon wafers were analysed with GAATR-FTIR and the titanium electrodes were characterized using XPS (Figure A12) and ToF-SIMS (Figure A11). The MIP containing titanium electrodes (and non-imprinted counterparts) were characterized in the impedance sensor set-up.

3.4 Results and Discussion

3.4.1 Surface grafting of MIPs.

To develop a surface MIP protocol, the known recipe for bulk monolith MIP synthesis was used as reference. MIP efficiencies depend mostly on the choice of monomers, ratio of monomers and choice of porogen. In principle, no large difference between surface grafted and bulk polymerized MIPs should exist. Variations can, however be required in order to account for different reactivities when grafting chains compared to solution processes. Thus, as a starting point a 1:4 MAA:EGDMA ratio was chosen for the surface grafting based on monolith protocols.^[41] All reactions were initiated using a pulsed UV excimer laser operating at 351 nm. The laser repetition rate was 100 Hz and the energy per pulse was set to 1.5 mJ/pulse and attenuated via a factor 100 reflective filter. The 6 × 8 mm² laser beam is directly projected onto the substrate. To assess if control over the polymerization can be acquired, the reaction procedure time was varied between 0 and 10 minutes. After 10 minutes the risk to polymerize EGDMA in solution (via direct UV-initiation of the monomer) increases, which is undesirable and thus needs to be avoided. In earlier work, we had reported on the use of a fluorescent UV-lamp for the grafting of MAA brushes.^[39] Compared to broadband UV light sources, the laser appeared to be beneficial, as we previously observed significant EGDMA polymerization in solution before any detectable polymer grafting had occurred. The laser allows

for better tuning of light intensities and provides generally better preciseness. The high energy input per pulse provides fast initiation and therefore allows for surface grafting and stopping the reaction before the undesired polymerization in solution can take place.

The MIPS films were first grafted from planar silicon substrates as the low roughness is ideal for grazing angle ATR-FTIR analysis. The IR spectra of non-imprinted polymer films (these are cross-linked networks formed by the same MIPS recipe in absence of any template molecule), depicted in **Figure 3.2**, show the appearance of typical acrylate-related vibration bands with increasing reaction time. Spectra were normalized to the peak at 1233 cm^{-1} which can be assigned to the SiO_2 stemming from the substrate. The relative peak intensity at 1732 cm^{-1} (carbonyl) and 1169 cm^{-1} (C-O stretch), both being indicative of the ester and acid moieties per polymer repeat unit are plotted against the reaction time to visualize the progress of the reaction. A similar increase in peak intensity can be observed for both peak positions as should be expected. From the steady increase in peak intensity it can be concluded that film growth is continuous and that the film layer is becoming thicker with time.

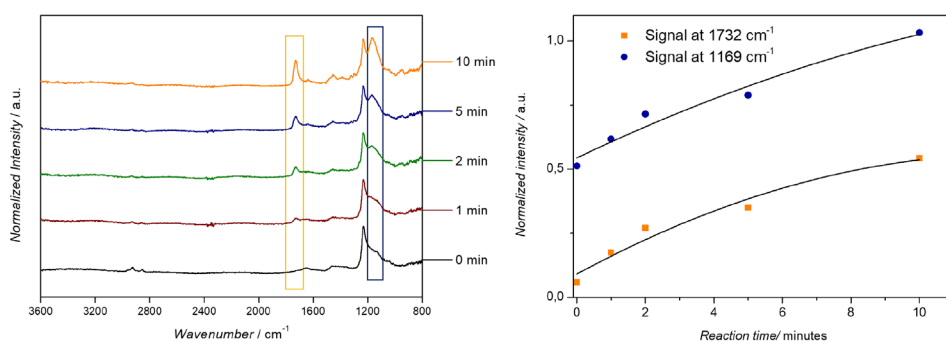


Figure 3.2. Normalized IR spectra of grafted P(MAA-co-EGDMA) films after varying reaction times (left). The relative intensities of the relevant peaks for the

methacrylic monomers (carbonyl at 1732 cm^{-1} and C-O stretch 1169 cm^{-1}) are plotted against reaction time (right).

After polymerization of a non-imprinted polymer (NIP) matrix was confirmed on silicon substrates, the procedure was transferred to titanium electrodes. Titanium is the superior metal compared to silicon to be used in impedance spectroscopy due to its low resistivity and hence presents the better electrode material in a biosensor. Since titanium has a higher surface roughness compared to the pristine silicon substrates employed in the first tests, no reliable grazing angle ATR spectra could be recorded. In order to confirm the success of polymerization and to check the composition of the polymer film, the samples were characterized via XPS and ToF-SIMS. Both methods give detailed insights into the chemical makeup of the surface grafts and allow for a near-quantitative analysis of the composition and homogeneity. To test if the monomers copolymerize during the grafting process in the same way as in solution, the ratio between the functional monomer MAA and cross-linker EGDMA was varied. When using a ratio of 1:4, with EGDMA in abundance, both ToF-SIMS and XPS (Figure A12) confirmed the presence of a thin polymer film evidenced by the clear presence of 2 characteristic peaks in the C 1s spectrum at 286.8 eV and 289.1 eV attributed to C-O and O=C-O respectively. [39] However, in XPS, the ratio of the O=C-O and C-O contributions had a value of ~ 0.8 and thus was comparable to the ratio obtained for a pure EGDMA polymer, only slightly higher. This did not unambiguously confirm the presence of MAA. When further increasing the MAA concentration by using ratios of 1:1, 2:1 and 4:1 (MAA:EGDMA) no significant increase of the O-C=O concentration was observed. The contribution of titanium was however significantly higher for the two highest MAA concentrations, indicating a thinner polymer film (Table A4). Considering the sampling depth of 8 to 10 nm achieved in XPS, the detection of the substrate signal indicates a thickness of the polymer film smaller than 8 nm. Titanium signals detected in ToF-SIMS were given in Figure A13. For ToF-SIMS, however,

an increase in the contribution of MAA was observed starting from a 2:1 ratio (MAA:EGDMA). When working with lower MAA concentrations, its contribution is distinguishable from pure EGDMA grafted samples. The evolution of the observed MAA contribution is displayed in **Figure 3.3**.

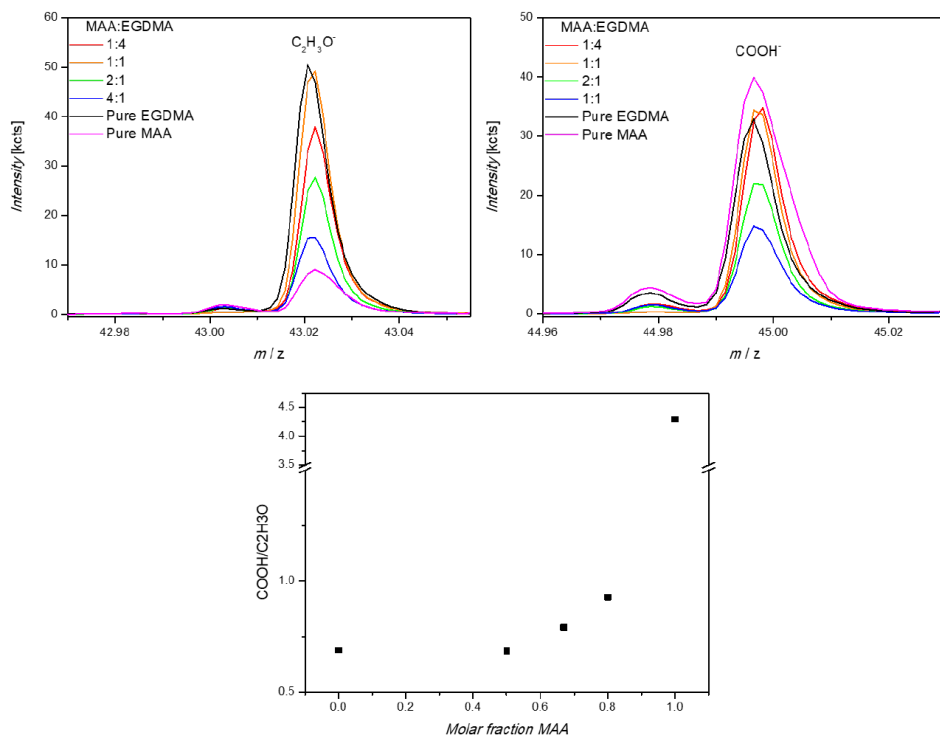


Figure 3.3. Ratio of molecular fragments, obtained via ToF-SIMS, specifically representing MAA ($COOH^+$, lower left) and EGDMA ($C_2H_3O^+$, upper left) plotted against the used monomer ratio to estimate the actual composition of the polymer film (upper right). The experimental monomer ratios are MAA:EGDMA 0:1, 1:4, 1:1, 2:1 and 4:1.

On first glance, XPS and ToF-SIMS seem to yield contradictory results. However, the hypothesis may be drawn that MAA is predominantly grafted at the end of the polymer chain, which is followed by a stop of film growth. This is in line with the relatively low film thicknesses observed, and also with our previous study where we also observed that MAA causes termination of chain growth before thicker brush layers can be formed.^[39] We assume that film thickness is more limited when MAA is copolymerized, resulting in thinner cross-linked films at higher MAA concentrations (and thus higher abundance of titanium in XPS analysis). This concomitantly can result in MAA being only present in the very top layer of the film, making an observable difference in ToF-SIMS, where only the topmost layer is visualized whereas in XPS the information stems here from the overall film. This results in a presence of MAA (and hence potential receptor sites) beyond a certain threshold (in this case 2:1 MAA:EGDMA). These hypotheses are backed-up by the sensor characterization assays, which are described in the next section.

3.4.2 Biomimetic measurements

After surface characterization had confirmed the presence of a cross-linked polymer film, and build-in of MAA on the film top layer, we proceeded to evaluate the quality of MIPs. Therefore, films were grafted in presence of the histamine target molecule, followed by washing out the target molecule from the surface after laser grafting. The MIP concept requires only formation of binding sites at the top of the polymer matrix, hence limited film thicknesses do not pose a problem, and also the incorporation of functional monomer only at the surface is in principle sufficient. Characterization of the formation of MIP receptor cavities is best directly evaluated by impedimetric sensor measurements. To evaluate the usability of the MIP coating for impedimetric biodetection of histamine dilutions in PBS were made ranging from 5 nanomolar to 1 micromolar concentrations. For each measurement a new sensor chip was placed onto the chip holder of the measurement cell and

after closing the cell and filling it with unspiked PBS the setup was left to stabilize for an hour to ensure equilibrium conditions. After one hour an impedance spectrum from 100 mHz to 10 MHz was taken by sweeping three times during 8 minutes. After completion of the sweeps the next concentration of histamine spiked PBS was injected and the sensor was left to stabilize for half an hour before taking the next impedance spectrum and this was repeated until the last concentration. The same experiments were performed with a NIP and with a MIP sensor which was exposed to histidine instead of histamine to evaluate the cross selectivity of the coating. Even though the binding of histamine to the MIP coating occurs at a fast rate the sensor should be left to stabilize due to the temperature dependency of the conductivity . After acquiring the spectra the data were analysed and plotted as impedance amplitude versus frequency graphs (Bode plots) such as shown in **Figure 3.4**. From these graphs, it was concluded that at low frequencies electrode polarization takes place, which causes the impedance to rise dramatically in that region. This effect is common for any metal electrode submerged into liquid as positively charged ions will be attracted to the negatively charged surface where they form a charged layer of ions. This so called double layer capacitor has a high impedance at low frequencies and decreases with increasing. At high frequencies in the MHz range the impedance decreases until it reaches a plateau where cable resistance, solution resistance and the resistance of the MIP layer dominates. The ideal frequency range for these measurements was determined to be from a few hundred hertz up to a few kilohertz. In this region the spectra of the different concentrations are clearly separated while in the lowest and highest region the effect size is negligible compared to the earlier described effects which are in play.

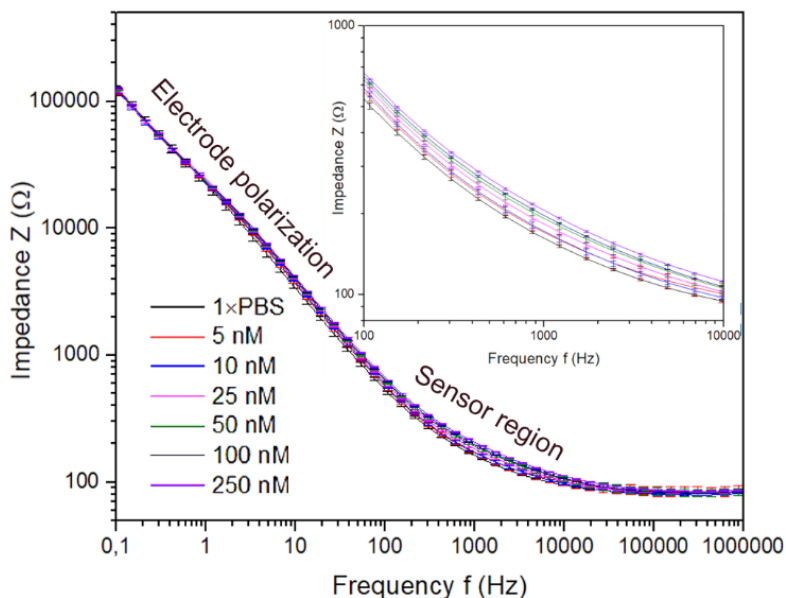


Figure 3.4. Bode plot of a MIP sensor measurement with indicated sensor region and electrode polarization in the low frequency region.

For the results displayed in **Figure 3.5**, 610 Hz was determined to be the optimal frequency. As can be seen from the graph the sensor responds even to the lowest concentration (5 nM) of histamine in PBS and keeps showing an increase in impedance amplitude for increasing concentrations. The Limit of Detection (LoD) was determined by taking the standard deviation of three impedance sweeps and multiplying it by three, this value is then used to acquire the corresponding concentration, which is around 3.4 nM. The ability to measure concentrations of histamine in the nanomolar range allows for various applications in both medical and a food industry context. Experiments with decreasing concentration have proven to be not feasible in a usable timeframe as the release of histamine from the MIP layer occurs at a low speed. The NIP gives barely any response to histamine, which proves it to be a capable control for non-specific binding due to the selective interaction of histamine with the sensor coating. The lack of response

of the NIP sensor is an important condition for the ability to perform differential measurements in complex matrices. Histidine however seems to interact with the MIP layer in a repeatable fashion. The decrease shown by histidine might be caused by increased conductivity of the solution or by molecular relaxations of histidine under influence of the AC signal.

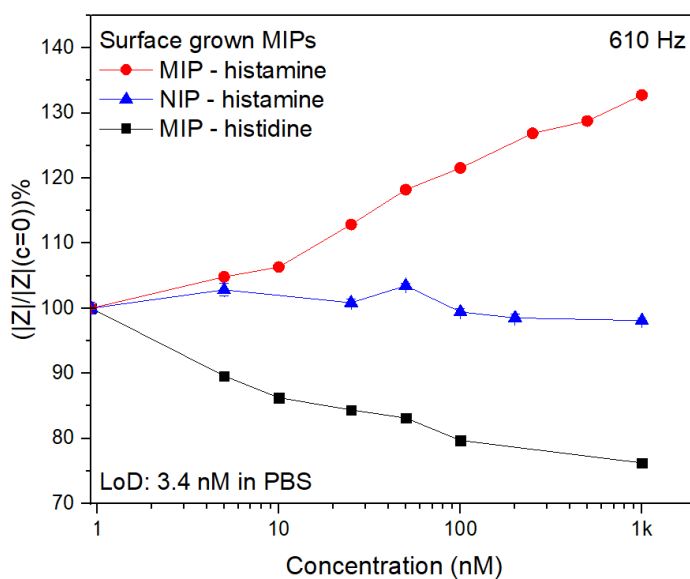


Figure 3.5. Dose-response curve of the MIP and NIP sensors at 610 Hertz for histamine and histidine. The limit of detection was determined to be 3.4 nM of histamine in PBS. The error margin is smaller than the symbol size and hence not clearly visible.

3.5 Conclusion

A planar titanium substrate was successfully functionalized with a histamine-molecularly imprinted polymer film using an organocatalyzed metal-free photoATRP. MIP polymer films were produced via laser grafting of mixtures of MAA and EDGMA, and the laser provided very high control over film growth and allowed for the formation of cross-linked layers without initiating any bulk polymerization in the solution above the substrate, a side reaction that was observed before when classical UV-lamps were used. Nevertheless, NIP and MIP polymer films with thicknesses of few nanometers could be produced via our procedure. The composition of the thin film was investigated via grazing angle ATR-FTIR, XPS and ToF-SIMS. These characterizations revealed the necessity of working with an excess of methacrylic acid to ensure formation of suitable binding sites on the polymer film surface compared to classical bulk MIP synthesis. The reason for the difference is not fully revealed, but it may be assumed that film growth is stopped or at least significantly hindered after first MAA monomer units are build-in, causing decreasing film thicknesses with increasing MAA content in the monomer solution and presence of polymerized MAA only at the film top layer. Formation of MIP receptor sites was, however, very successful. The response of the MIP film in impedimetric sensor measurements was strong enough that the absolute impedance can be used directly without any fitting as a measurement for the histamine concentration. This is indicative of a high sensitivity of the MIP, and hence abundant presence of suitable receptor sites. In contrast, the lack of response from the NIP film layers shows that the binding of histamine to the MIP is not unspecific. The NIP can be utilized as a correction factor to perform differential measurements for more complex matrices such as patient fluids or liquids in the food industry. The substantially increased surface coverage over traditional powder based MIPs and NIPs, and the inherently more

resilient coating are an advantage as this development allows for further miniaturization of the impedimetric sensor concept, and concomitantly for better reliability of the sensors, as the polymer films are covalently attached to the electrode substrates.

3.6 References

- [1] J. J. BelBruno, *Chem. Rev.* **2018**, acs.chemrev.8b00171.
- [2] B. Ara, M. Muhammad, M. Salman, R. Ahmad, N. Islam, T. ul H. Zia, *Appl. Water Sci.* **2018**, *8*, 41.
- [3] Z. Li, Z. Qian, S. Hu, T. Gong, Q. Xian, *Chemosphere* **2018**, *212*, 872–880.
- [4] I. Ahmad, W. A. Siddiqui, S. Qadir, T. Ahmad, *J. Mater. Res. Technol.* **2018**, *7*, 270–282.
- [5] C. Giovannoli, C. Passini, F. di Nardo, L. Anfossi, C. Baggiani, I. A. Nicholls, *Polymers (Basel)*. **2018**, *10*, 192.
- [6] Q. Liu, J. Wan, X. Cao, *Process Biochem.* **2018**, *70*, 168–178.
- [7] J. Bai, Y. Zhang, L. Chen, H. Yan, C. Zhang, L. Liu, X. Xu, *Mater. Sci. Eng. C* **2018**, *92*, 338–348.
- [8] V. R. A. Ferreira, M. A. Azenha, C. M. Pereira, A. Fernando Silva, *React. Funct. Polym.* **2018**, *131*, 283–292.
- [9] O. Parisi, M. Ruffo, L. Scrivano, R. Malivindi, A. Vassallo, F. Puoci, *Pharmaceuticals* **2018**, *11*, 92.
- [10] M. E. E. Alahi, S. C. Mukhopadhyay, L. Burkitt, *Sensors Actuators B Chem.* **2018**, *259*, 753–761.
- [11] R. Hu, R. Tang, J. Xu, F. Lu, *Anal. Chim. Acta* **2018**, *1034*, 176–183.

- [12] X. Lu, Y. Yang, Y. Zeng, L. Li, X. Wu, *Biosens. Bioelectron.* **2018**, *99*, 47–55.
- [13] Y. Wei, Q. Zeng, J. Huang, Q. Hu, X. Guo, L. Wang, *Chem. Commun.* **2018**, *54*, 9163–9166.
- [14] X. Yan, H. Li, X. Su, *TrAC Trends Anal. Chem.* **2018**, *103*, 1–20.
- [15] A. A. Ensafi, P. Nasr-Esfahani, B. Rezaei, *Sensors Actuators B Chem.* **2018**, *257*, 889–896.
- [16] J. Luan, T. Xu, J. Cashin, J. J. Morrissey, E. D. Kharasch, S. Singamaneni, *Anal. Chem.* **2018**, *90*, 7880–7887.
- [17] J. Liu, D. Yin, S. Wang, H.-Y. Chen, Z. Liu, *Angew. Chemie Int. Ed.* **2016**, *55*, 13215–13218.
- [18] T. Kajisa, W. Li, T. Michinobu, T. Sakata, *Biosens. Bioelectron.* **2018**, *117*, 810–817.
- [19] S. Beyazit, B. Tse Sum Bui, K. Haupt, C. Gonzato, *Prog. Polym. Sci.* **2016**, *62*, 1–21.
- [20] E. Roy, S. Patra, S. Saha, D. Kumar, R. Madhuri, P. K. Sharma, *Chem. Eng. J.* **2017**, *321*, 195–206.
- [21] M. Peeters, P. Csipai, B. Geerets, A. Weustenraed, B. van Grinsven, R. Thoelen, J. Gruber, W. De Ceuninck, T. J. Cleij, F. J. Troost, P. Wagner, *Anal. Bioanal. Chem.* **2013**, *405*, 6453–60.
- [22] K. Eersels, B. van Grinsven, M. Peeters, T. J. Cleij, P. Wagner, Springer, Berlin, Heidelberg, **2017**, pp. 1–25.

- [23] F. Lisdat, D. Schäfer, *Anal. Bioanal. Chem.* **2008**, *391*, 1555–1567.
- [24] A. Diouf, S. Motia, N. El Alami El Hassani, N. El Bari, B. Bouchikhi, *J. Electroanal. Chem.* **2017**, *788*, 44–53.
- [25] S. A. Nabavi, G. T. Vladislavljević, A. Wicaksono, S. Georgiadou, V. Manović, *Colloids Surfaces A Physicochem. Eng. Asp.* **2017**, *521*, 231–238.
- [26] H. Sun, J.-P. Lai, F. Chen, D.-R. Zhu, *Anal. Bioanal. Chem.* **2015**, *407*, 1745–1752.
- [27] M. Kato, M. Kamigaito, M. Sawamoto, T. Higashimura, *Macromolecules* **1995**, *28*, 1721–1723.
- [28] J.-S. Wang, K. Matyjaszewski, *J. Am. Chem. Soc.* **1995**, *117*, 5614–5615.
- [29] J. Chiefari, Y. K. Chong, F. Ercole, J. Krstina, J. Jeffery, T. P. T. Le, R. T. A. Mayadunne, G. F. Meijs, C. L. Moad, G. Moad, E. Rizzardo, S. H. Thang, *Macromolecules* **1998**, *31*, 5559–5562.
- [30] J. Nicolas, Y. Guillaneuf, C. Lefay, D. Bertin, D. Gigmes, B. Charleux, *Prog. Polym. Sci.* **2013**, *38*, 63–235.
- [31] M. J. Garcia-Soto, K. Haupt, C. Gonzato, *Polym. Chem.* **2017**, *8*, 4830–4834.
- [32] M. R. Halhalli, B. Sellergren, *Polym. Chem.* **2015**, *6*, 7320–7332.
- [33] J. Laun, Y. De Smet, E. Van de Reydt, A. Krivcov, V. Trouillet, A. Welle, H. Möbius, C. Barner-Kowollik, T. Junkers, *Chem. Commun.* **2018**, *54*, 751–754.

- [34] M. Fantin, A. A. Isse, A. Venzo, A. Gennaro, K. Matyjaszewski, *J. Am. Chem. Soc.* **2016**, *138*, 7216–7219.
- [35] T. D. Michl, D. Jung, A. Pertoldi, A. Schulte, P. Mocny, H.-A. Klok, H. Schönherr, C. Giles, H. J. Griesser, B. R. Coad, *Macromol. Chem. Phys.* **2018**, 1800182.
- [36] Z. Adali-Kaya, B. Tse Sum Bui, A. Falcimaigne-Cordin, K. Haupt, *Angew. Chemie* **2015**, *127*, 5281–5284.
- [37] N. J. Treat, H. Sprafke, J. W. Kramer, P. G. Clark, B. E. Barton, J. Read de Alaniz, B. P. Fors, C. J. Hawker, *J. Am. Chem. Soc.* **2014**, *136*, 16096–101.
- [38] E. H. Discekici, C. W. Pester, N. J. Treat, J. Lawrence, K. M. Mattson, B. Narupai, E. P. Toumayan, Y. Luo, A. J. McGrath, P. G. Clark, et al., *ACS Macro Lett.* **2016**, *5*, 258–262.
- [39] G. Ramakers, A. Krivcov, V. Trouillet, A. Welle, H. Möbius, T. Junkers, *Macromol. Rapid Commun.* **2017**, *38*, 1700423.
- [40] M. B. Passani, P. Panula, J.-S. Lin, *Front. Syst. Neurosci.* **2014**, *8*, 64.
- [41] M. Peeters, F. J. Troost, R. H. G. Mingels, T. Welsch, B. van Grinsven, T. Vranken, S. Ingebrandt, R. Thoelen, T. J. Cleij, P. Wagner, *Anal. Chem.* **2013**, *85*, 1475–83.
- [42] A. Sahebhasagh, G. Karimi, S. A. Mohajeri, *Food Anal. Methods* **2013**, *7*, 1–8.
- [43] L. Maintz, N. Novak, *Am. J. Clin. Nutr.* **2007**, *85*, 1185–1196.

- [44] E. Kovacova-Hanuszkova, T. Buday, S. Gavliakova, J. Plevkova, *Allergol. Immunopathol. (Madr)*. **2015**, *43*, 498–506.
- [45] J. H. Park, P.-L. Rhee, H. S. Kim, J. H. Lee, Y.-H. Kim, J. J. Kim, J. C. Rhee, *J. Gastroenterol. Hepatol.* **2006**, *21*, 71–78.
- [46] A. Rijnierse, F. P. Nijkamp, A. D. Kraneveld, *Pharmacol. Ther.* **2007**, *116*, 207–235.
- [47] P. S. Borade, C. C. Ballary, D. K. C. Lee, *Resuscitation* **2007**, *72*, 158–160.
- [48] S. H. Wright, *Adv. Physiol. Educ.* **2004**, *28*, 139–142.
- [49] M. Peeters, F. J. Troost, B. van Grinsven, F. Horemans, J. Alenus, M. S. Murib, D. Keszthelyi, A. Ethirajan, R. Thoelen, T. J. Cleij, P. Wagner, *Sensors and Actuators B-Chemical* **2012**, *171*, 602–610.

Chapter 4

Photoiniferter surface grafting of
poly(methyl acrylate) using xanthates

4.1 Introduction

Methods to alter surface characteristics have been investigated intensively in recent years. Surface properties define the interaction of materials with their direct environment and can determine their fate. This is especially important within a biomedical context, where parameters like biocompatibility and toxicity come into play. The grafting of synthetic polymers to modify surfaces is interesting as a vast library of monomers is available, allowing for precise fine tuning of the surface properties. By choosing a reversible deactivation radical polymerization (RDRP) reaction, the polymer film thickness can be controlled and desired end-groups can be obtained.^[1] The latter grants the option to modify the surface further through chain extensions, formations of block copolymers or through bio-conjugation with the addition of biomolecules.

On planar substrates, combining the advantages of controlled polymerizations with the advantages of photo-initiation allows for the engineering of complex structures and patterns with the addition of spatial and temporal control over the reaction.^[2-4] Two of the most studied and best known photoRDRP strategies for the surface grafting of polymers are photo-initiated atom transfer radical polymerization (photoATRP) and photo reversible addition-fragmentation degenerative chain-transfer (photoRAFT)^[2,5-7] For photoATRP, a catalyst is used to reduce the activator upon photoexcitation, yielding a radical accessible for propagation.^[8,9] Although initially requiring metal/ligand complexes, the employment of organocatalysts was reported more recently.^[10,11] In photoRAFT, although not strictly required, similar catalysts are often employed to enhance polymerization rate and initiation efficiency.^[6,12-15] A more direct approach is through direct excitation and activation of the thiocarbonylthio moiety present in RAFT agents. The RAFT agent will subsequently generate a radical to initiate the polymerization reaction. This is called photoiniferter, as the transfer agent is involved in *initiation*, *transfer* and

termination. This reaction was first described by Otsu and coworkers, who used dithiocarbamates to obtain the first controlled "living" radical polymerization.^[16,17] Despite dithiocarbamates being the benchmark photoiniferter agents for more than a decade, polymerizations were relatively inefficient and slow. Additionally, poor control was commonly observed due to dithiocarbamates being poor transfer agents. Trithiocarbonates (TTCs) were explored for their potential as iniferter agents.^[18,19] Qiao and coworkers presented a photoiniferter process using a TTC excited via blue light irradiation ($\lambda_{\text{max}} = 460 \text{ nm}$).^[20] This way photodegradation of the TTC, which is a risk when exposed to UV light, is avoided by selectively targeting the $n\text{-}\pi^*$ transition.^[21] Conversions up to 95% after 16 h reaction time and dispersities as low as 1.06 were reported.

Additionally, xanthates proved to be good iniferter agents for the polymerization of vinyl esters through UV irradiation, providing good control over the mass distribution ($\mathcal{D} = 1.2\text{-}1.3$). Conversions $> 80\%$ were observed for 90 minutes reaction time, greatly exceeding the polymerization rate of TTCs.^[22] This was confirmed by Carmean *et al.* where TTCs and xanthates were compared for the production of ultra-high molecular weight poly(dimethylacrylamide), reducing reaction time from 10 hours to 30 minutes.^[23] Reports of blue light initiation of xanthates show diminished time benefits.^[24,25]

Surface initiated photoiniferter is left relatively unexplored. After introducing photoiniferter for the surface grafting of polymers using dithiocarbamates in 1996,^[26] photoiniferter from nanoparticles using TTC was reported only very recently.^[27] To the best of our knowledge no photoiniferter grafting from planar substrates using xanthates, as displayed in **Figure 4.1**, or using TTCs has been reported until date. The reason xanthates are also mentioned is that they are interesting for their fast initiation, which might be necessary to compensate for the absence of the undesired exogenous catalysts.

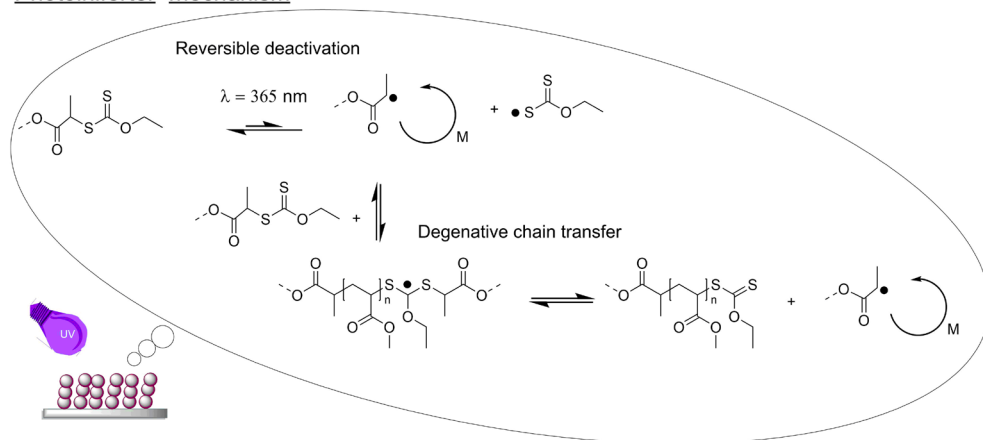
Photoiniferter mechanism

Figure 4.1. Schematic representation of photoiniferter mechanism using xanthates

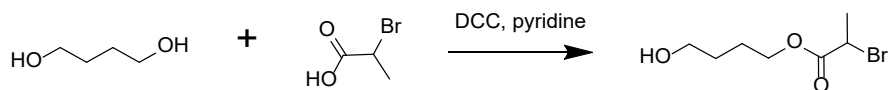
The fact that photoiniferter requires no additional catalyst makes it highly interesting for bio applications. A polymer application where photoiniferter exhibited highly promising results is molecularly imprinted polymers (MIPs), where exploiting the controlled nature of photoRDRPs results in improved binding efficiency.^[28] In the quest to produce *in vivo* MIP sensors, direct surface-grown MIPs allow for better surface coverage, better reproducibility and sensor miniaturization.^[29] Surface initiated photomediated RDRP allows for the creation of complex patterns in a controlled fashion.^[4] Acidic monomers are highly prevalent in MIP research as they tend to form hydrogen bonds for target recognition. This can be problematic when using photoATRP since ATRP is typically not compatible with the acidic functional monomers. Photoiniferter can be a great alternative as it is compatible with a vast library of monomers, including acids.

In this chapter the surface grafting of poly(methyl acrylate) (PMA) from planar SiO_2 substrates using immobilized xanthate iniferters through UV irradiation is presented. The polymer film was characterized using Fourier transform

infrared spectroscopy (FTIR), atomic force microscopy (AFM), x-ray photoelectron spectroscopy (XPS) and time-of-flight secondary ion mass spectrometry (ToF-SIMS). The results were critically assessed and discussed.

4.2 Experimental Section

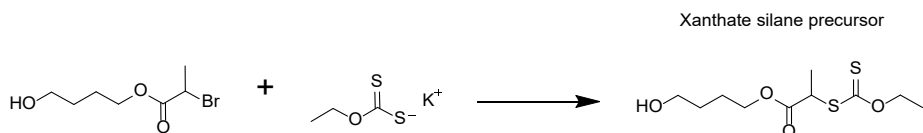
4.2.1 Synthesis of 4-hydroxybutyl 2-bromopropanoate



Scheme 4.1. Synthesis of 4-hydroxybutyl 2-bromopropanoate.

A mixture of butanediol (7.30 g, 81 mmol), *N,N'*-dicyclohexylcarbodi-imide or DCC (4.13 g 20 mmol) and pyridine (1 mL, 12 mmol) is cooled on ice. Subsequently 2-bromopropionic acid (1.5 mL, 16.7 mmol) dissolved in acetone (14 mL) was added dropwise and left to stir overnight. The mixture was filtered and extracted with ethyl acetate and brine, washed 2 times with 5% HCl and another two times with brine. Ultimately the product was purified over a column (hexane/ethyl acetate 1/1) and analyzed with ¹H NMR and ESI-MS. Yield = 29% (1.10 g). ¹H NMR (400 MHz, Chloroform-*d*) δ 4.35 (t, *J* = 7.4 Hz, 1H), 4.19 (t, *J* = 6.5 Hz, 2H), 3.66 (t, *J* = 6.7 Hz, 2H), 1.80 (d, *J* = 6.9 Hz, 3H), 1.78 – 1.71 (m, 2H), 1.67 – 1.60 (m, 2H). (Figure A14).

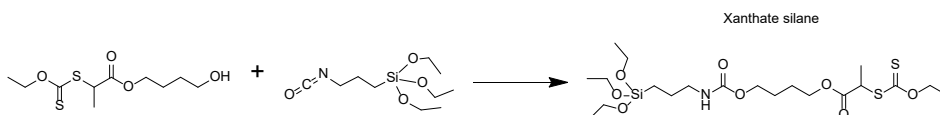
4.2.2 Synthesis of 4-hydroxybutyl 2-((ethoxycarbonothioyl)thio)propanoate (xanthate silane precursor)



Scheme 4.2. Synthesis of xanthate silane precursor.

To synthesize the xanthate silane precursor, 550 mg (1.18 eq) of 4-hydroxybutyl 2-bromopropanoate was dissolved in 5 mL ethanol with 335 mg (1 eq) of potassium ethyl xanthate salt and stirred over night at room temperature. The mixture was extracted two times with diethylether/pentane (2/1), two times washed with distilled water and dried with MgSO₄. The product was purified by recycling on size exclusion chromatography (SEC) with chloroform as eluents. Ultimately the product was analyzed with ¹H NMR. Yield = 45% (250 mg). ¹H NMR (400 MHz, Chloroform-d) δ 4.63 (q, J = 7.1 Hz, 2H), 4.38 (q, J = 7.4 Hz, 1H), 4.19 (t, J = 6.5 Hz, 2H), 3.68 (t, J = 6.7 Hz, 2H), 1.81 – 1.71 (m, 2H), 1.69 – 1.60 (m, 2H), 1.57 (d, J = 7.4 Hz, 3H), 1.42 (t, J = 7.1 Hz, 3H). (Figure A15).

4.2.3 Synthesis of 4,4-diethoxy-9-oxo-3,10-dioxo-8-aza-4-silatetradecan-14-yl 2-((ethoxycarbonothioyl)thio)propanoate (Xanthate silane)



Scheme 4.3 Synthesis of Xanthate silane.

4.3 Results and Discussion

Prior to grafting, the silicon wafers were activated for photoiniferter by immobilizing xanthate containing silanes. The selection of xanthates over TTCs is based on the fast photolysis rate of the former in UV light.^[23] Although mediocre control is reported in combination with acrylates,^[30] fast generation of surface radicals can be beneficial for the induction of surface grafting. Fast photolysis concomitantly leads to the hypothesis that reversible deactivation is expected to be the predominant control mechanism with respect to degenerative chain transfer.^[23]

First, the xanthate moiety was incorporated through a widely used substitution reaction in the synthesis of RAFT agents, substituting bromine for sulfur from the xanthate salt.^[31] Subsequently, the R-group was provided with an alcohol group. This allows the iniferter agent to be tethered to 3-aminopropyltriethoxysilane (APTES) via the R-group approach, with the formation of a urethane link. This is a fast and easy reaction, often exhibiting quantitative yields.^[32] Attaching the R-group was selected over the Z-group as the propagating radicals were in this way kept on the surface, minimalizing the generation of radicals in solution and thus solution polymerization.^[1]

Silanized and PMA grafted silicon substrates were characterized with XPS and ToF-SIMS to confirm and assess the success of xanthate immobilization and polymer grafting. To confirm silanization, ToF-SIMS was able to nicely detect the sulfur containing fragments as depicted in **Figure 4.2**. Additionally, it verified the presence of the ethyl ester fragment and CNO⁻ corresponding to the urethane functionality in the silane spacer. In contrast to the CNO⁻ fragment, which is still detectable after polymerization, the sulfur signal has decreased to the level of the blank sample without silane as can be seen in **Figure 4.2A**. This could indicate degradation of the xanthate functionality upon UV radiation. The grafting of PMA was confirmed with the detection of CH₃O⁻ (the pending methyl ester) and C₄H₅O₂⁻,

which were clearly detectable in ToF-SIMS. As a control experiment, the exact same procedure for the grafting of PMA was repeated on blank silicon substrates to rule out physisorption of methyl acrylate. ToF-SIMS confirmed that physisorption was indeed not the case as the characteristic peaks for PMA were not detectable.

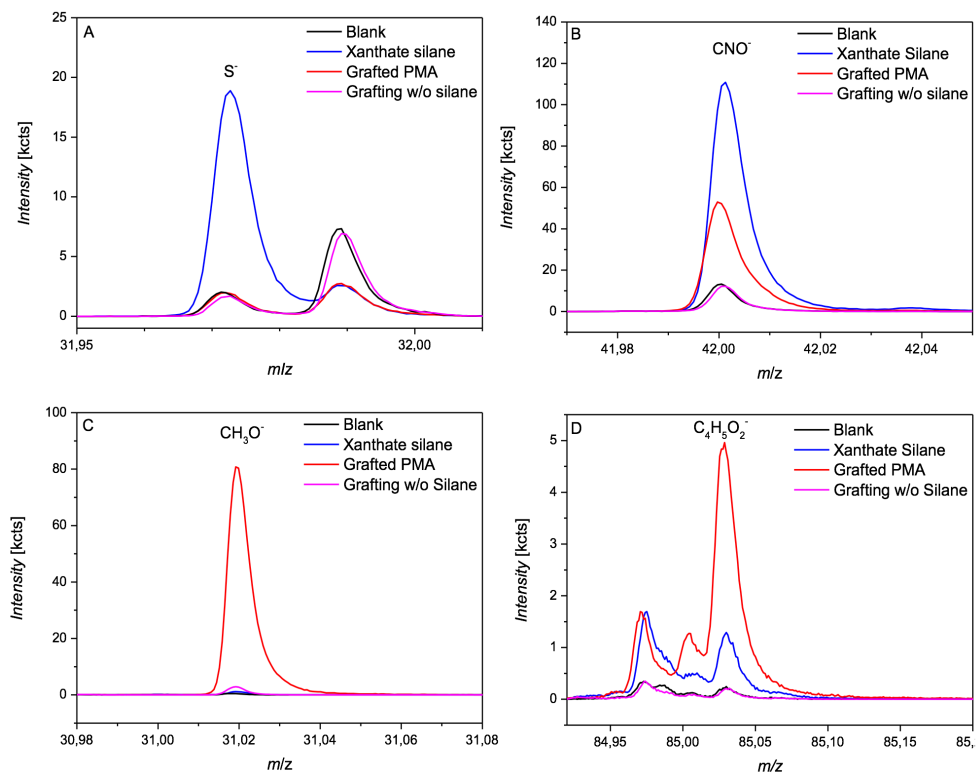


Figure 4.2. Fragments originating from the immobilized xanthate silane and grafted PMA are visualized in ToF-SIMS. A) Represents the sulfur stemming from the xanthate. B) represents the urethane moiety in the silane spacer. C and D both represent PMA.

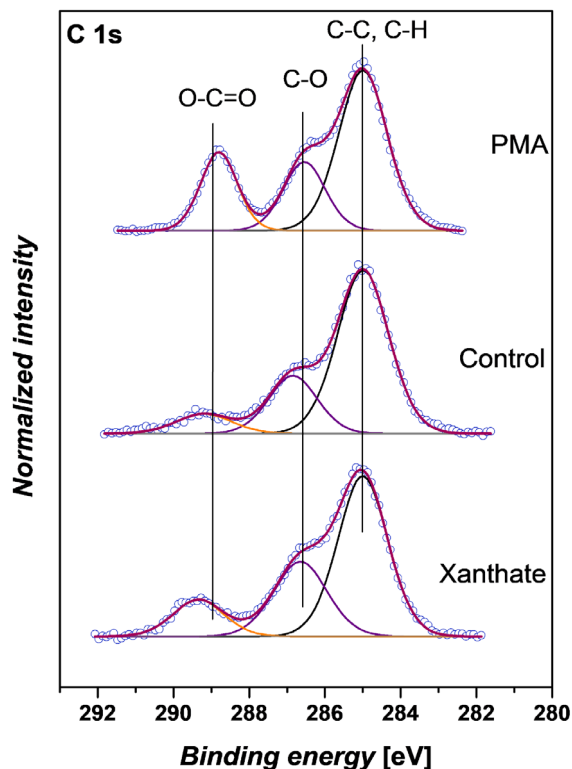


Figure 4.3. XPS spectra showing the contribution of C1s electrons for a PMA grafted sample (top), control experiment of grafting PMA without immobilized xanthate (middle) and a silanized silicon substrate (bottom)

In XPS, the xanthate would be mainly represented by the 2s or 2p electrons from the sulfur atoms, which were in this experiment not observed. This indicates a low grafting density since the sulfur was detected in ToF-SIMS, which is the more sensitive technique. The next step comprising the grafting of PMA from the silanized silicon wafers was visualized with XPS and depicted in **Figure 4.3**. XPS confirms the presence of the PMA through the relative contributions of the C 1s electrons at 289 eV, stemming from the ester and at 287 eV originating

from the methyl group. The experimental ratio of these peaks resembles the theoretical ratio of 1. ToF-SIMS confirms a successful silanization and XPS and ToF-SIMS proof a subsequent grafting of PMA from the xanthate functionalized silicon substrates. The possible loss of end-groups through the degradation of the xanthate as observed in ToF-SIMS can however be problematic concerning chain extensions, specific post-modification reactions and loss of control over the polymerization reaction.

To assess if control over film thickness can be achieved, the procedure was repeated at varying reaction times. Wafers exposed for 0, 10, 20, 30, 45 and 60 minutes were analyzed with grazing angle FTIR. When comparing the peak surface area corresponding to the carbonyl peak at 1740 cm^{-1} to the reaction time a positive correlation was observed as displayed in **Figure 4.4**. As the carbonyl peak is present in the acrylic monomer this is a relative measure for the amount of grafted PMA. The positive trend with increasing reaction time is a desired observation, which confirms a continuous film growth over time. After a reaction time of 60 minutes, undesired polymerization in solution was observed.

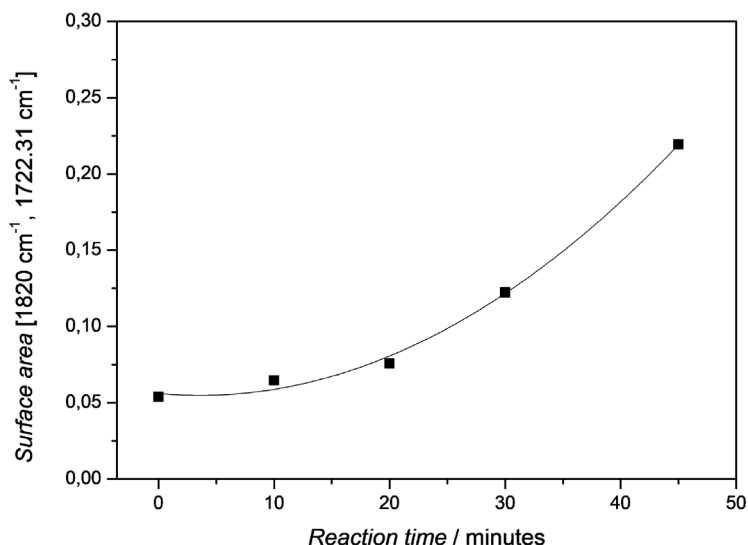


Figure 4.4. Plot displaying the evolution of the carbonyl vibration at 1740 cm^{-1} (grazing angle FTIR) against reaction time. The figure depicts the surface area of the peak against reaction time.

The PMA grafted samples were characterized with AFM. Topography of the polymer film was visualized and a scratch test was performed to determine the film thickness. AFM images, 2D and 3D, are displayed in **Figure 4.5**. After 30 minutes a smooth polymer film was obtained with a film thickness of 25 nm. 15 minutes reaction time yielded a film thickness of 6.5 nm (Figure A17). Conventionally, to obtain information on the molecular weight of the grafted polymer brushes and the dispersity of the mass distribution, cleavable groups are introduced near the anchoring point of the brush, which is then analyzed via SEC. Using surface initiated ATRP, Spencer and coworkers reported a PMA brush size of approximately $75000\text{ g}\cdot\text{mol}^{-1}$ for a grafting density of $0.45\text{ chains}\cdot\text{nm}^{-2}$ and a film thickness of $\pm 45\text{ nm}$.^[33] Based on these results, 25 nm for the photoiniferter grafted PMA would indicate a brush size of at least $40000\text{ g}\cdot\text{mol}^{-1}$. This estimation has to be taken

with care since the grafting density is unknown but assumed to be low according to the lack of sulfur detected in XPS. From the obtained data it was not possible to predict the polydispersity of the grafted PMA brushes.

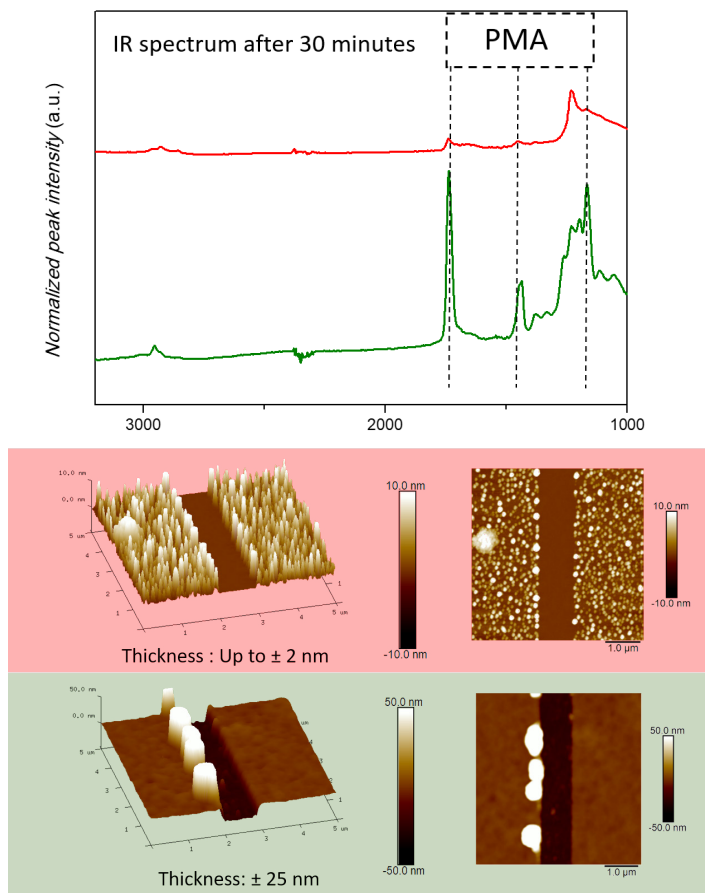


Figure 4.5. Comparison of results showing the discrepancies at identical reaction procedures. Samples were exposed to UV for 30 minutes. Left an IR spectra are depicted with characteristic PMA vibrations annotated with dotted line. Green indicates the results for a smooth polymer film. Red indicates the results for polymer “mushrooms”. AFM images of the scratch test including 3D images (middle) and top down (right) are presented.

Results were however suffering from significant reproducibility issues. Discrepancies for samples prepared with identical reaction procedures are depicted in **Figure 4.5**. AFM revealed the absence of a smooth polymer film, but confirmed the formation of mushroom shaped spots scattered across the surface. After 30 minutes reaction time, mushroom heights were observed around 2 nm. 45 min (3 nm), 20 and 10 min (both around 0.5 nm) were depicted in Figure A18 (appendix). IR confirmed the decrease in polymeric material with a significant decrease in relevant peak intensities.

The absence of a smooth polymer film and the presence of polymer “mushrooms” suggests a low density of initiation spots possibly caused by a low grafting density of the immobilized xanthate silanes. Another option is the partial loss of xanthate moieties, likely caused through photodegradation. However, since the silanized samples were kept in the dark after silanization, the odds of degradation of the light sensitive xanthate were reduced as much as possible. Literature furthermore shows that at low grafting densities, the polymer chains curl up in a mushroom-like formation, which was confirmed with AFM. Zheng *et al.*^[34] show the correlation between grafting density and film thickness, with a mushroom height of 8 nm increasing to 41 nm in a planar phase. This indicates that the actual molecular weight of the polymer brushes is not necessarily much different for the mushroom shaped polymers and smooth polymer surfaces. Until date no definite explanation can be given for these reproducibility issues. It is assumable that an unknown factor is interfering with the silanization reaction as the discrepancies were observed between batches of silanized samples and not between samples of the same batch. The shelf-life of the silane should also be considered, but up until now this is assumed to be of a lesser influence since no correlation was observed between the age of the silane or the age of the silanized sample batch at the moment of polymerization. Further research is required to reach the full potential of this grafting procedure and before definite conclusions about its feasibility can be drawn.

4.4 Conclusion

PMA brushes were successfully grafted from planar silicon wafers using xanthate for surface initiated photoiniferter, induced by a UV fluorescent tube lamp. The use of xanthate or TTCs for this purpose is to the best of our knowledge not yet reported in literature. ToF-SIMS confirmed successful xanthate immobilization and PMA grafting. XPS confirmed the presence of PMA, but detected no sulfur, indicating a low grafting density. A film thickness of around 25 nm was obtained after 30 minutes reaction time. A positive trend between reaction time and the carbonyl vibration peak intensity was observed in IR indicating an increasing monomer conversion with increasing reaction time. However, reproducibility issues were revealed with IR and AFM, showing significant discrepancies between identical reaction procedures. Smooth polymer films and the formation of mushrooms were observed. As mushrooms are a sign of low grafting density, issues during silanization are assumed to be a likely explanation. However, no definite answer could yet be given and further research into this issue is required to improve the feasibility of this reaction procedure. Surface initiated photoiniferter is despite these issues a labor friendly procedure (only monomer and solvent need to be added). Optimization of this grafting strategy, or surface initiated photoiniferter strategies overall, are therefore interesting developments towards grafting of controllable polymer films and patterns.

4.5 References

- [1] J. O. Zoppe, N. C. Ataman, P. Mocny, J. Wang, J. Moraes, H. A. Klok, *Chem. Rev.* **2017**, *117*, 1105–1318.
- [2] M. Chen, M. Zhong, J. A. Johnson, *Chem. Rev.* **2016**, *116*, 10167–10211.
- [3] N. Zhu, X. Hu, Z. Fang, K. Guo, *ChemPhotoChem* **2018**, DOI 10.1002/cptc.201800032.
- [4] J. Laun, Y. De Smet, E. Van de Reydt, A. Krivcov, V. Trouillet, A. Welle, H. Möbius, C. Barner-Kowollik, T. Junkers, *Chem. Commun.* **2018**, *54*, 751–754.
- [5] J. F. Quinn, L. Barner, C. Barner-Kowollik, E. Rizzardo, T. P. Davis, *Macromolecules* **2002**, *35*, 7620–7627.
- [6] T. G. McKenzie, Q. Fu, M. Uchiyama, K. Satoh, J. Xu, C. Boyer, M. Kamigaito, G. G. Qiao, *Adv. Sci.* **2016**, *3*, 1500394.
- [7] X. Pan, M. A. Tasdelen, J. Laun, T. Junkers, Y. Yagci, K. Matyjaszewski, *Prog. Polym. Sci.* **2016**, *62*, 73–125.
- [8] E. Frick, A. Anastasaki, D. M. Haddleton, C. Barner-Kowollik, *J. Am. Chem. Soc.* **2015**, *137*, 6889–6896.
- [9] S. Dadashi-Silab, S. Doran, Y. Yagci, *Chem. Rev.* **2016**, *116*, 10212–10275.
- [10] N. J. Treat, H. Sprafke, J. W. Kramer, P. G. Clark, B. E. Barton, J. Read de Alaniz, B. P. Fors, C. J. Hawker, *J. Am. Chem. Soc.* **2014**, *136*, 16096–101.
- [11] G. M. Miyake, J. C. Theriot, *Macromolecules* **2014**, *47*, 8255–8261.
- [12] M. Chen, J. A. Johnson, *Chem. Commun.* **2015**, *51*, 6742–6745.
- [13] J. C. Theriot, G. M. Miyake, C. A. Boyer, *ACS Macro Lett.* **2018**, *7*, 662–666.
- [14] J. Yeow, R. Chapman, J. Xu, C. Boyer, *Polym. Chem.* **2017**, *8*, 5012–5022.
- [15] J. Xu, K. Jung, A. Atme, S. Shanmugam, C. Boyer, *J. Am. Chem. Soc.* **2014**, *136*, 5508–5519.
- [16] T. Otsu, M. Yoshida, T. Tazaki, *Die Makromol. Chemie, Rapid Commun.*

- 1982**, 3, 133–140.
- [17] T. Otsu, A. Kuriyama, *J. Macromol. Sci. Part A - Chem.* **1984**, 21, 961–977.
- [18] H. Zhou, J. A. Johnson, *Angew. Chemie* **2013**, 125, 2291–2294.
- [19] H. Wang, Q. Li, J. Dai, F. Du, H. Zheng, R. Bai, *Macromolecules* **2013**, 46, 2576–2582.
- [20] T. G. McKenzie, Q. Fu, E. H. H. Wong, D. E. Dunstan, G. G. Qiao, *Macromolecules* **2015**, 48, 3864–3872.
- [21] T. G. McKenzie, L. P. da M. Costa, Q. Fu, D. E. Dunstan, G. G. Qiao, B. Klumperman, S. H. Thang, D. Nüsse, H. Schroeder, R. Wacker, R. Breinbauer, C. M. Niemeyer, H. Waldmann, *Polym. Chem.* **2016**, 7, 4246–4253.
- [22] M. Y. Khan, M.-S. Cho, Y.-J. Kwark, *Macromolecules* **2014**, 47, 1929–1934.
- [23] R. N. Carmean, T. E. Becker, M. B. Sims, B. S. Sumerlin, *Chem* **2017**, 2, 93–101.
- [24] J. Li, X. Pan, N. Li, J. Zhu, X. Zhu, *Polym. Chem.* **2018**, 9, 2897–2904.
- [25] C. Ding, C. Fan, G. Jiang, X. Pan, Z. Zhang, J. Zhu, X. Zhu, *Macromol. Rapid Commun.* **2015**, 36, 2181–2185.
- [26] T. Matsuda, Y. Nakayama, *Macromolecules* **1996**, 99, 8622–8630.
- [27] A. Bagheri, Z. Sadrearhami, N. N. M. Adnan, C. Boyer, M. Lim, *Polymer (Guildf)*. **2018**, 151, 6–14.
- [28] M. J. Garcia-Soto, K. Haupt, C. Gonzato, *Polym. Chem.* **2017**, 8, 4830–4834.
- [29] R. I. Boysen, L. J. Schwarz, D. V. Nicolau, M. T. W. Hearn, *J. Sep. Sci.* **2017**, 40, 314–335.
- [30] S. Perrier, P. Takolpuckdee, *J. Polym. Sci. Part A Polym. Chem.* **2005**, 43, 5347–5393.
- [31] C. J. Ferguson, R. J. Hughes, D. Nguyen, B. T. T. Pham, R. G. Gilbert, A. K. Serelis, C. H. Such, B. S. Hawket, *Macromolecules* **2005**, 38, 2191–2204.
- [32] C. Barner-Kowollik, F. Bennet, M. Schneider-Baumann, D. Voll, T. Rölle, T.

- Fäcke, M.-S. Weiser, F.-K. Bruder, T. Junkers, *Polym. Chem.* **2010**, *1*, 470.
- [33] C. Kang, R. Crockett, N. D. Spencer, *Polym. Chem.* **2016**, *7*, 302–309.
- [34] X. Zhou, X. Wang, Y. Shen, Z. Xie, Z. Zheng, *Angew. Chemie Int. Ed.* **2011**, *50*, 6506–6510.

Chapter 5

Development of functional polymer
resins for two-photon polymerization

5.1 Introduction

Synthetic materials have taken a more prominent role in the field of tissue engineering in recent years. They are more versatile than their natural counterparts and display improved stability.^[1,2] These materials generally serve in the form of scaffolds, which direct and promote cell growth towards a predetermined destination, depending on the application.^[3] Besides inorganic scaffolds,^[4] advanced functional scaffolds based on synthetic polymers receive a growing interest and are produced to mimic the extracellular matrix (ECM) as good as possible.^[5-7] To introduce ECM similarities often growth factors like arginylglycylaspartic acid (RGD) peptide sequences or ligands are incorporated.^[8] Furthermore the porosity and stiffness of the scaffold play an important role and topographic similarities to the ECM are required.^[9]

To have good control over the topography, two photon polymerization (2PP) has become a popular tool to achieve structures and 3D topographic features as small as 65 nm.^[10,11] It is based on the quasi-simultaneous (within 10^{-16} s) absorption of 2 photons by a photoinitiator to create radicals, which in their turn can initiate a radical polymerization reaction.^[12] As the energy for the incoming photons is cumulated upon absorption, the incoming laser light can be found in the near infrared (NIR) range. Several advantages are an improved penetration depth and a less destructive nature (*e.g.* biosamples).^[13,14] With the absorption of the first photon a virtual intermediate energy state is reached. After absorption of the second photon the excited state is reached, leading to the creation of radicals. The energy of the two photons is combined to trigger similar events as if it was one photon with double the energy.^[15] **Equation 1** provides this in a formula where E is the energy, h is the Planck constant and ν is the frequency.

$$E = h\nu_{UV} = \frac{1}{2}h\nu_{IR} + \frac{1}{2}h\nu_{IR} \quad (\text{Equation 1})$$

After excitation, two prominent types of relaxation can be considered, namely *via* inter-system crossing and *via* fluorescence, as depicted in the Jablonski diagram in **Figure 5.1**. Rapid non-radiative relaxation or inter-system crossing results in radical generation and subsequent initiation. This is in competition with the relaxation via fluorescence. Since radical generation and thus intersystem crossing is preferred, the fluorescence quantum yield has to be as low as possible for 2PP initiators.^[16]

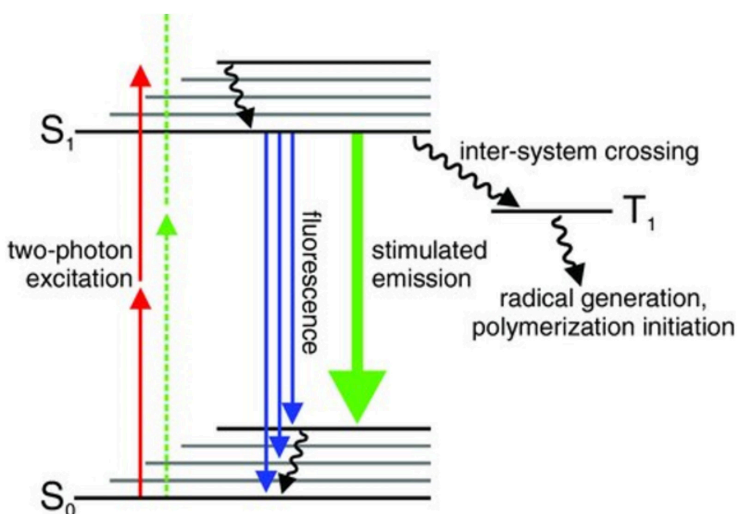


Figure 5.1. Jablonski diagram. Depicts relevant and optical transitions and processes for 2PP.

Since the lifetime of the virtual intermediate energy level is very short (10^{-4} - 10^{-9} s), an almost simultaneous absorption is required for 2PA. This is achieved by using an ultrashort (a femtosecond) pulsed laser instead of a high powered continuous wave laser. This results in a momentarily increased concentration of photons which subsequently increases the probability of a 2PA event. 2PA is furthermore proportional to the squared power of the photon flux density, *i.e.* intensity. This results in the creation of extremely local voxels and superior spatial

resolution beyond the diffraction limit, which allows for the direct 3D printing of detailed macrostructures.^[17] This is in contrast with the layer-by-layer approach of other computer aided design (CAD) techniques like stereolithography.^[18]

Recently, developments of customized 2PP resins tailoring specific applications have been reported.^[19,20] Commercial and custom-made resins comprise a cross-linking monomer and a 2PA photoinitiator. These monomers allow the formation of densely cross-linked polymeric networks and determine the structural and mechanical properties. Acrylic cross-linkers are often selected for their fast propagation.^[21] Radicals are generated upon excitation of a 2PA photoinitiator. The efficiency in non-linear photon absorption is given by the 2PA cross section (σ) and is measured in Göppert-Meyer (GM) units [$10^{-50} \text{ cm}^4 \text{ s photon}^{-1}$]. High σ values are related to charge transfer characteristics of the molecule. Therefore, mostly centrosymmetric molecules with electron-donating and electron-withdrawing moieties separated by a conjugated π -system are suitable for 2PA. Efficient 2PP photoinitiators have σ values of 100 GM or higher and low fluorescence quantum yields (as discussed earlier).^[12]

2PP is until date exclusively used for free radical polymerization processes. With the implementation of a reversible deactivation radical polymerization (RDRP) mechanism, the polymerization process is more controlled.^[22] This results in improved mechanical and chemical properties of the 3D printed structures. Furthermore, through high end-group fidelity the surface properties can be altered with the formation of block copolymers or conjugation reactions.^[23] One of the best-known RDRP reactions is reversible-addition fragmentation degenerative chain-transfer (RAFT) polymerization.^[24] The control mechanism of RAFT is based on a degenerative chain transfer. After initiation with a conventional radical initiator, a chain transfer agent (CTA) reversibly transfers and distributes the radicals over a large number of dormant polymer chains. This allows the polymer chains to grow at an equal pace. As the transfer rate is much higher than the termination rate a

“living” character of the polymerization is obtained. Concomitant high end-group fidelity and low polydispersity further fulfil the requirements for a successful RDRP.

To prepare a custom-made resin for photoRAFT (initiated upon photoexcitation) in 2PP, a so-called macroRAFT is added to a mixture of cross-linker and photoinitiator. A macroRAFT is a short RAFT polymer. With its addition to the resin, transfer agents are provided to the reaction mixture to allow a RAFT mechanism. Properties of the resin and the ultimate polymer structures can be tuned by varying the chemical nature of the macroRAFT. This can be achieved by selecting a proper end-group and a suitable monomer for the specific applications.

A typical functionality of transfer agents for RAFT polymerization are trithiocarbonates (TTCs). These are known to be polyvalent with respect to post-modification reactions.^[25] One of the most studied options is the conversion of TTCs into thiols through aminolysis. Subsequently these thiols can be addressed through reaction with activated vinyl compounds, better known as a thiol-ene Michael addition.^[26] Herein the formation of a thioether is catalyzed with the addition of a base or nucleophile.^[26,27] Carefully selecting the reaction conditions allows for a straightforward one-step aminolysis and Michael addition.^[28]

In here the development of a functional resin for 2PP, involving RAFT polymerization, is described (**Figure 5.2**). First, the synthesis of a poly(methyl methacrylate) (PMMA) macroRAFT is optimized. This macroRAFT is subsequently added to a custom-made resin comprising a methacrylic trifunctional cross-linker, and photoinitiator. 2PP laser parameters are optimized for this resin and the resulting structures were characterized and analyzed. Ultimately preliminary data was reported concerning post-modification of the cured resin through the conjugation of polyethylene glycol(PEG) acrylate (PEGA) using a thiol-ene Michael addition. A preliminary biocompatibility test was performed.

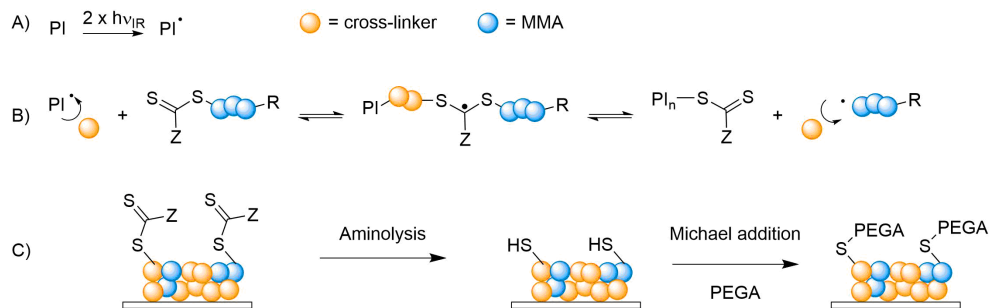
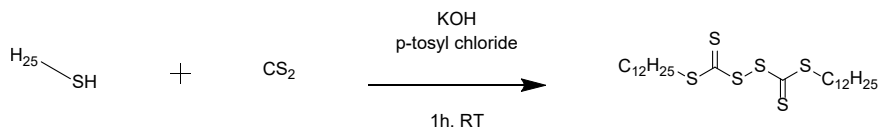


Figure 5.2. Schematic representation of photoRAFT in 2PP and subsequent post-modification. A) Photoinitiation through 2PA. B) RAFT equilibrium involving the PMMA macroRAFT. C) Aminolysis of TTC and subsequent Michael addition of PEG acrylate (PEGA).

5.2 Experimental Section

5.2.1 Synthesis of Bis(dodecylsulfanyl thiocarbonyl)disulfide

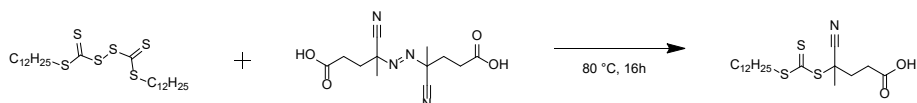


Scheme 5.1. Synthesis of Bis(dodecylsulfanyl thiocarbonyl)disulfide.

1-Dodecanthiol (10.12 g, 0.05 mol) was dissolved in a 1:4 aceton:H₂O mixture. KOH (3.366 g) was dissolved in 6.7 mL H₂O and subsequently added dropwise to the solution. CS₂ (3 mL, 0.05 mol) was added and the solution was stirred for 30 minutes at room temperature. After cooling on ice, p-toluenesulfonyl chloride (4.766 g, 0.025 mol) was added in small portions. The mixture was stirred for 1 hour at room temperature and another 10 minutes at 45 °C. The precipitate was filtered off and the product (bis(dodecylsulfanyl thiocarbonyl)disulfide) was

purified with flash column chromatography (85:15 hexane:DCM). Yield=72%

5.2.2 Synthesis of 4-cyano4-[(dodecylsulfanylthiocarbonyl)sulfanyl]pentanoic acid (CDP-TTC)



Scheme 5.2. Synthesis of CDP-TTC RAFT agent.

The final product was synthesized according to literature.^[29] (Bis(dodecylsulfanylthiocarbonyl)disulfide (9.3943 g, 0.016 mol) and 4,4'-azobis(4-cyanopentanoic acid) (7.115 g, 0.025 mol) were dissolved in ethyl acetate and refluxed overnight at 80 °C. Subsequently, additional 4,4'-azobis(4-cyanopentanoic acid) (2.371 g, 0.008 mol) was dissolved in ethyl acetate and added to the solution, which was stirred for another hour at 100 °C. The product was purified with gradient column chromatography (100 hexane to 34:66 ethyl acetate/hexane) yielding. 10.37 g. Yield=80% ¹H NMR (400 MHz, CDCl₃) δ 3.35 – 3.31 (m, 2H), 2.73 – 2.63 (m, 2H), 2.58 - 2.33 (m, 2H), 1.89 (s, 3H), 1.74 – 1.65 (m, 2H), 1.47 – 1.20 (m, 18H), 0.87 (t, 3H). (Figure A19).

5.2.3 Synthesis of PMMA macroRAFT

A solution of 8M MMA in dioxane and CDP-TTC agent was prepared targeting a theoretical 5000 g·mol⁻¹ (*DP* = 46) at 100% conversion. The reaction mixture was used without purging. A blue LED flow reactor as described by Rubens et al.^[30] was used. The reactor comprises a custom-made tubular reactor cascade, consisting of fluorinated gastight PFA tubing (Advanced Polymer Tubing GmbH, 1/16'' OD, 0.75 mm ID, reactor volume of 1.1 mL), wrapped around a glass framework and placed in a silicon oil bath heated to 90 °C on an IKA RCT basic hot plate (Figure A30).

Inside the glass framework 2 m of a blue light led strip (60 led/m, 450nm, 14.4 W) from Ledsky is placed facing the PFA tubing. Reaction solutions are pumped into the reactor via a HPLC pump (Azura). Monomer conversions were determined via ^1H NMR. Molecular weight distributions were analyzed via GPC-SEC. End-group fidelity was analyzed via ESI-MS.

5.2.4 Production of Microstructures using Two-Photon Polymerization (2PP)

Writing of 3D microstructures was performed with a 3D laser lithography system (Nanoscribe GmbH, Photonic Professional). The excitation source was a Ti-Sapphire femtosecond (fs) laser with a wavelength of 780 nm, emitting 150 fs pulses at 100 MHz and 50 mW at sample surface. The laser beam was focused using a 63 × microscope objective with a numerical aperture of 0.75. After exposure of the resin cates on a glass cover slide, the glass was cleaned using propylene glycol methyl ether acetate (PGMEA) for 10 minutes and isopropanol (IPA). The cover samples were dried using a gentle nitrogen flow (adapted from ^[15]).

Parameter tests are performed in piezo scan mode to optimize laser power and scan speed. Five lines with increasing height (from 0.5 μm to 2.5 μm ; length 10 μm) and spacing of 0.5 μm was seen as one unit. In the x-axis, 5 units were printed with increasing laser power (100% = 50mW). For each laser power, 5 units were printed in the y-axis, each with different scan speeds. In this way, 25 distinct laser power scan speed combinations could be screened in one print. The assays were visualized and characterized using a profilometer, SEM and energy dispersive x-ray spectroscopy (EDX). After defining the optimal laser parameters, cross arrays are printed. The composition of the 2PP resins was varied and optimized.

5.2.5 Cell Experiments

Human osteosarcoma MG-63 cells were cultured in alpha minimum essential medium (α -MEM) supplemented with 10% fetal bovine serum (FBS), 1% penicillin-streptomycin, 1% glutamine, 1% HEPES and 1% sodium pyruvate. The cells were cultured at 37 °C in a humidified atmosphere of 5% CO₂. Medium was replaced every 2 to 3 days. Cells were sub-cultured in standard culture flasks upon reaching 80-90% confluence, and then trypsinized with 0.25% trypsin/EDTA for 5 minutes at 37 °C. Trypsin was inactivated with three times its volume in medium, and used for experiments or sub-cultured (from^[11]).

5.2.6 Post-modification of the Polymers

Resin was casted on a glass substrate. Subsequently, the resin was cured using a UV excimer laser (351 nm, 1.5mJ, 100Hz, 15 seconds). The disc shaped, cross-linked polymer was placed in a glass petri dish. The polymer disc was rinsed with THF to remove any unreacted resin. A solution of hexylamine (1 eq.), PEGA (2 eq. ; 480 g·mol⁻¹) and THF was added in excess to the polymer disc. The petri dish was placed on a shaker for 2 hours. Thereafter, the mixture was removed and the disc was washed again with THF (2 times).

5.3 Results and Discussion

5.3.1 Synthesis of PMMA macroRAFT

Control over the molecular weight of the macroRAFT is essential as it has a direct influence on the amount of available functional end-groups in the resin and, depending on the resin composition, solubility of the polymer as additive. The applied polymerization procedure was based on a protocol described by Rubens *et al.*^[30] Direct photoexcitation of CDP-TTC used blue LEDs ($\lambda = 450$ nm) for initiation to improve end-group fidelity compared to initiation by UV light.^[31] The flow aspect makes the synthesis procedure easily upscalable and ensures a homogenous illumination of the reaction mixture (law Lambert-Beer). Using the TTC as the radical source eliminates initiator fragments as polymer end-groups and ensures the type of radical source. Wenn *et al.* showed that, when performing photoRAFT in flow, an undesired contribution to radical initiation from the RAFT agent can be expected. When removing the photoinitiator, still more than 60% monomer conversion was obtained through photoexcitation of the TTC.^[32] This problem is avoided by deliberately targeting the TTC for radical initiation.

To assess the controllability of the reaction, end-group fidelity, dispersities and the evolution of molecular weight with increasing conversion was investigated. In **Figure 5.3**. The number average molecular weight (M_n) and dispersity are plotted against conversion. A near-linear positive increase is observed, which confirms control over the molecular weight. Changing the solvent from DMSO to dioxane and without purging with N_2 , the conversion was reduced to 60% in 60 minutes compared to almost full conversion in literature.^[30] The polymerization was performed without the purging to mimic the oxygen rich environment at the 2PP set-up (nanoscribe). These results were used to determine the reaction procedure for the resin applied polymer. To produce the macroRAFT a relatively

low molecular weight was targeted with only a few monomer additions. Not only does a small macroRAFT provide more accessible CDP-TTC to the resin mixture, it also results in a more readily reinitiation of the RAFT polymerization, which makes the macroRAFT preferred for subsequent monomer additions compared to pure RAFT agent.^[30]

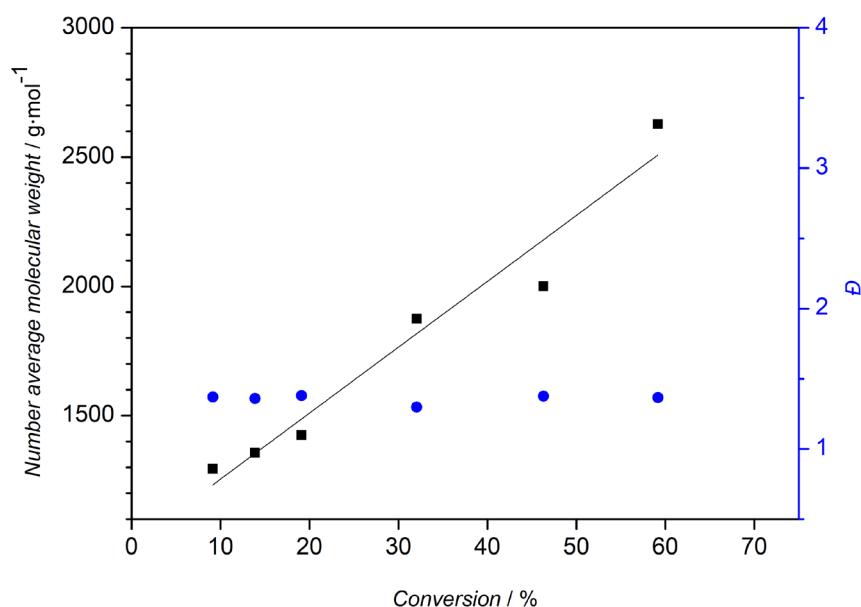


Figure 5.3. Blue light initiated photoRAFT polymerization of MMA. Number average molecular weight M_n and dispersity (D) plotted against conversion. $R^2 = 0.95$.

End-group fidelity was assessed via electrospray ionization mass spectrometry (ESI-MS) and revealed good end-group fidelity as the main distribution can be assigned to polymers consisting of MMA units and functional end-groups linked to the CDP-TTC RAFT agent, displayed in **Figure 5.4**. To check the stability of

the transfer agent under UV irradiation, polymerization was also performed in a UV flowreactor using a 365 nm fluorescent tube lamp. Although not directly comparable to the exposure of a two-photon laser, it might give indication of the survival odds in nanoscribe. This is an important feature to enable eventual post-modification reactions. ESI-MS revealed end-groups were maintained to a significant extent, although the detection of many side reactions indicate a loss of control, which is backed up by the M_n vs conversion plot where control appears to be lost after 20 minutes reaction time. This is accompanied by an increasing \mathcal{D} (Figure A20).

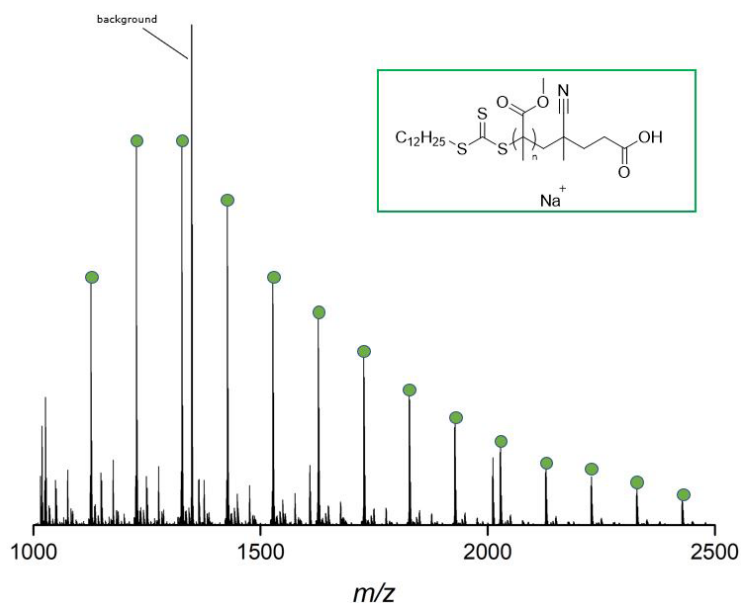


Figure 5.4. ESI-MS spectrum displaying a distribution of PMMA with intact CDP-TTC incorporated.

5.3.2 Optimization of resin composition and two-photon polymerization

To optimize the laser parameters, the photoinitiator Irgacure 819 mixed with cross-linker trimethylolpropane trimethacrylate (TRIM), depicted in **Figure 5.5** was used as resin. Generally, photoinitiators used in resins are produced via elaborate and tedious synthesis procedures (hence the high cost) and require specific properties as described in the introduction.

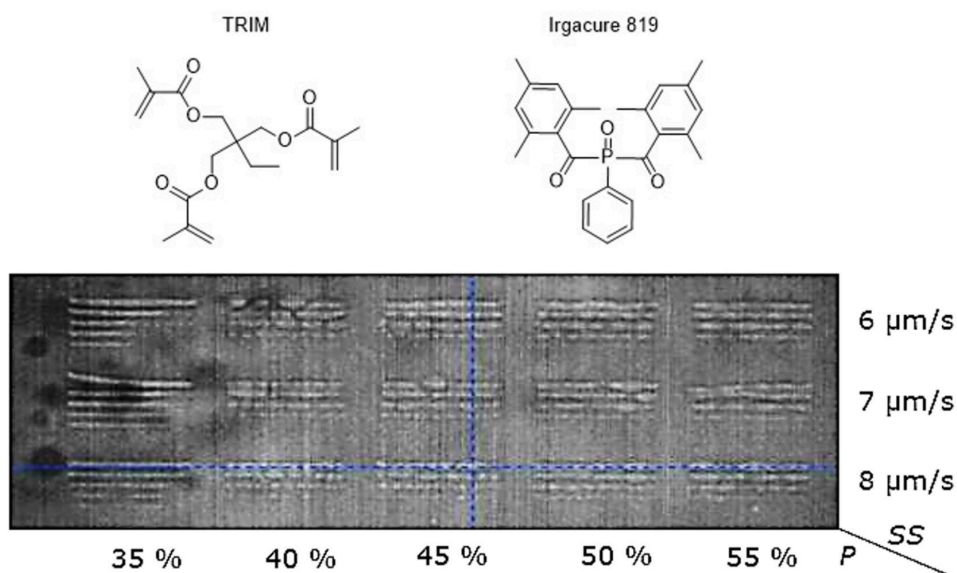


Figure 5.5. The cross-linker (upper left) and photo-initiator (upper right) were used to optimize 2PP parameters. A live microscopy image (bottom) shows the optimization array with varying power (P , 100% = 50 mW) and scan speed (SS).

The compatibility of Irgacure 819 with 2PP was described by Schafer *et al.*^[33] Irgacure 819 was found to be suitable, but exhibited a relatively small absorption cross-section. Being commercially available and relatively cheap it was considered

a worthy candidate. With the formation of radicals by an additional initiator, in 2PP, the macroRAFT is incorporated through a classical RAFT process, with the trithiocarbonate only serving as the transfer agent (in contrast to the synthesis of the macroRAFT). This furthermore supports the decision of using a methacrylic cross-linker, respecting the compatibility of the CDP-RAFT agent.

As displayed in **Figure 5.5**, the resolved lines could be drawn using a concentration of 5 mol% Irgacure 819 in TRIM, which serves as cross-linker and as solvent. The array with the lowest power, at 35%, gave the best results. Higher powers appeared to have discontinuities. Lower laser power however seemed to reduce the risk of overheating the voxels. Prolonged exposure, which is related to the scan speed, to higher laser power could increase the risk of “micro explosions”. Such explosions destroy the printed structure. Therefore a 7 $\mu\text{m/s}$ scan speed and a laser power set at 35% was selected for further experimentation. The printed lines were subsequently characterized using a profilometer, as depicted in **Figure 5.6**. From bottom to top, for each condition (power and scan speed), different structure heights were targeted, starting with 0.5 μm up to 2.5 μm increasing with steps of 0.5 μm . Up to 2 μm height polymer lines were printed with good resolution and a desired height difference of approximately 0.5 μm difference in height.

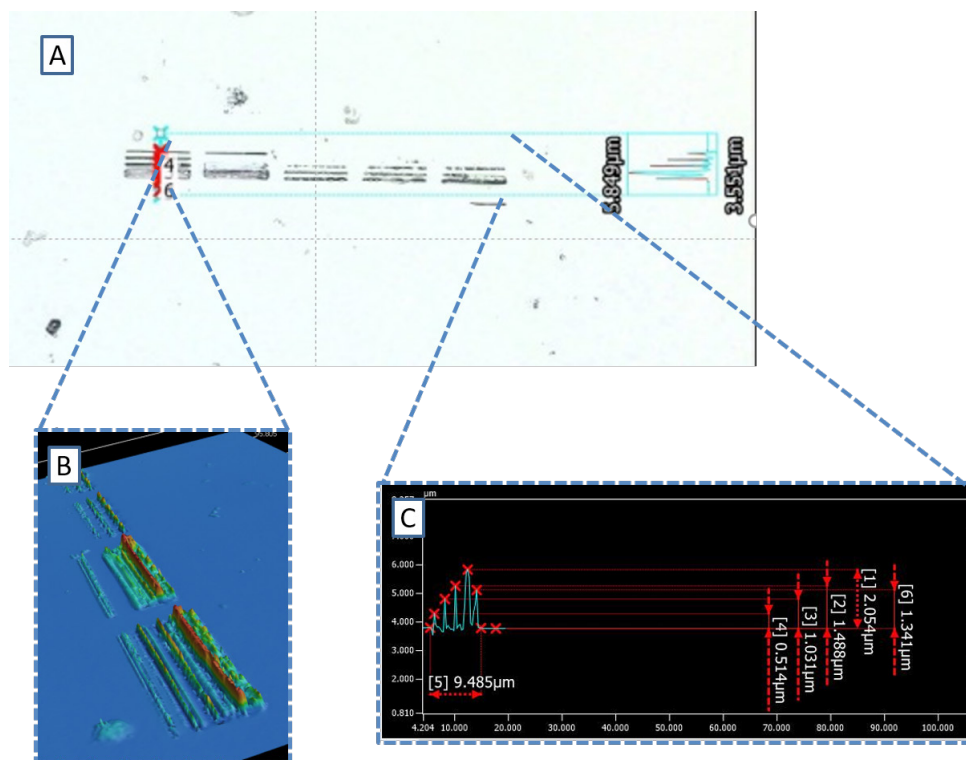


Figure 5.6. Profilometer analysis of the parameter array test on resin comprising 5 mol% Irgacure 819 dissolved in TRIM as cross-linker. Selected parameters were scan speed 7 $\mu\text{m/s}$ and laser power 35% (100% 50 mW). Depicted are A) brightfield image of array. B) 3D profile map of the array. C) Profile of the array.

For the final step before 2PP, the PMMA macroRAFT was mixed into the tested resin. The reaction time for the synthesis of this macroRAFT was set at 20 minutes to obtain a molecular weight of around 1500 $\text{g}\cdot\text{mol}^{-1}$ (exp = 1570 $\text{g}\cdot\text{mol}^{-1}$ $D = 1.29$). DMSO (45 volume%), chosen because of its low volatility, was added to resin to increase the polymer content from 2 to 10 mol% and thus the amount of available end-groups for post-modification. Mol% were calculated without solvent, therefore only giving the respective amounts of cross-linker, initiator and

macroRAFT. The addition of solvent can lead to more porous structures, which can affect the interaction with cells. It is therefore a reckonable parameter when progressing towards cell studies. Structures in the shape of crosses were printed. SEM imaging, displayed in **Figure 5.7**, revealed a nicely defined, x-shaped polymer structure.

Elemental analysis via electron dispersive x-ray spectroscopy (EDX) confirmed the carbon and oxygen contribution (although the glass substrate in the background overtakes the oxygen contribution stemming from the polymer structure). The slight increase in phosphorus can be assigned to Irgacure 819. Most importantly a slightly higher sulfur contribution was observed at the position of the "x", which can be assigned to the presence of the trithiocarbonate incorporated in the PMMA macroRAFTs. A resin with only 2 mol% PMMA did yield similar results (Figure A21). However, no sulfur was detected. This indicates a higher macroRAFT concentration is necessary. The absence of sulfur can indicate that EDX might not be sensitive enough to detect the 2 mol% of PMMA or the TTCs get at least partially destroyed in the 2PP process. Further investigation using more sensitive (ToF-SIMS) and quantitative (XPS) techniques is recommended.

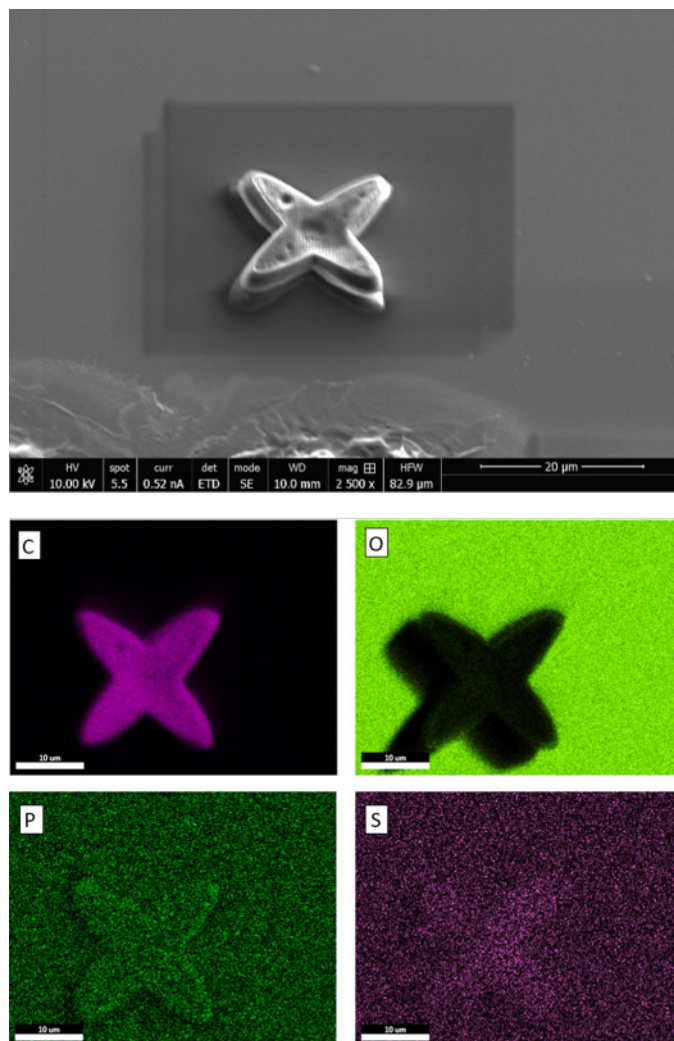


Figure 5.7. SEM image of "x" shaped polymer structure (top). EDX mapping reveals the elemental contribution of carbon (C), oxygen (O), phosphorus (P) and sulfur (S). The resin comprised 5 mol% irgacure 819, 10 mol% PMMA, TRIM and DMSO (45 vol%).

5.3.3 Biocompatibility assays

Before using these synthetic scaffolds in bio-applications, tests to determine toxicity and biocompatibility are required. A preliminary test was carried out using a resin comprising TRIM and Irgacure 819, without PMMA macroRAFT. In a first instance, toxicity for these two components was investigated to set a reference point. A cross array was printed and cultured with osteosarcoma cells. The cells were observed in proximity and in between the polymer crosses, surviving for up to three days as displayed in **Figure 5.8**. Due to the insufficient seeding of the cells, these tests have to be repeated, including a live staining (Calcein AM, green, and EtD-1, red) to assess viability and staining with DAPI(blue) and phalloidin(red) to visualize the nuclei and cytoskeleton respectively, which play an essential role in cell proliferation and migration.

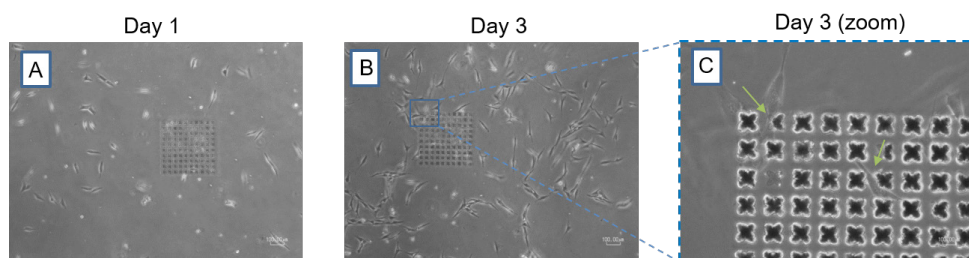


Figure 5.8. Optical microscopy image taken from cross array subjected to a osteosarcoma culture. A) picture after one day. B) After the three days viable cells can be found on and between the crosses. Zoom from 10x to 20x (C).

5.3.4 Post-modification

As preliminary post-modification test the resin containing 10 mol% PMMA was casted on a glass substrate and cured using the UV (351 nm) excimer laser to obtain a disc-shaped polymer structure. To assess the possibility for modification,

Polyethylene glycol (PEG) acrylate ($480 \text{ g}\cdot\text{mol}^{-1}$) was conjugated to the polymer disc using a thiol-ene Michael addition. PEG chains are generally known for their stealth effect in bio-applications and inertness.^[34] In this case it also alters the hydrophilicity of the surface. With the addition of hexylamine (in excess) the available trithiocarbonates were transformed to thiols via aminolysis. Subsequently, the activated vinyl functionality present in the acrylic moiety was further modified in situ to form a thioether bond. When characterizing the polymer disc with ATR-IR, a new peak around 1100 cm^{-1} is observed, as displayed in **Figure 5.9**. Pure PEG-acrylate displays a prominent peak at the same position, which can be assigned to the C-O-C stretch vibration. This result is considered promising. However, more experiments are required to exclude any possible physisorption. The next step is to repeat this experiment for structures constructed with 2PP with the addition of characterization techniques like ToF-SIMS and XPS for further confirmation.

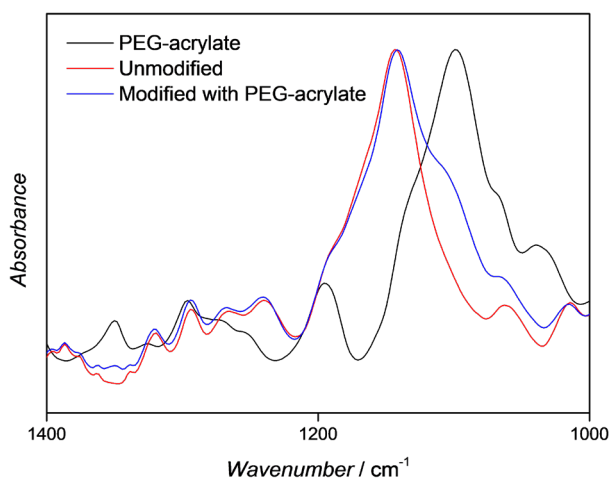


Figure 5.9. ATR-IR spectrum of cured polymer resin using a UV (351 nm) excimer laser compared to pure acrylate (represented by the C-O-C stretch vibration at 1100 cm^{-1}) and the spectrum after the modification of the polymer resin with PEGA via Michael addition.

5.4 Conclusions

The incorporation of functional polymers into polymer resins receives a growing interest in the field of tissue engineering and the synthesis of complex structures. In combination with 2PP, highly resolved structures in the micro scale can be produced and post-modified to meet demanding requirements. The synthesis of a PMMA macroRAFT was assessed in flow and the procedure was adapted for the production of low molecular weight polymers. The parameters for 2PP were optimized for resins consisting of Irgacure 819 (5 mol%) as photoinitiator and TRIM as cross-linker. When adding the macroRAFT as additive, cross arrays were successfully produced. The addition of solvent (DMSO) was required to push the molar contribution of PMMA to 10 mol%, which was necessary to detect sulfur in EDX, stemming from the TTC functionality required for post-modification. Preliminary tests modifying the resin with PEGA using Michael addition reactions gave promising results. Preliminary cell studies showed viable cells in proximity of the cross arrays for up to three days. More and detailed investigations are however required to draw any definite conclusions on biocompatibility.

5.5 Future outlook

The preliminary results obtained in this research demonstrate the possibilities of this approach and opens pathways for future investigation and applications. The chosen polymerization strategy (RAFT) allows for the addition of a vast library of different monomer types due to its versatile nature. This results in polymers that can be made more hydrophilic, are more or less rigid, contain interesting lower critical solution temperatures (LCST) or exhibit thermo- or pH-responsive behavior. Instead of using conventional CTA's multifunctional RAFT agent could be used which results in multiplying the available functional groups for post-modification. Functional groups are furthermore not limited to thiol groups, as presented in this chapter, but also the function of the R-group (in this case an carboxyl group) can be transformed and the synthesis of block copolymers or chain extension can be explored. To eventually serve a biological purpose the structures have to be elaborately investigated in a cellular environment to determine their biocompatibility and toxicity. Lastly, degradation studies will determine the fate of the materials and toxicity of these fragments has to be considered. All these options and possible features can be explored towards a gigantic amount of possible applications.

5.6 References

- [1] J. Patterson, M. M. Martino, J. A. Hubbell, *Mater. Today* **2010**, *13*, 14–22.
- [2] J. L. Drury, D. J. Mooney, *Biomaterials* **2003**, *24*, 4337–4351.
- [3] J. Torgersen, X.-H. Qin, Z. Li, A. Ovsianikov, R. Liska, J. Stampfl, *Adv. Funct. Mater.* **2013**, *23*, 4542–4554.
- [4] J. Yang, J. L. Guo, A. G. Mikos, C. He, G. Cheng, *Ann. Biomed. Eng.* **2018**, *46*, 1229–1240.
- [5] T. Limongi, A. Rocchi, F. Cesca, H. Tan, E. Miele, A. Giugni, M. Orlando, M. Perrone Donnorso, G. Perozziello, F. Benfenati, et al., *Mol. Neurobiol.* **2018**, 1–11.
- [6] A. Rahmani Del Bakhshayesh, N. Annabi, R. Khalilov, A. Akbarzadeh, M. Samiei, E. Alizadeh, M. Alizadeh-Ghodsi, S. Davaran, A. Montaseri, *Artif. Cells, Nanomedicine, Biotechnol.* **2018**, *46*, 691–705.
- [7] F. P. W. Melchels, M. A. N. Domingos, T. J. Klein, J. Malda, P. J. Bartolo, D. W. Hutmacher, *Prog. Polym. Sci.* **2012**, *37*, 1079–1104.
- [8] A. Ovsianikov, A. Deiwick, S. Van Vlierberghe, M. Pflaum, M. Wilhelmi, P. Dubruel, B. Chichkov, A. Ovsianikov, A. Deiwick, S. Van Vlierberghe, et al., *Materials (Basel)*. **2011**, *4*, 288–299.
- [9] D. W. Hutmacher, *Biomater. Silver Jubil. Compend.* **2000**, 175–189.
- [10] W. Haske, V. W. Chen, J. M. Hales, W. Dong, S. Barlow, S. R. Marder, J. W. Perry, *Opt. Express* **2007**, *15*, 3426.
- [11] D. Barata, P. Dias, P. Wieringa, C. van Blitterswijk, P. Habibovic, *Biofabrication* **2017**, *9*, 035004.

- [12] J. Torgersen, in *Photocured Mater.*, **2014**, pp. 75–86.
- [13] A. Vogel, V. Venugopalan, **2003**, DOI 10.1021/CR010379N.
- [14] T. Weiss, G. Hildebrand, R. Schade, K. Liefeth, *Eng. Life Sci.* **2009**, *9*, 384–390.
- [15] A. Ovsianikov, B. N. Chichkov, *Methods Mol. Biol.* **2012**, *868*, 311–25.
- [16] J. Fischer, G. von Freymann, M. Wegener, *Adv. Mater.* **2010**, *22*, 3578–3582.
- [17] M. Malinauskas, M. Farsari, A. Piskarskas, S. Juodkazis, *Phys. Rep.* **2013**, *533*, 1–31.
- [18] S. A. Skoog, P. L. Goering, R. J. Narayan, *J. Mater. Sci. Mater. Med.* **2014**, *25*, 845–856.
- [19] M. Tromayer, P. Gruber, M. Markovic, A. Rosspeintner, E. Vauthey, H. Redl, A. Ovsianikov, R. Liska, *Polym. Chem.* **2017**, *8*, 451–460.
- [20] A. Ovsianikov, J. Viertel, B. Chichkov, M. Oubaha, B. MacCraith, I. Sakellari, A. Giakoumaki, D. Gray, M. Vamvakaki, M. Farsari, et al., *ACS Nano* **2008**, *2*, 2257–2262.
- [21] L. H. Nguyen, M. Straub, M. Gu, *Adv. Funct. Mater.* **2005**, *15*, 209–216.
- [22] X. Pan, M. A. Tasdelen, J. Laun, T. Junkers, Y. Yagci, K. Matyjaszewski, *Prog. Polym. Sci.* **2016**, *62*, 73–125.
- [23] M. R. Hill, R. N. Carmean, B. S. Sumerlin, *Macromolecules* **2015**, *48*, 5459–5469.

- [24] J. Chiefari, Y. K. Chong, F. Ercole, J. Krstina, J. Jeffery, T. P. T. Le, R. T. A. Mayadunne, G. F. Meijs, C. L. Moad, G. Moad, et al., *Macromolecules* **1998**, *31*, 5559–5562.
- [25] G. Moad, E. Rizzardo, S. H. Thang, *Polym. Int.* **2011**, *60*, 9–25.
- [26] J. W. Chan, H. Wei, H. Zhou, C. E. Hoyle, *Eur. Polym. J.* **2009**, *45*, 2717–2725.
- [27] G.-Z. Li, R. K. Randev, A. H. Soeriyadi, G. Rees, C. Boyer, Z. Tong, T. P. Davis, C. R. Becer, D. M. Haddleton, *Polym. Chem.* **2010**, *1*, 1196.
- [28] J. Vandenberg, K. Ranieri, T. Junkers, *Macromol. Chem. Phys.* **2012**, *213*, 2611–2617.
- [29] H. U. Kang, Y. C. Yu, S. J. Shin, J. H. Youk, *J. Polym. Sci. Part A Polym. Chem.* **2013**, *51*, 774–779.
- [30] M. Rubens, P. Latsrisaeng, T. Junkers, D. Chen, L. Wang, C. Zhao, *Polym. Chem.* **2017**, *215*, 9–26.
- [31] T. G. McKenzie, Q. Fu, E. H. H. Wong, D. E. Dunstan, G. G. Qiao, *Macromolecules* **2015**, *48*, 3864–3872.
- [32] B. Wenn, T. Junkers, *Macromolecules* **2016**, *49*, 6888–6895.
- [33] K. J. Schafer, J. M. Hales, M. Balu, K. D. Belfield, E. W. Van Stryland, D. J. Hagan, *J. Photochem. Photobiol. A Chem.* **2004**, *162*, 497–502.
- [34] H. K. Makadia, S. J. Siegel, H. K. Makadia, S. J. Siegel, *Polymers (Basel)*. **2011**, *3*, 1377–1397.

Chapter 6

Synthesis of functional polymer particles from Morita-Baylis-Hillman polymerization

G. Ramakers, Claudio D'Incal, Mick Gagliardi, Daniël G. M. Molin, Tanja Junkers, *Macromol. Rapid Commun.* **2018**, 1800678

6.1 Abstract

Functional synthetic polymers are frequently explored for their use in the biomedical field. To fulfill the stringent demands of biodegradability and compatibility, the materials need to be versatile and tunable. Post-modification is often considered challenging for well-known degradable materials like poly(lactic acid) because of their chemical inertness. In this work a procedure is proposed to produce densely functionalized polymer particles using oligomeric precursors synthesized via the Morita-Baylis-Hillman reaction. This allows for a variety of post-modification reactions to serve bio-conjugation or tuning of the material properties. The particles are subjected to basic media and found to be degradable. Furthermore, cytotoxicity tests confirm good biocompatibility. Finally, as a proof of concept to demonstrate the versatility of the particles, post-modification reactions are carried out through the formation of imines.

6.2 Introduction

The development of functional biodegradable materials for biomedical use is an ongoing endeavor in polymer chemistry. While a broad range of polymerizations has been applied for this purpose, there is until today a need for novel tunable materials.^[1-4] For medical use, a biomaterial should ideally be non-toxic, have favorable thermal and mechanical properties, be able to hold a payload (when used for drug delivery purposes), (bio)degrade under controlled conditions to non-harmful fragments and be chemically versatile.^[5-7] Many of these conditions are met by well-known materials such as poly(lactic acid) or related polymers. Yet, while usually relatively easy to obtain, they mostly suffer from chemical inertness, and hence are difficult to manipulate chemically. This poses a significant hurdle for ligation of biomolecules or the formation of core-shell structures.^[8,9]

Most biodegradable materials possess ester bonds that hydrolyze under certain pH conditions.^[10] Depending on the hydrophilicity or hydrophobicity of the materials, such degradation can occur quickly or slowly under physiological conditions. Polyesters are mostly synthesized from step-growth esterification, or by ring-opening polymerization of cyclic esters. Some exceptions exist such as the radical ring-opening polymerization of cyclic ketene acetals.^[11] In our previous work, we had shown that thiol-ene polymerization can be a versatile and simple method to obtain a broad variety of ester-degradable polymers, when diacrylates are reacted with dithiols using base catalysis.^[12-15] In such case, the degradable ester is already present in the monomer, while the thioether linkage that is formed during polymerization remains non-degradable. Thiol-ene polymerizations are fast and efficient, and due to the commercial availability of both dithiols and diacrylates, functional materials with tunable hydrophobicity can be accessed with ease.^[16,17] A series of materials was in this way synthesized, allowing to even change the mode of degradation (bulk degradation vs surface degradation).^[14] Further adaptability

could be reached by using reversible addition fragmentation degenerative chain transfer (RAFT) polymerization to obtain oligomeric dithiols, then allowing to make thiol-ene polymers with a broad range of thermal and mechanical properties.^[12,18] A distinct disadvantage of the approach is though that thiols are typically associated with strong odors, and inherent reactivity. Monomers form disulfides, while the polymers oxidize to sulfoxides, changing then the mechanical properties of the polymers. As an alternative to thiol-ene polymerization we thus explore in here the use of the Morita-Baylis-Hillman (MBH) reaction. In MBH reactions, dialdehydes react with diacrylates, forming likewise a polyester. The use of thiols is hence avoided, while at the same time vinyl groups are introduced into the backbone of the polymer. This allows in principle for facile chemical functionalization after polymerization. The MBH reaction is shown in **Figure 6.1**. Mechanistically similar to base-catalyzed thiol-ene reactions, the acrylate moieties are activated by tertiary amines, followed by addition of the aldehyde.^[19] After elimination of the amine from the product, the geminal double bond is obtained.

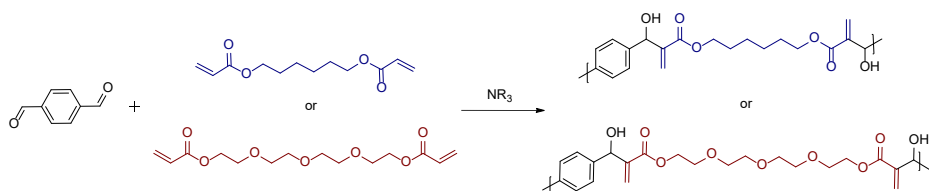


Figure 6.1. Morita-Baylis-Hillman polymerization to create hydrophobic (top, blue) or hydrophilic (bottom, red) polymers.

MBH polymerizations have been described before by Klok and coworkers,^[20–22] and a number of tertiary amines have been identified in the past to catalyze the reactions efficiently. Yet, obtainable molecular weights remain limited and the oligomers synthesized are of only limited practical use from a mechanical point of view. In the present contribution we have adapted the previous procedures to

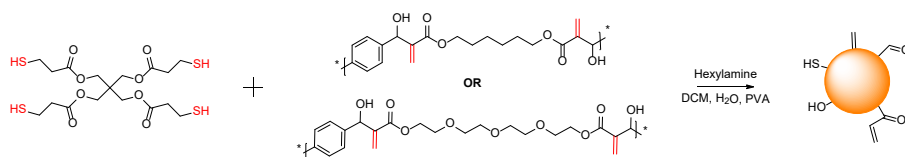
create hydrophobic and hydrophilic MBH polymers. These polymers are powerful precursors to form more complex materials, and the geminal double bond found in the polymers are an excellent tool for modification. In combination with thiol-ene cross-linking, MBH materials can be formulated efficiently to obtain suspension particles. If tuned well, these particles will feature aldehyde groups on their surface that are readily available for functionalization by imine formation, a reaction often employed in bioconjugation.^[23-26] Further, the biocompatibility of these particles is discussed.

6.3 Experimental section

6.3.1 Morita-Baylis-Hillman polymerization (MBH polymerization)

To synthesize the MBH oligomers 2g (1 eq.) of TA, acrylate (1 eq.), catalyst (DABCO, 3-HQD or DMAP, 1 eq;), and methanol (1.63 eq.) were dissolved in 5 mL of dimethyl- formamide. The mixture was stirred for 24 hours at room temperature. The obtained product was precipitated in cold diethyl ether and purified over a silica plug to remove the catalyst. The collected oligomers were analysed with SEC-GPC, ESI-MS and ¹H-NMR, respectively.

6.3.2 Suspension Polymerization



Scheme 6.1. Schematic representation of suspension polymerization via thiol-ene Michael addition yielding densely functionalized micro particles.

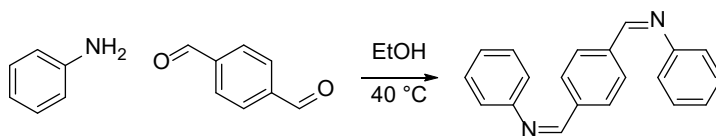
The polymer particles were synthesized via a suspension polymerization. The continuous phase contained distilled water and a PVA concentration of $10 \text{ mg}\cdot\text{mL}^{-1}$ while the organic phase contained the MBH oligomers (1 eq of repeating units), PETMP (0.5 eq. per repeating unit) and dichloromethane (DCM) (3 mL per gram MBH oligomers). Subsequently, the organic phase was added to the continuous phase and placed on a stirring plate. After letting the suspension stir for 3 minutes a few droplets of hexylamine were added. The mixture was left to react for 30 minutes while stirring continuously (1200 rpm).

6.3.3 Polymer degradation study

To test degradability, the MBH oligomers (100 mg) were added to a NaOH solution of 1M in water. The mixture was stirred (800 RPM) for 6 days at $40 \text{ }^\circ\text{C}$ and, subsequently, extracted with DCM. The DCM was evaporated and the degradation products were characterized by SEC-GPC.

The same procedure was followed for analyzing the degradation of the polymer particles. The degraded material was washed with H_2O twice by centrifugation (5 minutes, 4 000 rpm). The pellet was analysed using optical microscopy

6.3.4 Schiff base modification on particle surfaces



Scheme 6.2. Synthesis of Schiff base from TA and aniline.

A reference for infrared characterization a Schiff base was synthesized by dissolving 0.7 mL of aniline (2 eq.) in 1 mL of absolute ethanol. Subsequently, this solution

was gradually added to a solution of TA (0.5 g, 1 eq.) in 1 mL of absolute ethanol and stirred for 2 hours at 40 °C. Finally, the product was three times recrystallized from ethanol ($\text{conv}_{\text{nmr}} = 66\%$).

For the particle functionalization, 0.5 mL of aniline was dissolved in 1 mL absolute ethanol. This solution was slowly added to 0.04 g of MBH particles dispersed in absolute ethanol (1 mL). Subsequently, this mixture was stirred for 4 hours at 40 °C and was followed by centrifugation of the synthesized particles with 50 mL of H₂O twice, and one time with acetone. Ultimately, the particles were dried in a vacuum oven (40 °C, ± 4 hours) and analysed using ATR-IR.

6.3.5 Cytotoxicity study

To test the toxicity of the material the polymer particles were incubated with cell culture medium at a concentration of 100 mg/mL for 24, 48, 72, 98h and 1 week. Control was medium incubated without particles for 1 week. After incubations, supernatants were collected after a short centrifugation step. The supernatants were added to a 96 well plate with HUVECs (Human umbilical vein endothelial cells) and a 96 well plate with porcine skin fibroblasts in the following concentrations: 0.1 mg/mL, 1 mg/mL, 10 mg/mL and 50 mg/mL and incubated for 24 hours. After 24 hours cytotoxicity was determined.

6.4 Results and discussion

6.4.1 Morita-Baylis-Hillman polymerization

As a first step, precursor MBH oligomers were synthesized. Two different acrylic linkers were selected to be combined with terephthalaldehyde (TA), namely hexanediol diacrylate (HDDA) and tetraethyleneglycol diacrylate (TEGDA), with the last monomer creating polar resins. For both linkers a quick optimization assay was carried out, as literature suggested different catalyst preferences depending on the type of acrylate used.^[27] Size exclusion chromatography (SEC) elugrams (displayed in **Figure 6.2**) shows for both types of polymer a pattern which is typical for a step-growth polymerization. The difference and relative effectiveness of the catalyst/acrylate combination is illustrated by an overlay of the molecular weight distribution (MWD) for each monomer combination. TA with HDDA seems to yield the best results when 3-hydroquinolidone (3-HQD) is employed as the catalyst, as indicated by lower overall elution volumes and hence higher molecular weight when compared to other catalysts. Using the Mark-Houwink parameters for polystyrene in tetrahydrofuran (THF) an apparent number average molecular weight (M_n) of around 1 400 g·mol⁻¹ is obtained, which is in line with literature^[22] and suggests an oligomer of 3-4 repeating units consisting of one HDDA and one TA moiety, respectively. For the polymer built from TEGDA and TA an M_n around 850 g·mol⁻¹ was obtained, which would correspond to an oligomer of less than 2 full repeating units on average. TEGDA seems to give the best results while using 1,4-diazabicyclo[2.2.2]octane (DABCO).

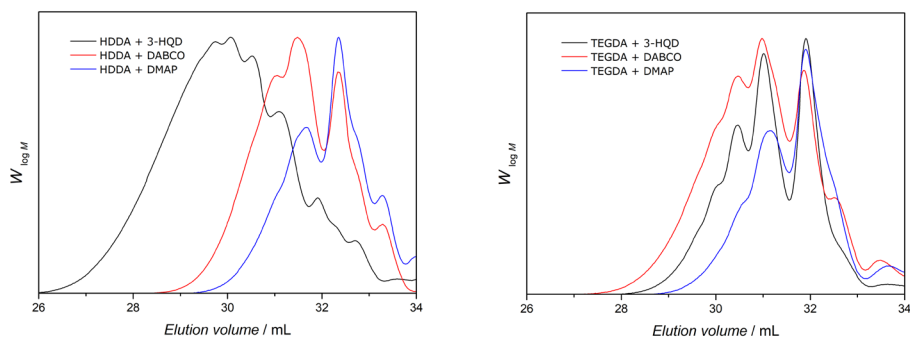


Figure 6.2. Elugrams obtained via SEC assessing the efficiency of different tertiary amines as catalyst for MBH polymerization of TA in combination with HDDA (left) and TEGDA (right).

Since catalysts like 3-HQD and DABCO are suspected to be cytotoxic they need to be used with extra care^[28,29] and therefore an additional purification step is preferred prior to further use. The obtained MBH polymers were hence passed over a silica plug and analyzed with proton-nuclear magnetic resonance (¹H NMR). NMR of the unpurified polymeric materials showed that the extra purification step was essential to remove the residual catalyst (see Figure A22 and A23 for details). Additionally, electrospray ionization-mass spectrometry (ESI-MS) was performed to confirm the molecular structure of the oligomers. ESI-MS displayed the expected oligomer structures, yet also revealed that some chains carry the catalyst as end-group, despite NMR not indicating the presence of such groups (Figure A24). Furthermore, peaks could be assigned to species stemming from reaction with impurities, namely 6-hydroxy hexyl acrylate (in case of HDDA), which may be present as impurity in the commercially available monomer. Also for the ESI-MS spectrum of the MBH polymers containing TEGDA fragments, depicted in Figure A25, the corresponding impurity was discovered. After purification, no distribution could be assigned to DABCO containing polymer chains anymore.

6.4.2 Suspension polymerization and polymer degradation

The purified MBH oligomers were subsequently used for particle synthesis. The activated vinyl groups, which are typically part of a MBH adduct, can be used for cross-linking via Michael addition (along with the available acrylate groups stemming from the acrylic linkers at the chain end). MBH particles are produced by suspending the MBH oligomers with a multifunctional thiol cross-linkers in water. A small tetrafunctional cross-linker, pentaerythriol tetrakis(3-mercaptopropionate) (PETMP), was selected to ensure dense cross-linking of the MBH precursor. In principle, thiol-ene reactions can be performed via radical pathways, and – since the pendant double bonds along the backbone are activated – via base catalyzed Michael addition. In here, we opted to use the Michael addition route, and hexylamine was used as catalyst. For visualization of the success of the reactions, particles were analyzed with optical microscopy after suspension polymerization. The particle size was determined by using a mastersizer, to a mean diameter of 232 μm (span = 0.95) for HDDA containing MBH polymers and 204 μm mean (span = 0.85) particle size for the TEGDA containing MBH polymers (Figure A26). The corresponding microscopy images are displayed in **Figure 6.3** and Figure A27 for the particles with HDDA and TEGDA containing particles, respectively. Particle formations were shown to be well reproducible. To tune particle size and to obtain slightly smaller particles (more suitable for the cytotoxicity studies) simply a bigger stirring bar was used, yielding then particles of around 157 μm mean (span = 0.67). The microscopy images show the size distribution of the polymer particles is rather broad, yet within expectations for a suspension polymerization. This is confirmed by the mastersizer. Since thiol groups are present on the particle surfaces, in principle disulfide formation can cause particle aggregation. Monitoring the size of particles over the time frame of two weeks did, however not show any significant change in size, at least when particles were stored in dry state.

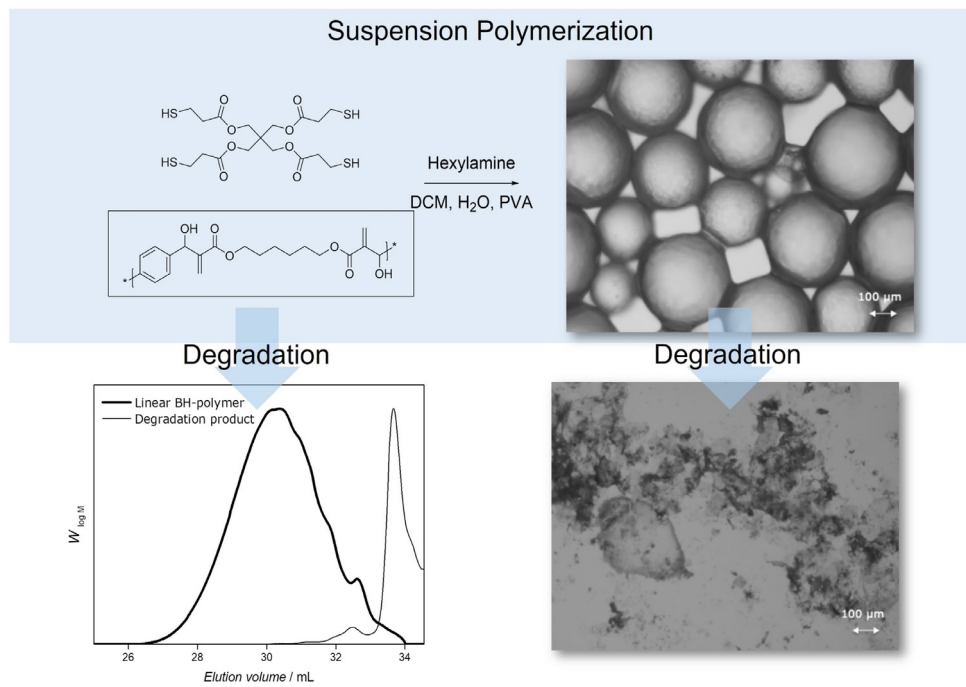


Figure 6.3. After the formation of polymer particles through the crosslinking of MBH oligomers both the linear molecules and the particles were successfully degraded as confirmed by SEC (lower left) and optical microscopy (lower right) respectively.

The advantage of MBH polymer based particles with respect to post-modification is the variety of accessible functional groups to choose from. After using the vinyl groups for cross-linking and particle synthesis, the aldehyde functionality was targeted as a proof of principle for the synthesis of a Schiff base with the addition of aniline. Aniline served hereby as model compound, yet any amine will be available to form imines on the surface of the particles. Attenuated total reflectance infrared spectroscopy was the technique of choice to confirm imine formation on the particle surface, and indeed the imine specific vibration bands can be observed hence imine specific vibration bands can be observed. A successful

reaction was indicated by the presence of vibration bands near 1 630, 1 610 and 1 500 cm^{-1} , corresponding to a successful imine formation.^[30] The IR spectrum is shown in **Figure 6.4**. Biofunctionalization of the particles is hence achievable in simple procedures that are well known in the realm of biochemistry. Since the MBH resin can be changed from polar to apolar by the choice of diacrylate used (and also by the choice of thiol cross-linker), also mechanical properties can in principle be tuned with relative ease, giving rise to a very high tenability of the particles.

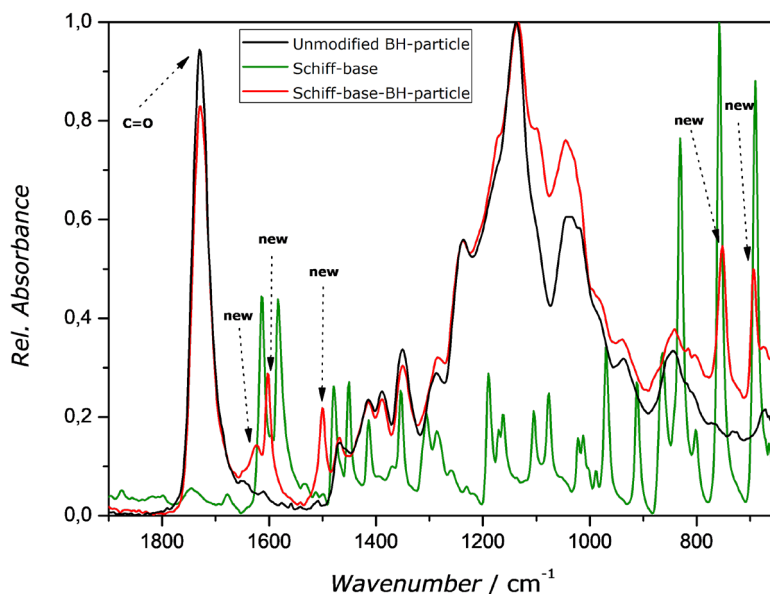


Figure 6.4. FTIR spectrum comparing MBH particles before and after modification with aniline through the formation of a Schiff base.

Both the linear MBH oligomers and the polymer particles were subjected to a degradation study. The polymer hydrolyses when exposed to basic condition ($\text{pH} =$

14) via its ester moieties. SEC revealed the evolution from the typical step-growth polymer pattern to an almost complete degradation of the oligomers. This was the case for both types of polymer, however especially for MBH polymers with TEGDA linkers, a fraction of higher molecular weight polymers could still be observed as shown in Figure A28. Degradation of the polymer particles was visualized with optical microscopy. Subjection to the basic solution turned the particles into an amorphous residue indicating a successful degradation. Microscopy images of the residues are displayed in **Figure 6.3** and A28. Of course, degradation in basic media does not allow for the direct conclusion that the materials are biodegradable, yet – especially for polar particles – a positive outcome may be expected.^[31,32] Assessment of the exact mode of degradation (surface degradation vs bulk degradation) and the range of conditions under which degradation occurs are subject to further investigation. Based on the experience gained on thiol-ene networks, it can be, however, concluded that degradation will also occur under acidic conditions.^[15]

6.4.3 Cytotoxicity tests

A cytotoxicity test was performed to gain information about the biocompatibility of the particles in order to evaluate for their usefulness in biomedical application. The results are depicted in **Figure 6.5**. The chosen cell lines, namely porcine skin fibroblasts (PSF) and human umbilical vein endothelial cells (HUVEC), are selected for their structural role in tissue formation and angiogenesis respectively, two important events in tissue generation and engineering.^[7,33] Overall almost 100% cell viability was observed for PSF and minor toxicity for HUVEC up to 10 mg·mL⁻¹ and 96 hours of exposure time. The effect of the HUVEC cell line being more sensitive is noticeable already at lower concentrations (0.1 mg·mL⁻¹). The lower viability of 24h at all time points could be explained by batch variation or by the release or presence of a substance limited to the early stage of the assay (first 24

hours). However at a high concentration of 50 mg·mL⁻¹ toxicity is observed in the HUVEC cell line while for the PSF a mild toxicity is displayed. One can ultimately conclude that these particles display no to very mild toxicity up to (10 mg·mL⁻¹), with the HUVEC cell line being slightly more sensitive.

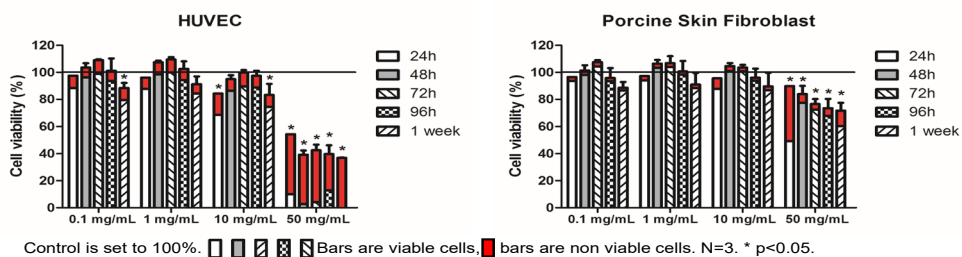


Figure 6.5. Dose response relationship between the MBH particles and HUVEC (left) and Porcine Skin Fibroblasts (right).

6.5 Conclusion

Functional precursor oligomers were successfully produced via the Morita-Baylis-Hillman step-growth polymerization using HDDA and TEGDA as acrylic linkers. These oligomeric resins contain double bonds along their backbone, and feature aldehyde endgroups, giving rise to a double functionality. Via suspension polymerization and using a simple stirring plate, polymeric microparticles were obtained in a consistent way, obtaining particle sizes between 150 and 250 μm from a Michael addition reaction with a tetrafunctional thiol. The particles are hydrolysable in basic conditions, as well as their linear precursors. As a proof of principle, the particles were post-modified by attaching aniline through the formation of an imine. Particles can hence be decorated with functional amines, and therefore be optimized for distinct biomedical applications. Further, particles are found to have no significant cytotoxicity on HUVEC and porcine skin fibroblasts. Only at high concentrations ($50 \text{ mg}\cdot\text{mL}^{-1}$) toxicity is observed, showing the potential of the cross-linked particles to serve as scaffolds in various biomedical applications, e.g. tissue engineering and drug release application. The variety of accessible functional groups on the surface and within the particles are an invitation for further functionalization.

6.6 References

- [1] T. Haider, C. Völker, J. Kramm, K. Landfester, F. R. Wurm, *Angew. Chemie Int. Ed.* **2018**, DOI 10.1002/anie.201805766.
- [2] Kenry, B. Liu, *Biomacromolecules* **2018**, *19*, 1783–1803.
- [3] T. Witko, M. Guzik, K. Sofińska, K. Stepien, K. Podobinska, *Biophys. J.* **2018**, *114*, 363a.
- [4] Y. Ikada, *Biomaterials* **1994**, *15*, 725–736.
- [5] K. Sevim, J. Pan, *Acta Biomater.* **2018**, *66*, 192–199.
- [6] D. Vinciguerra, S. Denis, J. Mougin, M. Jacobs, Y. Guillaneuf, S. Mura, P. Couvreur, J. Nicolas, *J. Control. Release* **2018**, *286*, 425–438.
- [7] Y. Wang, D. G. M. Molin, C. Sevrin, C. Grandfils, N. M. S. van den Akker, M. Gagliardi, M. L. Knetsch, T. Delhaas, L. H. Koole, *Int. J. Pharm.* **2016**, *503*, 150–162.
- [8] T. Maharana, S. Pattanaik, A. Routaray, N. Nath, A. K. Sutar, *React. Funct. Polym.* **2015**, *93*, 47–67.
- [9] G. Delaittre, A. M. Greiner, T. Pauloehrl, M. Bastmeyer, C. Barner-Kowollik, *Soft Matter* **2012**, *8*, 7323–7347.
- [10] V. Delplace, J. Nicolas, *Nat. Chem.* **2015**, *7*, 771–784.
- [11] S. Kobben, A. Ethirajan, T. Junkers, *J. Polym. Sci. Part A Polym. Chem.* **2014**, *52*, 1633–1641.
- [12] J. Vandenbergh, G. Ramakers, L. van Lokeren, G. van Assche, T. Junkers, *RSC Adv.* **2015**, *5*, 81920–81932.

- [13] J. Vandenberg, K. Ranieri, T. Junkers, *Macromol. Chem. Phys.* **2012**, *213*, 2611–2617.
- [14] N. Zaquen, B. Wenn, K. Ranieri, J. Vandenberg, T. Junkers, *J. Polym. Sci. Part a-Polymer Chem.* **2014**, *52*, 178–187.
- [15] J. Vandenberg, M. Peeters, T. Kretschmer, P. Wagner, T. Junkers, *Polymer.* **2014**, *55*, 3525–3532.
- [16] S. K. Reddy, K. S. Anseth, C. N. Bowman, *Polymer.* **2005**, *46*, 4212–4222.
- [17] T. O. Machado, C. Sayer, P. H. H. Araujo, *Eur. Polym. J.* **2017**, *86*, 200–215.
- [18] J. Chiefari, Y. K. Chong, F. Ercole, J. Krstina, J. Jeffery, T. P. T. Le, R. T. A. Mayadunne, G. F. Meijs, C. L. Moad, G. Moad, E. Rizzardo, S. H. Thang, *Macromolecules* **1998**, *31*, 5559–5562.
- [19] K. E. Price, S. J. Broadwater, B. J. Walker, D. T. McQuade, *J. Org. Chem.* **2005**, *70*, 3980–3987.
- [20] S. H. Ji, B. Bruchmann, H. A. Klok, *Macromol. Chem. Phys.* **2011**, *212*, 2612–2618.
- [21] S. Ji, B. Bruchmann, F. Wurm, H.-A. Klok, *J. Polym. Sci. Part A Polym. Chem.* **2012**, *50*, 25–34.
- [22] S. Ji, B. Bruchmann, H.-A. Klok, *Macromolecules* **2011**, *44*, 5218–5226.
- [23] J.-Y. Byeon, F. T. Limpoco, R. C. Bailey, *Langmuir* **2010**, *26*, 15430–15435.
- [24] D. K. Kölmel, E. T. Kool, *Chem. Rev.* **2017**, *117*, 10358–10376.
- [25] K. M. Hassell, J. R. Stutzman, S. A. McLuckey, *Anal. Chem.* **2010**, *82*, 1594–1597.

- [26] V. C. Cotham, J. B. Shaw, J. S. Brodbelt, *Anal. Chem.* **2015**, *87*, 9396–9402.
- [27] V. K. Aggarwal, I. Emme, S. Y. Fulford, *J. Org. Chem.* **2003**, *68*, 692–700.
- [28] C. Pretti, M. Renzi, S. Ettore Focardi, A. Giovani, G. Monni, B. Melai, S. Rajamani, C. Chiappe, *Ecotoxicol. Environ. Saf.* **2011**, *74*, 748–753.
- [29] B. Vazquez, C. Elvira, B. Levenfeld, B. Pascual, I. Goni, M. Gurruchaga, M. P. Ginebra, F. X. Gil, J. A. Planell, P. A. Liso, et al., *J. Biomed. Mater. Res.* **1997**, *34*, 129–136.
- [30] J. Favrot, D. Vocelle, C. Sandorfy, *Photochem. Photobiol.* **1979**, *30*, 417–421.
- [31] H. K. Makadia, S. J. Siegel, H. K. Makadia, S. J. Siegel, *Polymers.* **2011**, *3*, 1377–1397.
- [32] E. A. Kamoun, E.-R. S. Kenawy, X. Chen, *J. Adv. Res.* **2017**, *8*, 217–233.
- [33] D. Antoni, H. Burckel, E. Josset, G. Noel, *Int. J. Mol. Sci.* **2015**, *16*, 5517–27.

Chapter 7

Appendix

7.1 Figures

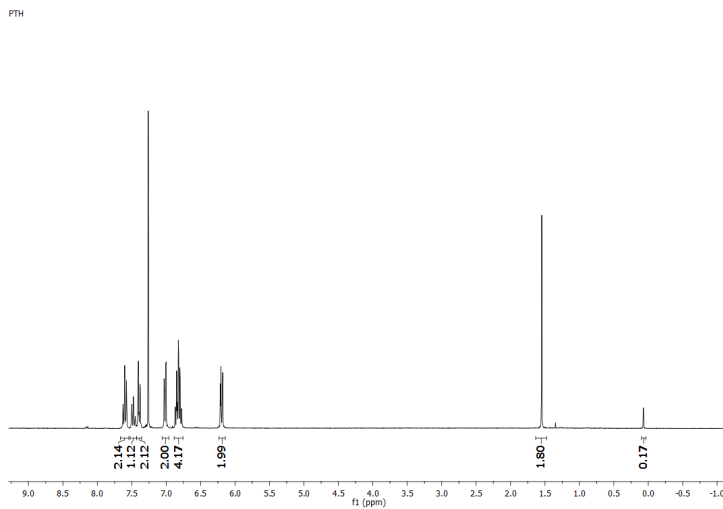


Figure A1. ^1H NMR spectrum 10-phenyl(phenothiazine).

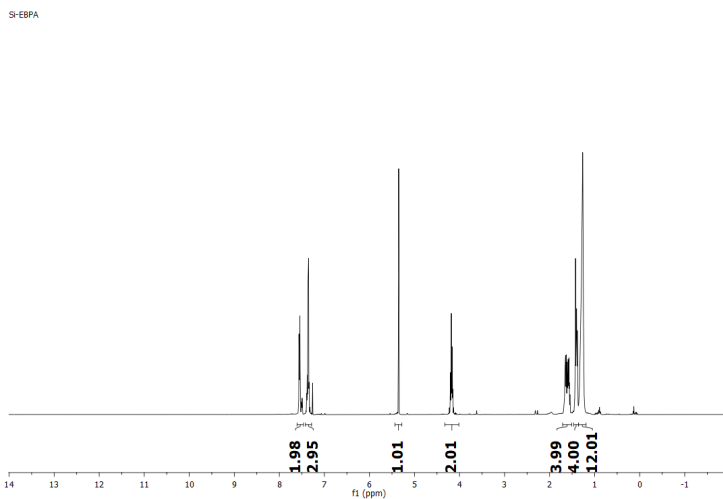


Figure A2. ^1H NMR spectrum of 11-(trichlorosilyl)undecyl 2-bromo-2-phenylethanoate.



Figure A3. Custom-made chamber with quartz glass window used for surface grafting.

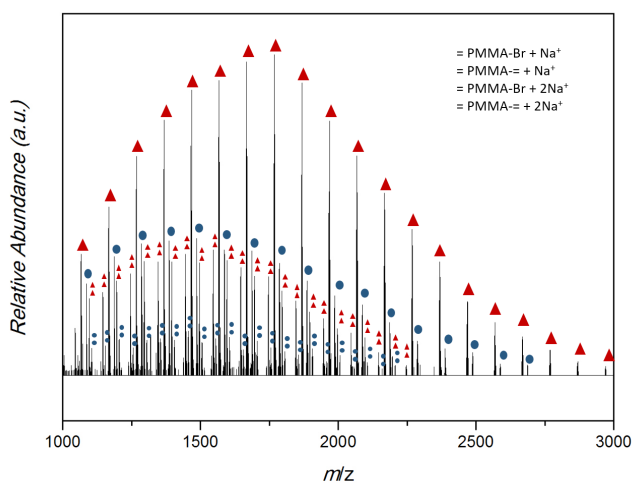


Figure A4. ESI-MS spectrum of metal-free ATRP of MMA. Distributions can be assigned to the bromine end-capped polymers and the bromine-eliminated polymers. Both also presented as single and double charged species.

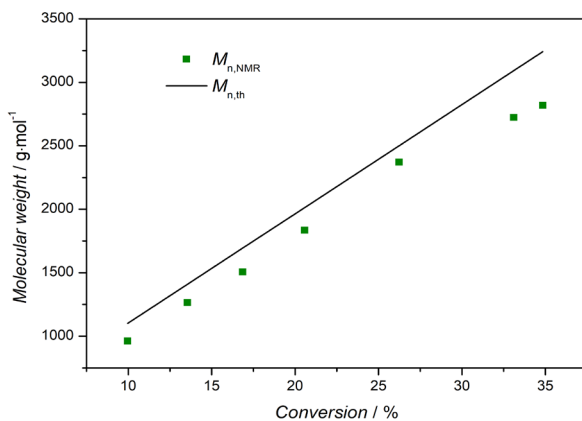


Figure A5: M_n is plotted against conversion for a metal-free ATRP of MAA in batch.

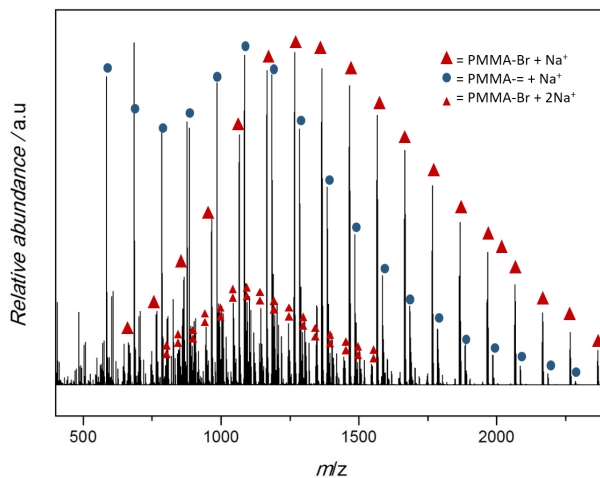


Figure A6. ESI-MS spectrum of PMMA produced via a metal-free ATRP flow reaction.

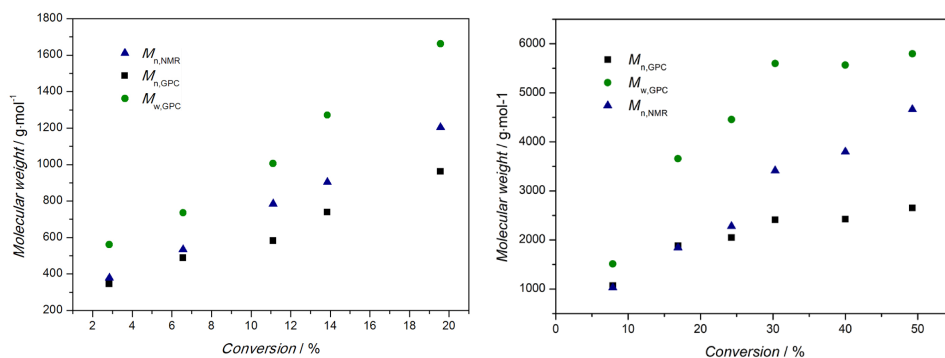


Figure A7. Comparison of M_n obtained via ^1H NMR with M_n and M_w obtained via GPC for metal-free polymerization of MAA in flow. Left plot: MMA/EBPA/PTH = 100/2/0.05, Right plot: MMA/EBPA/PTH = 100/1/0.05.

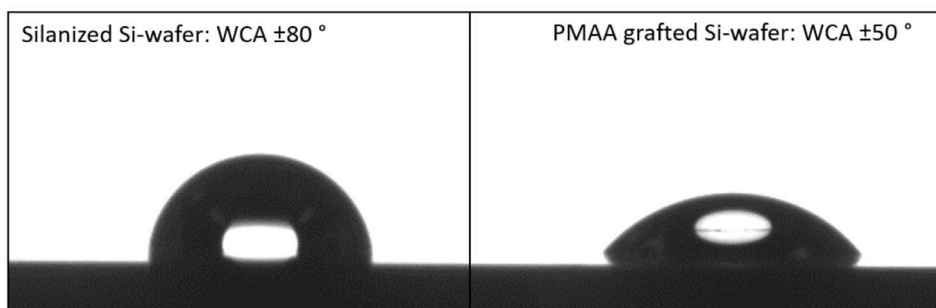


Figure A8. Results of water contact angle measurement comparing silicon wafers before and after grafting of PMAA.

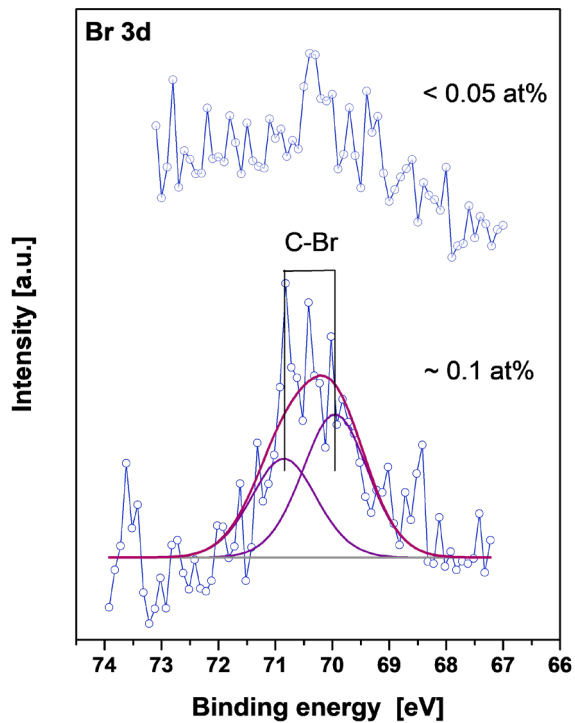


Figure A9. Br 3d XPS spectra before (top) and after (bottom) silanization. The presence of covalently bound Br, stemming from the ATRP initiator, can be detected in the silanized sample and confirms successful silanization.

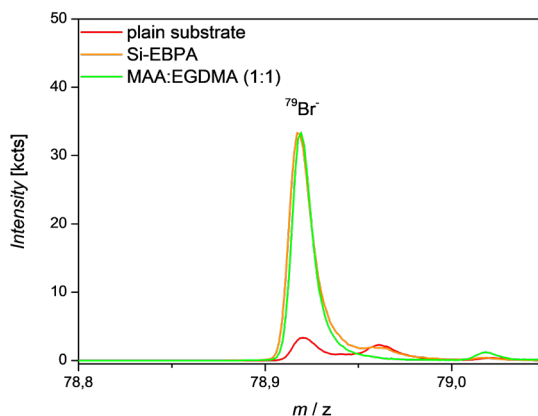


Figure A10. ToF-SIMS spectra showing bromine fragments (^{79}Br) of the plain substrate, after silanization, and after grafting of the polymer film (MAA:EGDMA; 1:1). This confirms the successful immobilization of the ATRP initiator and the conservation of the bromine after polymerization.

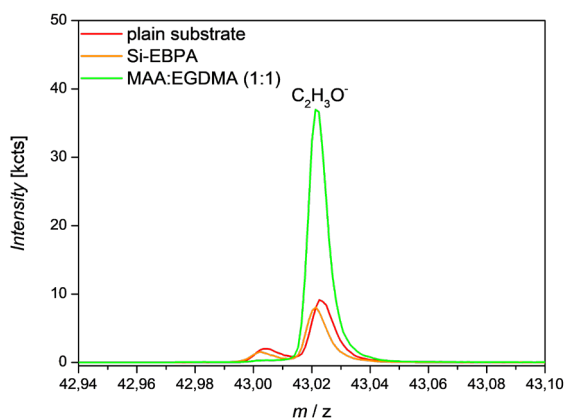


Figure A11: ToF-SIMS spectra showing $\text{C}_2\text{H}_3\text{O}^-$ signals, representing the grafted polymer, of the plain substrate, after silanization, and after grafting a polymer film with an experimental monomer ratio of 1:1; MAA:EGDMA. This confirms a successful polymer grafting.

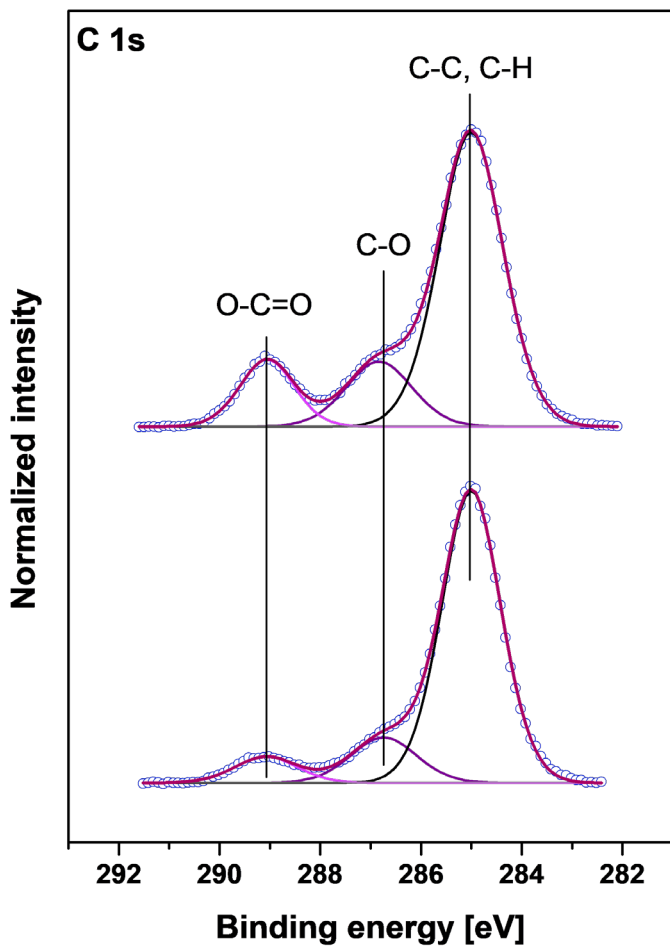


Figure A12: C 1s XPS spectra showing the contributions of O-C=O, C-O and C-C before (bottom) and after (top) polymer grafting. The ratio's of the contributions approach the expectations for a (meth)acrylic polymer film.

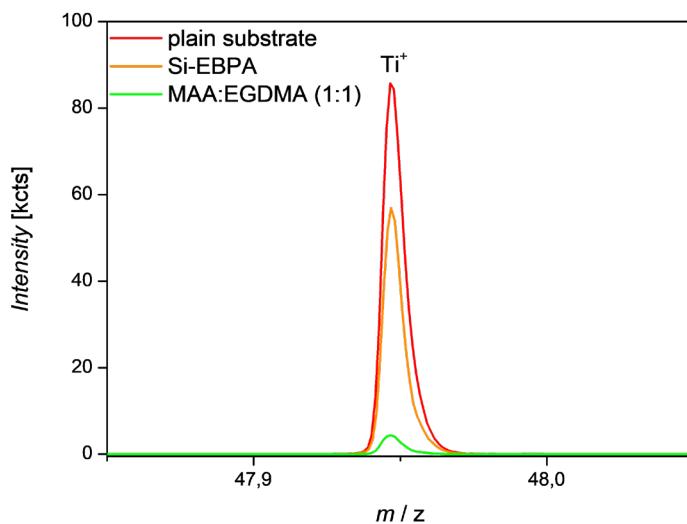


Figure A13: ToF-SIMS spectra showing ^{48}Ti signals of the plain silicon substrate, after silanization, and after grafting a polymer film produced with an experimental monomer ratio of 1:1; MAA:EGDMA.

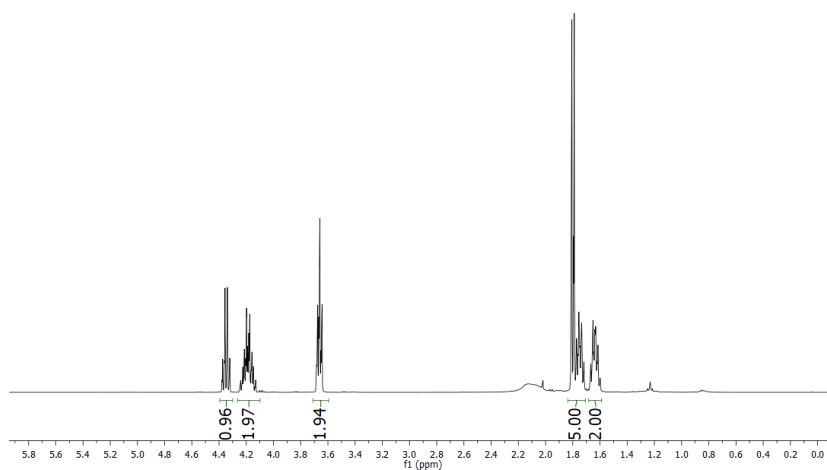


Figure A14. ^1H NMR spectrum of 4-hydroxybutyl 2-bromopropanoate.

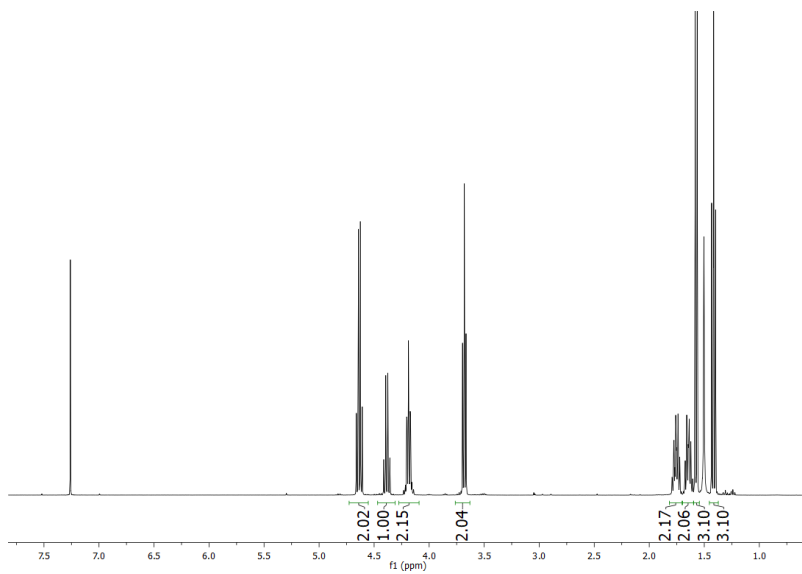


Figure A15. ¹H NMR spectrum of xanthate silane precursor.

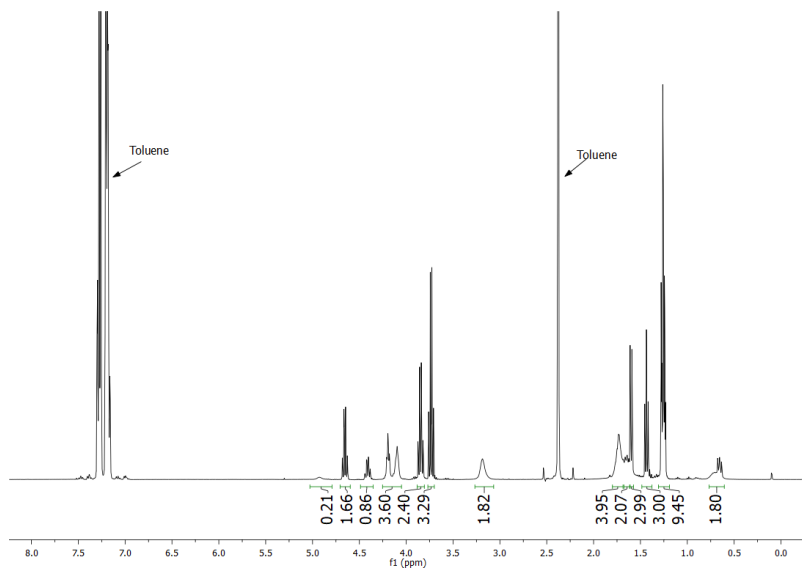


Figure A16. ¹H NMR spectrum of xanthate silane.

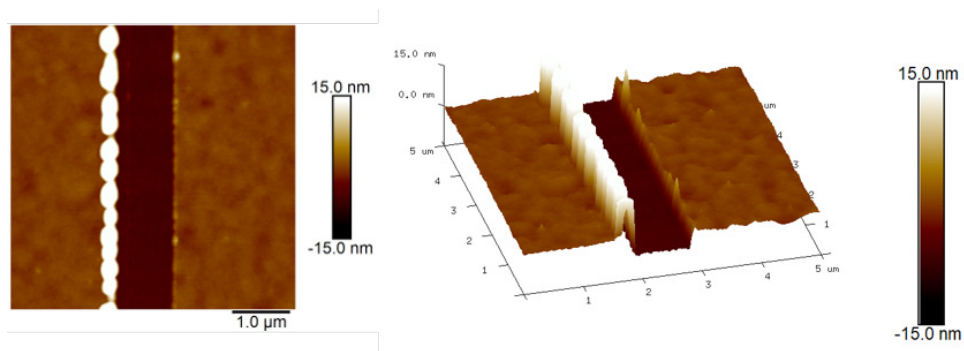


Figure A17. AFM image of surface initiated photoiniferter grafting of PMA resulting in smooth polymer films. 2D (left) and 3D (right).

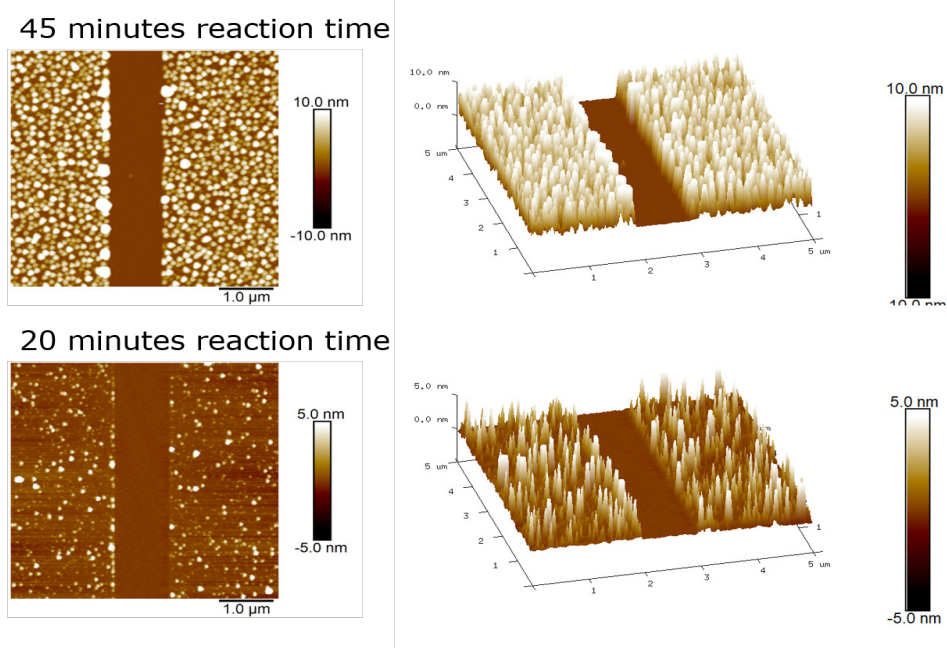
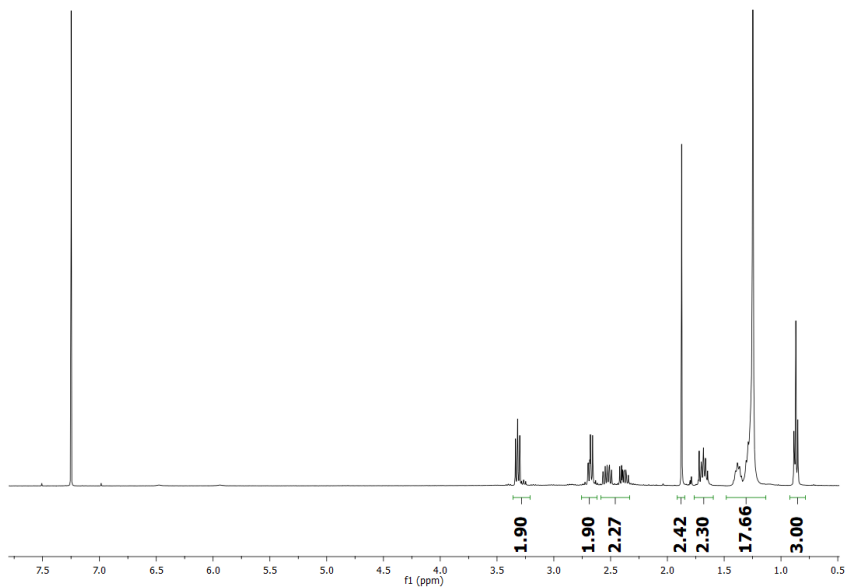
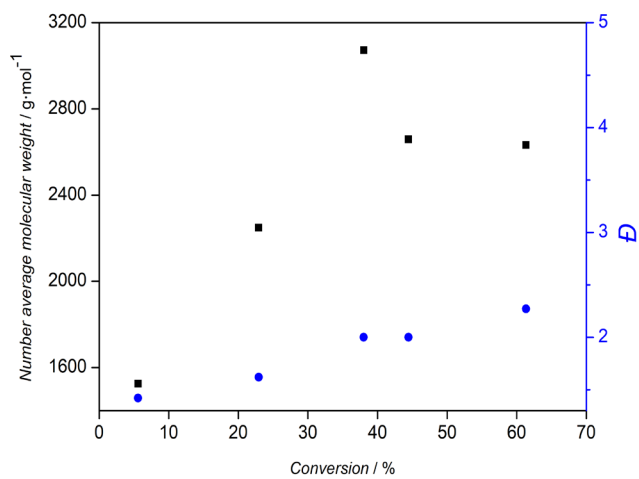


Figure A18. AFM image of surface initiated photoiniferter grafting of PMA resulting in polymer "mushrooms" comparing 45 minutes reaction time (top) and 20 minutes reaction time (bottom). 2D image (left) and 3D image (right).

Figure A19. ^1H NMR spectrum of CDP-TTC.Figure 20A. Number average molecular weight (M_n) versus conversion for the flow polymerization of PMMA using CDP-TTC and UV-light for initiation.

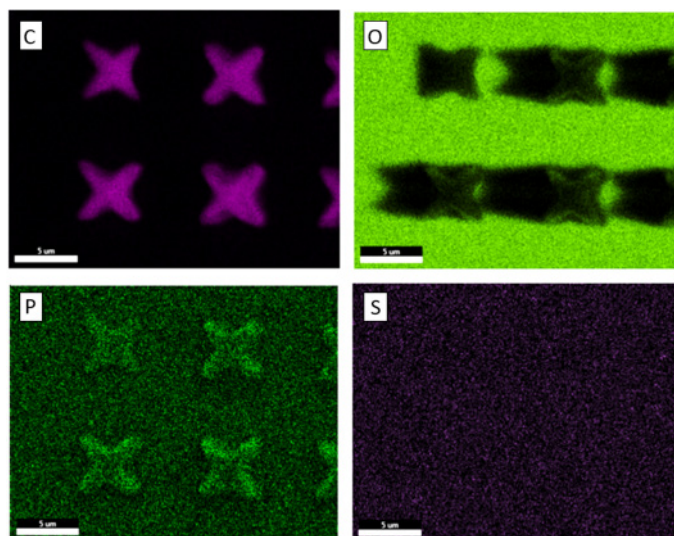


Figure A21. EDX mapping reveals the elemental contribution of carbon (C), oxygen (O), phosphorus (P) and sulfur (S). The resin comprised 5 mol% irgacure 819, mol% PMMA, TRIM and DMSO (45 vol%).

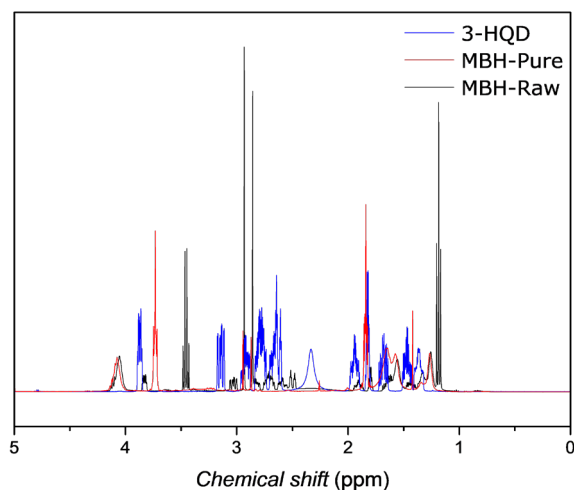


Figure A22. Overlay of ^1H -NMR spectra of 3-HQD and MBH polymer with HDDA as acrylic linker, before and after purification over a silica plug.

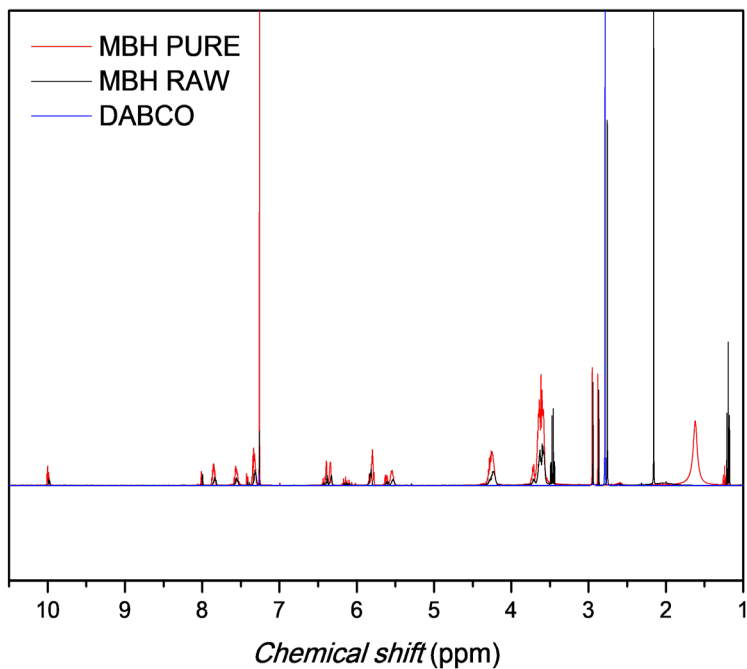


Figure A23. Overlay of ¹H NMR spectra of DABCO and MBH polymer with TEGDA as acrylic linker, before and after purification over a silica plug.

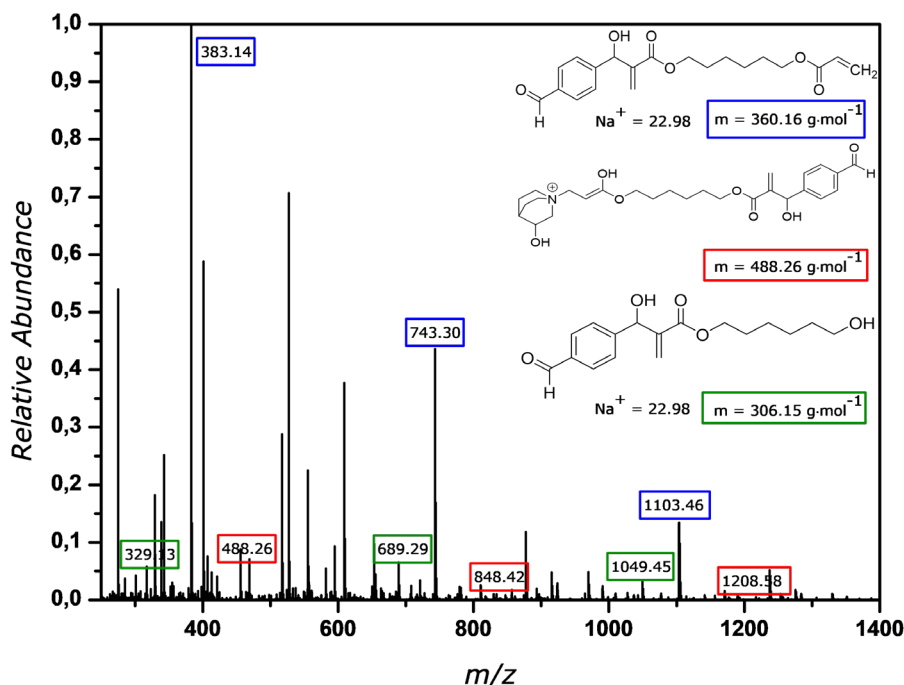


Figure A24: ESI spectrum from MBH polymer using HDDA as acrylic linker. The distribution assigned in blue represent a desired distribution. Other desired distributions, which were not assigned in this figure, have homo-telechelic aldehyde functionalities or acrylate functionalities. The red assignments are residues of polymer chains with catalyst still added to the activated alkene (despite a clean NMR spectrum). The distribution with green annotations represents the polymer chains end-capped with an impurity from the acrylic linker. Combinations of the above three are also possible.

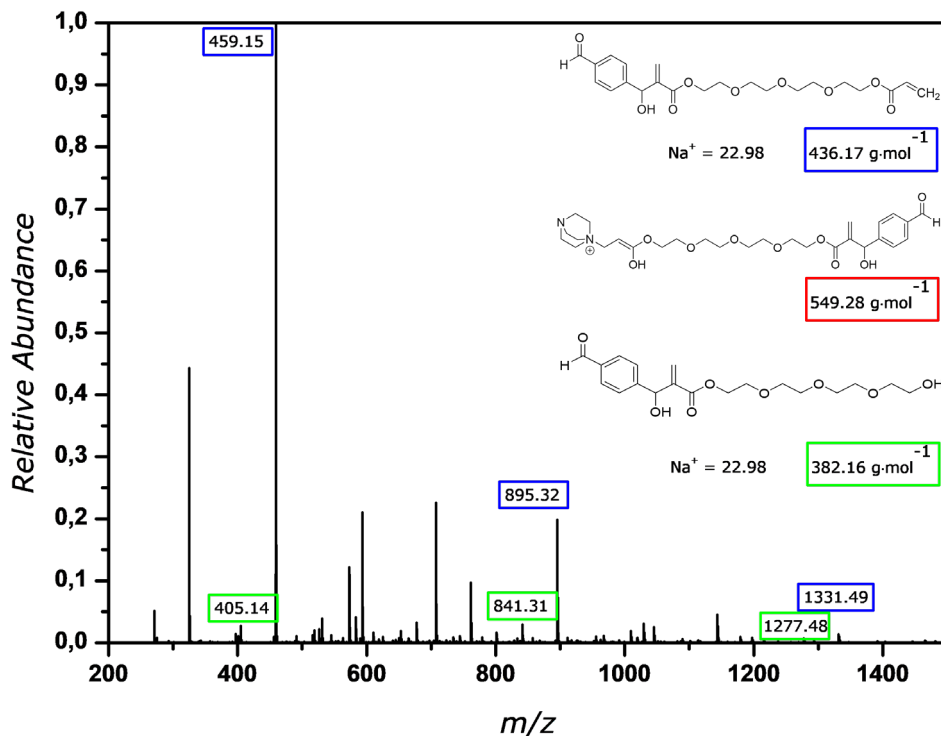


Figure A25: ESI spectrum from MBH polymer using TEGDA as acrylic linker. The distribution assigned in blue represent a desired distribution. Other desired distributions, which were not assigned in this figure, have homo-telechelic aldehyde functionalities or acrylate functionalities. The distribution with green annotations represents the polymer chains end-capped with an impurity from the acrylic linker. Combinations of the above three are also possible. The absence of the distribution containing the catalyst (red) indicate successful purification.

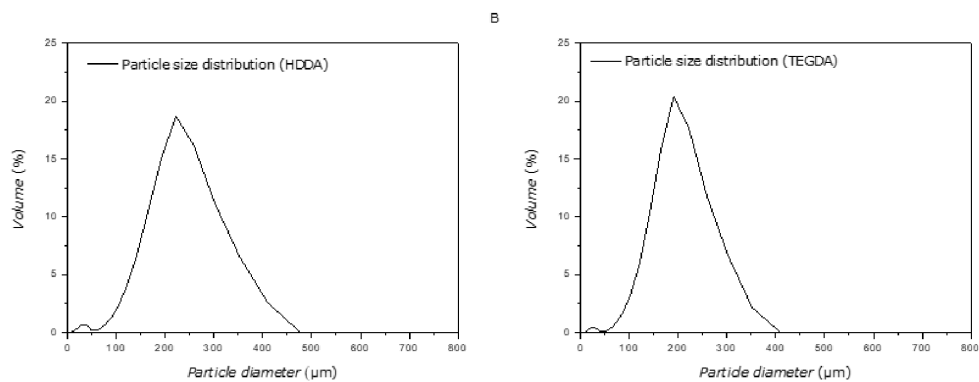


Figure A26. Size distribution of MBH polymer particles using HDDA (left) or TEGDA (right) as acrylic linker, obtained via mastersizer.

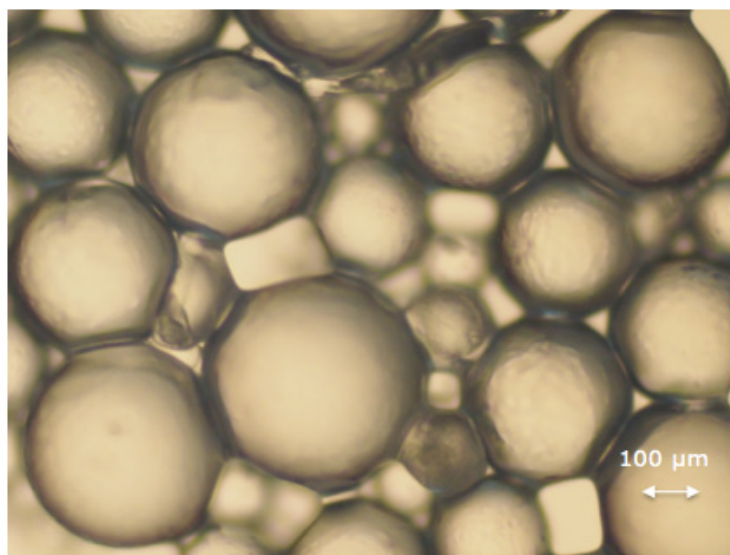


Figure A27. Optical microscopy images of MBH particles showing Particles using TEGDA as acrylic linker.

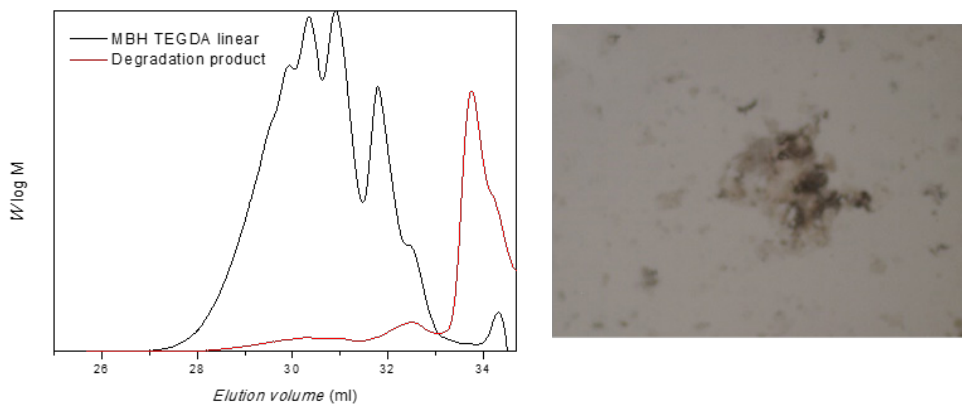


Figure A28. SEC (left) shows the evolution of the MBH polymers with TEGDA as acrylic linker to degradation product. Optical microscopy (right) shows degraded left overs of MBH particles with TEGDA as acrylic linker.

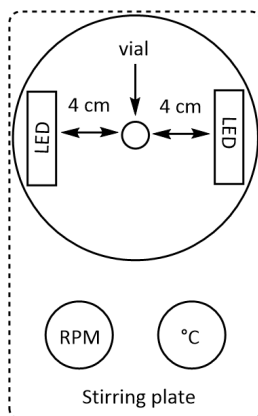


Figure A29. Schematic representation of the reaction set-up for the polymerization of PMMA and PMAA in batch using PTH catalyzed O-ATRP.



Figure A30. Picture of the microreactor used for the synthesis of the PMMA macroRAFT (picture made by Maarten Rubens). The microreactor is indicated by the black rectangle.

7.2 Tables

Table A1: Different targeted degrees of polymerization and resulting number average molecular weights (M_n) and dispersities.

M/I	$M_{n,NMR}$	$M_{n,GPC}$	\bar{D}
25	1139 g · mol ⁻¹		
50	1817 g · mol ⁻¹	1417 g · mol ⁻¹	1.3
100	3161 g · mol ⁻¹	2812 g · mol ⁻¹	1.55
250	10096 g · mol ⁻¹	8925 g · mol ⁻¹	1.8

Table A2. Comparison between polymerization of MMA via metal-free-ATRP in batch and in flow. Data was compared for 50% conversion (MMA/EBPA/PTH = 100/1/0.05).

Batch polymerization of MMA	Flow polymerization of MMA
12h Reaction time	120 minutes reaction time
$M_n = 4914 \text{ g} \cdot \text{mol}^{-1}$ (¹ H NMR)	$M_n = 4665 \text{ g} \cdot \text{mol}^{-1}$ (¹ H NMR)
$M_n = 5407 \text{ g} \cdot \text{mol}^{-1}$ (GPC)	$M_n = 2601 \text{ g} \cdot \text{mol}^{-1}$ (GPC)
$M_{n,th} = 5249 \text{ g} \cdot \text{mol}^{-1}$	$M_{n,th} = 5249 \text{ g} \cdot \text{mol}^{-1}$
$\bar{D} = 1.55$	$\bar{D} = 2.18$

Table A3. Comparison between polymerization of MAA via metal-free-ATRP in batch and in flow (MAA/EBPA/PTH =100/1/0.05).

Batch polymerization of MAA	Flow polymerization of MAA
10h Reaction time	120 minutes reaction time
$M_n = 2818 \text{ g}\cdot\text{mol}^{-1}$ ($^1\text{H NMR}$)	$M_n = 5642 \text{ g}\cdot\text{mol}^{-1}$ ($^1\text{H NMR}$)
$M_{n,\text{th}} = 3200 \text{ g}\cdot\text{mol}^{-1}$	$M_{n,\text{th}} = 5588 \text{ g}\cdot\text{mol}^{-1}$
34.8 % Conversion	64.9 % Conversion

Table A4. Ti metal and oxide contributions in atomic percentage (at%) before (only with immobilized ATRP initiator) and after polymer grafting with different experimental monomer ratio's of MAA and EGDMA (1:4; 1:1; 2:1; 4:1). The contribution of Ti can be related to the polymer film thickness.

MAA:EGDMA	Concentration / at%	
	Ti(0)	Ti(ox)
With ATRP initiator	2,0	17,0
1:4	0,5	5,0
1:1	0,2	2,3
2:1	1,2	11,7
4:1	1,3	13,5

Chapter 8

Materials & Characterization



8.1 Materials

8.1.1 Surface grafting

For the synthesis of 10-phenyl(phenothiazine) (PTH) following products were purchased from ABCR: phenothiazine (98%), 2-dicyclohexylphosphino-2',6'-diisopropoxybiphenyl (RuPhos, 98%), chloro(2-dicyclohexylphosphino-2',6'-diisopropoxy-1,1'-biphenyl)[2-(2'-amino-1,1'-biphenyl)]palladium(II) and (Ruphos precat, 98%). Sodium *tert*-butoxide (NaOtBu, 98%) and chlorobenzene (99%) were purchased from Acros. 1-4 Dioxane (Anal. Grade, Fisher) and chlorobenzene were dried over mol. sieves (VWR, 3Å).

For the synthesis of 11-(trichlorosilyl)undecyl 2-bromo-2-phenylethanoate, α -bromophenylacetic acid (98%) and 10-undecen-1-ol (98%) were purchased from TCI, Karstedt's catalyst from ABCR, pyridine (anhydrous, 99%) from Acros, 4-(dimethylamino)pyridine (DMAP, 99%) from Acros, 1-Ethyl-3-(3-dimethylaminopropyl)carbodiimide (EDC) from Acros (97%) and trichlorosilane from Aldrich (99%).

The monomers used for polymerization were purified over basic alumina before usage. Methyl methacrylate (MMA) was purchased from Acros (99%), methacrylic acid (MAA) from Sigma Aldrich (99%), ethylene glycol dimethacrylate (EGDMA) from TCI (97%) and methyl acrylate from Acros (99%). The initiator Ethyl α -bromophenylacetate (EBPA) was purchased from Acros (97%).

For the synthesis of the xanthate silane, *N,N'*-dicyclohexylcarbodiimide (DCC) was obtained from Acros (99%), butandediol from Acros (99%), 2-bromopropionic acid from Alfa Aesar (98%), potassium ethyl xanthogenate from Acros (97%), 3-(triethoxysilyl) propyl isocyanate (95%) from ABCR and dibutyl tin dilaurate from Acros (94%).

8.1.2 Side projects

For the synthesis of the CDP-TTC RAFT following chemicals were used: 4,4'-azobis(4-cyanovaleric acid) (ACVA, Sigma-Aldrich, 98%), carbon disulfide (Fisher, 99.9%), 1-dodecanethiol (TCI, 95%), p-toluenesulfonyl chloride (TCI, 99%)

For the preparation of the Resin poly(ethylene glycol) methyl ether acrylate (PEGA, $M_n = 480 \text{ g}\cdot\text{mol}^{-1}$) was obtained from Aldrich, trimethylolpropane trimethacrylate (TRIM) from TCI (90%) phenyl bis(2,4,6-trimethylbenzoyl)phosphine oxide (Irgacure 819) was obtained from TCI (95%).

For the synthesis of the Morita-Baylis-Hillman polymers following monomers and catalysts were purchased: terephthalaldehyde (TA, Acros Organics; 98%), 1,6-hexanediol diacrylate (HDDA, Sigma Aldrich; 80%), tetra(ethylene glycol) diacrylate (TEGDA, Sigma Aldrich; technical grade), 1,4-diazabicyclo[2.2.2.] octane (DABCO, Acros Organics; 97%), 4-dimethylaminopyridine (DMAP, Acros Organics; 97%), 3-quinuclidinol (3-HQD, Sigma Aldrich; 99%).

For the suspension polymerization pentaerythriol tetrakis(3-mercaptopropionate) (PETMP, Sigma Aldrich; >95%), poly(vinylalcohol) (PVA, Acros Organics; 88% hydrolyzed, average MW 22000) and hexylamine (HA, Sigma Aldrich; 99%) were used. Aniline was bought from Acros Organics (99.8%).

All solvents used were obtained from commercial sources (Acros, VWR, Sigma-Aldrich, Fisher) and used without further purification.

8.2 Characterization

Time-of-Flight Secondary Ion Mass Spectrometry (ToF-SIMS) was performed on a TOF. SIMS5 instrument (ION-TOF GmbH, Münster, Germany). This spectrometer is equipped with a Bi cluster primary ion source (field emission from liquid Bi wetting a tungsten tip) and a reflectron type time-of-flight analyzer. UHV base pressure during analysis was $< 7 \cdot 10^{-9}$ mbar. For high mass resolution the Bi source was operated in the "high current bunched" mode providing short Bi_3^+ primary ion pulses at 25 keV energy, a beam diameter of approx. 4 μm , and a target current of 0.5 pA at 10 kHz repetition rate. The short pulse length of 1.2 ns allowed for high mass resolution (approx. 5500 $\text{m}/\Delta\text{m}$). The primary ion beam was rastered across a $500 \times 500 \mu\text{m}^2$ field of view on the sample, and 128×128 data points were recorded. Primary ion dose densities were held at $1 \times 10^{11} \text{ cm}^{-2}$ to ensure quasi-static conditions. Spectra were calibrated on C^+ , CH^+ , CH_2^+ , and CH_3^+ ; or C^- , CH^- , CH_2^- , and C_2^- ; respectively. Spectra are presented as signal intensities with 3 point binning.

X-Ray Photoelectron Spectroscopy (XPS) measurements were performed using a K-Alpha+ XPS spectrometer (ThermoFisher Scientific, East Grinstead, UK). Data acquisition and processing using the Thermo Avantage software is described elsewhere.^[1] All thin films were analyzed using a microfocused, monochromated Al K α X-ray source (400 μm spot size). The kinetic energy of the electrons was measured by a 180° hemispherical energy analyzer operated in the constant analyzer energy mode (CAE) at 50 eV pass energy for elemental spectra. The K-Alpha+ charge compensation system was employed during analysis, using electrons of 8 eV energy, and low-energy argon ions to prevent any localized charge build-up. The spectra were fitted with one or more Voigt profiles (BE uncertainty: ± 0.2 eV) and Scofield sensitivity factors were applied for quantification.^[2] All spectra were referenced to the C 1s peak (C-C, C-H) at 285.0 eV binding energy

controlled by means of the well-known photoelectron peaks of metallic Cu, Ag, and Au, respectively.

Proton Nuclear Magnetic Resonance (^1H NMR) spectra of solutions in $(\text{CD}_3)_2\text{SO}$ or CDCl_3 were recorded at room temperature on an Agilent/Varian Inova 400 spectrometer using a 5 mm OneNMR Pulsed-Field-Gradient (PFG) probe. The chemical shift scale (δ ; in ppm) was calibrated relatively to the residual proton signals of the deuterated solvents (for DMSO at 2.50 ppm or for CHCl_3 at 7.26 ppm).

Gel Permeability Chromatography – Size Exclusion Chromatography (GPC-SEC) was performed on a Tosoh EcoSEC operated by PSS WinGPC software, equipped with a PLgel 5.0 μm guard column (50 \times 8 mm), followed by three PLgel 5 μm mixed-C columns (300 \times 8 mm) and a differential refractive index detector using THF as eluent at 40 $^\circ\text{C}$ with a flow rate of 1 $\text{mL} \cdot \text{min}^{-1}$. The SEC system was calibrated using linear narrow PS standards ranging from $474 \times 7.5 \times 10^6 \text{ g mol}^{-1}$ PS ($K = 14.1 \times 10^{-5} \text{ dL g}^{-1}$ and $a = 0.70$), and toluene as a flow marker.^[3]

Contact Angle Measurement The contact angle measurement sessile drop method was performed on a DataPhysics OCA-15 plus with distilled H_2O via the sessile drop method.

Electrospray ionization mass spectrometry (ESI-MS) was performed using an LTQ orbitrap velos pro mass spectrometer (ThermoFischer Scientific) equipped with an atmospheric pressure ionization source operating in the nebulizer assisted electro spray mode. The instrument was calibrated in the m/z range 220 – 2000 using a standard solution containing caffeine, MRFA and Ultramark 1621. A constant spray voltage of 5 kV was used and nitrogen at a dimensionless sheath gas flow rate of 7 was applied. Capillary temperature was set to 275 $^\circ\text{C}$. A mixture of THF and methanol (THF : MeOH = 3 : 2), all of HPLC grade, was used as the solvent. Spectra were analyzed using Thermo Xcalibur Qual Browser software.^[4]

For **Atomic Force Microscopy (AFM)** a Bruker Icon AFM was used with AC160Ts tip for the measurements. Scratching was done in contact mode while measurements were performed in tapping mode.

Optical Microscopy images of the polymer particles were made with an Olympus BX 41 optical microscope, magnification 10x. Pictures were taken with an Olympus PEN lite E-PL3 Micro with a BX41 lens of Olympus Digital with adapter Four Thirds MMF-2.

To confirm post modification of the particles with **Attenuated Total Reflectance Infrared spectroscopy (ATR-IR)**, a Bruker Tensor-27 equipped with an ATR probe Pike MIRacle 19993 and an MIR detector. Spectra were measured with a resolution of 4 cm^{-1}

Grazing angle attenuated tot reflection Fourier-Transform infrared (GAATR-FTIR) spectra were obtained from the dry polymer layers using a Frontier FTIR spectrometer (PerkinElmer) equipped with an MCT detector and a veemax III attachment (PIKE technologies). For the collection of the spectra, a resolution of 4 cm^{-1} was selected.^[5]

To obtain extra information about the particle size and distribution, a **mastersizer** from Malvern instruments (Malvern mastersizer-S, Worcs., UK) was applied. Distilled water was used as dispersing medium and poly(vinylalcohol) was used as additive. Laser transmitter: minimum 2 mW He-Ne laser (633 nm wavelength) with 18 mm beam diameter, collimated and spatially filtered to a single transverse mode. Receiver: Fourier transformation lens mount; lens 300RF with size range 0.05 – 880 μm . Calculation of the particle size distribution was based on a relative refractive index of 1.3300 and a beam length of 2.40 nm. Five subsequent measurements were performed with an intermediate time range of 5 min per run.

Height profile measurements and 2D maps were acquired on a 3D laser scanning confocal microscope (Keyence VK-X250).

The morphology of the microstructures was analyzed with **scanning electron microscopy** (SEM; FEI VERSA, Netherlands), coupled with elemental analysis with **energy-dispersive X-ray spectroscopy** (EDX; TEAM EDS system from EDAX, USA)

8.3 References

- [1] K. L. Parry, A. G. Shard, R. D. Short, R. G. White, J. D. Whittle, A. Wright, *Surf. Interface Anal.* **2006**, *38*, 1497–1504.
- [2] J. H. Scofield, *J. Electron Spectros. Relat. Phenomena* **1976**, *8*, 129–137.
- [3] E. Baeten, S. Vanslambrouck, C. Jérôme, P. Lecomte, T. Junkers, *Eur. Polym. J.* **2016**, *80*, 208–218.
- [4] J. J. Haven, J. Vandenberg, R. Kurita, J. Gruber, T. Junkers, *Polym. Chem.* **2015**, *6*, 5752–5765.
- [5] J. Laun, Y. De Smet, E. Van de Reydt, A. Krivcov, V. Trouillet, A. Welle, H. Möbius, C. Barner-Kowollik, T. Junkers, *Chem. Commun.* **2018**, *54*, 751–754.

Chapter 9

Summary & Outlook

9.1 Summary

A chemical sensor is a powerful tool to improve diagnostics and therapeutics in the clinical field. For example, real-time monitoring of *in vivo* analyte concentrations via novel developed chemical sensors can add to the understanding of pathologies and the progression of patients. In order to accomplish this, there is a need for production routes that allow miniaturization of these sensors, which make them suitable for medical applications.

Antibodies are frequently used in chemical sensors as they are well-known for their specific interaction with target molecules. Their synthetic counterparts are molecularly imprinted polymers (MIPs), which specifically interact with an analyte based on a variety of chemical interactions. The use of synthetic materials over their biological counterparts guarantees a better shelf-life, low production cost and good survival rate in harsh environmental conditions. The building blocks for MIPs (monomers) exhibit specific chemical functionalities, like acids. Synthesis routes have to be carefully chosen to be compatible with this type of monomer and preserve its function as recognition element.

Miniaturization of MIP-based sensors is enabled through the production of direct surface-grown MIPs (instead of MIP particle deposition). Furthermore, by using light sources to initiate the polymerization reaction, spatial and temporal control can be achieved. By choosing a reversible deactivation radical polymerization (RDRP), better control over the polymer film can be achieved, with concomitant improved binding efficiencies for the MIPs.

The first step in this thesis was to optimize a photo-mediated RDRP suitable for the production of surface-grafted polymers using monomers relevant for MIPs. Secondly, the specific reaction condition had to be determined to produce a working MIP film and characterize its sensor abilities.

To start, a synthesis route was optimized for the polymerization of methacrylic acid (MAA), which is a monomer that is widely used for MIPs. This was achieved by using a metal-free, organocatalyzed, photo atom transfer radical polymerization (photoATRP). While this is considered impossible for a classical ATRP route, metal-free ATRP of methyl methacrylate (MMA), as a reference, and MAA were investigated in solution and continuous flow. This revealed that control over the molecular weight was directly assessed only at significant monomer conversions. At lower conversions, a confusing mismatch concerning the molecular weight was observed in gel permeability chromatography (GPC) and proton nuclear magnetic resonance (^1H NMR). In addition, electrospray ionization mass spectrometry (ESI-MS) revealed some loss of end-groups. Ultimately, PMAA brushes were successfully grafted from planar silicon wafers resulting in thin films of around 4 nm. This thickness is sufficient for the imprinting of analytes.

The synthesis route described above was elaborated to graft cross-linked non imprinted polymer (NIP) films, copolymerizing MAA and ethylene glycol dimethacrylate (EGDMA) from titanium substrates. Grafting was initiated by using a UV-laser, which provides initiation that is more efficient and allows for the production of more complex polymer patterns. X-ray photoelectron spectroscopy (XPS) and time-of-flight secondary ion mass spectrometry (ToF-SIMS) revealed the real respective monomer contributions in the polymer film. By varying the monomer ratios, the threshold to incorporate MAA was observed to be at 2:1 MAA:EGDMA. This is essential to have a working MIP sensor. After grafting the polymer film in presence of the template analyte, histamine, the function of the MIP film was directly characterized with electro impedance spectroscopy (EIS). This nicely demonstrated the specific recognition of histamine with a limit of detection of 3.4 nM of histamine in phosphate buffer saline (PBS).

As an alternative, surface initiated photoiniferter using xanthates was investigated. In contrast to photoATRP, no catalyst is required. Photoiniferter is compatible with

a vast library of monomers and its mechanism is comparable to photo reversible addition fragmentation degenerative chain transfer (RAFT) polymerization, but without the addition of exogenous radical initiators. This reaction is straightforward in a sense that only monomers and solvent are added to the activated substrates before irradiation by UV-light. The xanthates were successfully immobilized on a silicon wafer, as confirmed by ToF-SIMS. The grafting of poly(methyl acrylate) (PMA), a reference for MIP relevant acrylates, was confirmed via ToF-SIMS and XPS. FTIR revealed a continuing monomer conversion over reaction time up to 45 minutes. Atomic force microscopy (AFM) detected a film thickness of 25 nm after 30 minutes reaction time. However, significant reproducibility issues are observed which resulted in the grafting of polymer "mushrooms" instead of the desired smooth films. This indicates a low grafting density, which could be caused by partial degradation of the xanthate functionality or interference with the silanization process. The chemical pathways developed within this project can possibly serve as a route for the production of MIP films. However, the reproducibility issues need to be addressed before further conclusion about the reaction's feasibility can be drawn. This project shows the chemistry is working and can possibly serve as a route to produce MIP films.

As a side project, functional resins were developed for two-photo polymerization (2PP). 2PP is a popular tool to directly 3D print polymeric structures with high resolution. A 2PP resin generally comprises cross-linkers and specific photoinitiators. In this project, an oligomer produced via RAFT polymerization (macroRAFT), was added. This induces a RAFT mechanism for 2PP while so far only free radical polymerization was reported. In this way a variety of post-modifications reactions are enabled and concomitant control over the mechanical and chemical properties of the 3D structures is allowed. Scanning electron microscopy (SEM) confirms the printing of 3D "X"-shaped structures with up to 10 mol% macroRAFT. Energy dispersive x-ray spectroscopy confirmed the presence of the trithiocarbonate.

Preliminary data show promising results for the post-modification via aminolysis of the RAFT agents and subsequent Michael addition of polyethylene glycol acrylate.

For a second side project, Morita-Baylis-Hillman (MBH) step growth polymerization was performed to produce densely functionalized oligomers. These MBH adducts were cross-linked in suspension using thiol-ene Michael addition reactions, yielding polymer microparticles. Degradability experiments proof the degradation of the polymer particles in basic media and cytotoxicity tests revealed good biocompatibility. As a proof of concept, the possibility to post modify the particles is displayed through the formation of imines, a popular bioconjugation reaction.

9.2 Nederlandse samenvatting

Een chemische sensor is een krachtige tool om de kwaliteit van diagnostische bepalingen en therapieën te verbeteren. Een voorbeeld hiervan is het *real-time* monitoren van *in vivo* analiet concentraties. Dit kan bijdragen tot een betere kennis omtrent pathologieën en de progressie van patiënten. Om dit te verwezenlijken is er nood aan syntheseroutes die het toelaten om zulke sensoren te miniaturiseren en dus inzetbaar te maken voor medische toepassingen.

In chemische sensoren worden antilichamen frequent gebruikt als receptoren gezien deze bekend zijn voor hun specifieke herkenning en interactie met respectievelijk doelmoleculen. De synthetische tegenhangers van antilichamen zijn zogenaamde MIPs of moleculair ingeprinte polymeren die de interactie met het doelmolecule aangaan op basis van verschillende chemische interacties. Het gebruik van synthetische materialen geeft als voordeel een verbeterde levensduur van het materiaal, een lagere productie kost en een goede compatibiliteit met de variëteit aan fysiologische condities. De bouwstenen voor MIPs (namelijk monomeren) bevatten enkele specifieke chemische functionaliteiten, zoals zuren. De syntheseroutes moeten afgesteld worden op deze types monomeer zodat hun

eigenschappen met betrekking tot moleculaire herkenning worden behouden.

De miniaturisatie van MIP gebaseerde sensoren wordt mogelijk gemaakt door het direct groeien van MIPs vanaf het oppervlak van een substraat i.p.v. het afzetten van MIP partikels waarbij voorgesynthetiseerde partikels worden geïmmobiliseerd. Daarbij wordt, door het gebruik van lichtbronnen ter initiatie van de polymerisatie reactie, een zowel ruimtelijke als temporele controle verkregen. Door gebruik te maken van een reversibele deactiveerbare radicalaire polymerisatie (RDRP) kan er een betere controle over de eigenschappen van de gegroeide MIP film worden bekomen. Dit gaat gepaard met verbeterde bindingseigenschappen van de MIPs.

De eerste stap in deze thesis was om een foto-gemedieerde RDRP te optimaliseren voor de productie van oppervlak gegroeide polymeren, opgebouwd uit zure monomeren. Vervolgens werden de reactie condities aangepast om een functionele MIP sensor te kunnen produceren. Ten slotte werd de MIP sensor dan gekarakteriseerd.

Eerst werd een syntheseroute geoptimaliseerd voor de polymerisatie van methacrylzuur (MAA) dat een veel gebruikt monomeer is voor MIPs. Dit doel werd bereikt door gebruik te maken van organogekatalyseerde foto *atom transfer radical polymerization* (ATRP). Ondanks dat klassieke ATRP initieel niet compatibel is met zure monomeren, werd dit metaal vrije alternatief getest voor de polymerisatie van methyl methacrylaat (MMA) en MAA in *batch* en in *flow* reactoren. Hieruit kon worden afgeleid dat controle over de moleculaire massa alleen bekomen kon worden bij hogere monomeer conversies. Bij lagere conversies werd er een mismatch waargenomen tussen GPC (*gel permeability chromatography*) en NMR (*nuclear magnetic resonance*). ESI-MS (*electrospray ionization mass spectrometry*) toont aan dat er geen volledig behoud van eindgroepen is. Uiteindelijk werden PMAA-ketens gegroeid vanaf siliciumoxide. De dikte van de polymeer film bedroeg ongeveer 4 nm. Deze dikte is voldoende om het inprenten van de uiteindelijke

doelmoleculen mogelijk te maken.

De hierboven aangehaalde syntheseroute werd vervolgens geoptimaliseerd voor het groeien van vernette polymeer filmen van titanium substraten, gebruik makend van MAA en ethylene glycol dimethacrylaat (EGDMA). De gebruikte lichtbron was een UV-laser die voorziet in een efficiëntere initiatie en het groeien van complexere polymeer patronen toelaat. Met XPS (*x-ray photoelectron spectroscopy*) en ToF-SIMS (*time-of-flight secondary ion mass spectrometry*) kon de werkelijke bijdragen van de respectievelijke monomeren worden achterhaald. Door de experimentele monomeer ratio's vervolgens aan te passen werden de optimale condities vastgesteld rond 2:1 MAA:EGDMA. Dit gegeven is essentieel om een functionele MIP sensor te kunnen bekomen. Vervolgens kon een polymeer film gegroeide worden in aanwezigheid van het doelmolecule, nl. histamine. De werking van de MIP film werd rechtstreeks via impedantie gekarakteriseerd. Dit toonde de goede specificiteit van de sensor aan met een gemeten detectielimiet rond 3.4 nM van histamine in PBS.

Als alternatieve syntheseroute werd ook fotoiniferter onderzocht. Bij fotoiniferter zijn er geen benodigde katalysatoren en de route is compatible met een grote verscheidenheid aan monomeren. De reactie is straight-forward in die zin dat, na het functionaliseren van het substraat, slechts monomeer en eventueel solvent dient toegevoegd te worden voordat deze blootgesteld worden aan de UV-bron. In dit project werden xanthaten geïmmobiliseerd op siliciumoxide substraten, zoals bevestigd door ToF-SIMS. Het groeien van methyl acrylaat ketens (PMA), die hier als referentie werden gebruikt, werd bevestigd door XPS en ToF-SIMS. Infrarood spectroscopie toonde vervolgens aan dat er een continue monomeer conversie was over tijd, tot 45 minuten. AFM (*atomic force microscopy*), nam een polymeer film waar met een dikte van 25 nm na 30 minuten reactietijd. Er werden echter problemen met de reproduceerbaarheid van de resultaten vastgesteld. In gelijkaardige condities werden ook "paddenstoelen" waargenomen i.p.v. van

een homogene polymeer film. Dit zou verklaard kunnen worden door een lage dichtheid van xanthaten aan het oppervlak. Mogelijk is dit te wijten aan een eventuele degradatie van de xanthaten of een verhinderde immobilisatie daarvan. Om uitspraken te kunnen doen over de haalbaarheid van dit project zouden eerst hiervoor verklaringen moeten worden gevonden. Het project toont echter aan dat het mogelijk is PMA te groeien door gebruik te maken van fotoiniferter, wat vervolgens impliceert dat dit onderzocht kan worden om van het oppervlak gegroeide MIPs te produceren.

In een zij-project werd de ontwikkeling van functionele polymeerhars voor twee-foton polymerisatie (2PP) aangewend. 2PP is een populaire tool om polymere structuren te 3D-printen met hoge resolutie. Een 2PP hars bestaat meestal uit *cross-linkers* (die zorgen voor vernetting) en specifieke initiators. In dit project werd een oligomeer dat geproduceerd werd via RAFT (*reversible addition fragmentation degenerative chain transfer*) polymerisatie aan de hars toegevoegd. Hierdoor werd een RAFT mechanisme geïnduceerd voor 2PP terwijl tot nu toe alleen 2PP werd gerapporteerd in combinatie met een vrij radicalaire polymerisatie. Op deze manier worden er een aantal opties toegevoegd die het toelaten om de 3D structuren te post-modificeren. Verder wordt er meer controle over de mechanische en chemische eigenschappen bekomen. SEM (*scanning electron microscopy*) bevestigde dat de 3D structuren met succes werden geprint, gebruikmakend van 10 mol% RAFT oligomeer. EDX (*energy dispersive x-ray*) spectroscopie kon vervolgens de aanwezigheid van trithiocarbonaten vaststellen. Veel belovende, preliminaire resultaten werden bekomen voor de post-modificatie van de structuren via aminolyse van de trithiocarbonaten en daaropvolgende Michael additie van polyethyleen glycol acrylaat.

Bij een tweede zij-project werd gebruik gemaakt van de Morita-Baylis-Hillman stap groei polymerisatie voor de productie van dicht gefunctionaliseerde oligomeren. Deze MBH precursoren werden vernet in suspensie via de thiol-een Michael additie

om polymeer micropartikels te bekomen. Degradatie experimenten tonen de degradatie aan van de partikels in basisch medium. Toxiciteitstesten bewijzen vervolgens dat deze een goede bio compatibiliteit hebben. Tenslotte werden de partikels, bij wijze van *proof of concept*, gemodificeerd via de formatie van imines, een populaire reactie voor bio conjugatie.

9.3 Outlook

A good first step was taken towards the production of surface-grown MIPs using photomediated RDRP. The sensor reported in this thesis was optimized for histamine. This grafting strategy should however be transferable to different targets. For each new target analyte, optimization of the preparation protocol is required. This includes the reaction conditions, the extraction procedure and the contribution of functional monomer.

The UV-laser was used in this thesis to initiate surface-grown MIP polymerization. The area of illumination of the laser was in this case kept as large as possible to cover a maximal fraction of the titanium substrate with MIP film. The laser is however an ideal tool to explore more complex patterns and graft multi-target arrays. For example grafting a MIP plane as well as a NIP plane on one substrate enables differential measurements, directly correcting for non-specific binding. Multi-target arrays would allow for the monitoring of concentration fluctuations of several targets simultaneously, which can give useful information about more complex chemical events or pathologies. The laser could ultimately be used to further exploit the option for miniaturization, contributing to the production of catheters or even edible sensors to allow for *in vivo* detection. Prior to *in vivo* measurements, sensors have to be tested using biological samples (e.g. blood, intestinal juices). When aiming to apply the histamine sensor in a catheter, this would mainly concern intestinal juices.

The results for surface initiated photoiniferter using xanthates looked highly

promising as the chemistry was determined to be successful. At this point, it looks like an unknown factor (until date) interferes with the silanization process. Literature further more makes, to the best of our knowledge, no report of great difficulties with the immobilization of trithiocarbonates (or xanthates). Much improved results and reproducibility might be obtained for performing these experiments in a more specialized environment for surface chemistry as these reactions are expected to be very sensitive for contamination. This means there are high expectations for the future development of such reactions. When developing surface initiated photoiniferter towards the production of surface-grown MIPs, functional monomers like acrylic acid are a logical next step. RAFT or iniferter are typically compatible with a vast library of monomers. This means the monomer pool for this specific reaction procedure can be easily expanded, which is of course only relevant after previously discussed issues are resolved.

The use of 2PP in combination with photo-mediated RDRPs is until date completely unexplored. Firstly, this means all different kind of RAFT agents can be tested and combined with all their respective compatible monomers. Secondly, the effect of different molecular weights for the macroRAFT can be assessed. Additionally, the use of only macroRAFT and thus no exogenous cross-linker can be tested. This would greatly improve the ability to post-modify the 3D structures as the amount of end-groups are maximized (being only dependent from the size of the macroRAFT). In that case bifunctional or multifunctional RAFT agents can be considered. Furthermore, biocompatibility and toxicity has to be thoroughly investigated in cell studies. This includes the effect of post-modification and mechanical properties, like porosity, on the cell behavior. Lastly, many different conjugation reactions can be explored, as the end-groups of the RAFT polymer can be chosen and fine-tuned according to the needs of the application.

The synthesized MBH particles are found to be biocompatible. A logical next step is to explore the possible conjugation reactions. This automatically includes the attachment of biomarkers or peptides, depending on the application. Furthermore, it would be interesting to push the size of the particles to its lower limits using different emulsion techniques or particle synthesis in continuous flow procedures. This would possibly ameliorate the dispersity of the particles size distribution. Additionally, synthesizing particles in flow would allow for a more straightforward upscaling of the synthesis procedure.

Publications

Scientific journals

G. Ramakers, C. D'Incal, M. Gagliardi, D. Molin, T. Junkers, *Synthesis of functional polymer particles from Morita-Baylis-Hillman polymerization*, *Macromol. Rapid Commun.* **2018**, 1800678.

G. Ramakers, A. Krivcov, V. Trouillet, A. Welle, H. Möbius, T. Junkers, *Organocatalyzed Photo-Atom Transfer Radical Polymerization of Methacrylic Acid in Continuous Flow and Surface Grafting*, *Macromol. Rapid Commun.* **2017**, 38, 1700423.

M. Conradi, G. Ramakers, T. Junkers, *UV-Induced [2+2] Grafting-To Reactions for Polymer Modification of Cellulose*, *Macromol. Rapid Commun.* **2016**, 37, 174–180.

J. Vandenberg, G. Ramakers, L. van Lokeren, G. van Assche, T. Junkers, *Synthesis of degradable multi-segmented polymers via Michael-addition thiol-ene step-growth polymerization*, *RSC Adv.* **2015**, 5, 81920–81932.

G. Ramakers, G. Wackers, V. Trouillet, A. Welle, P. Wagner, T. Junkers, *Laser-grafted Molecularly Imprinted Polymers for the Detection of Histamine From Organocatalyzed Atom Transfer Radical Polymerization*, submitted.

Conference poster contributions

G. Ramakers, J. Vandenberg, T. Junkers, *Synthesis of Biodegradable Polymers via Thiol-ene Click Polymerization*, Annual Meeting of the Belgian Polymer Group (BPG) **2015**, Houffalize, Belgium.

G. Ramakers, J. Vandenberg, T. Junkers, *Synthesis of biodegradable polymers via thiol-ene click polymerization*, Biomedica **2015**, Genk, Belgium.

G. Ramakers, T. Junkers, *New insights in a metal-free ATRP process*, Annual Meeting of the Belgian Polymer Group (BPG) **2016**, Hasselt, Belgium.

G. Ramakers, T. Junkers, *New insights in a metal-free ATRP process*, Interuniversity Attraction Poles (IAP) meeting **2016**, Liège, Belgium.

G. Ramakers, V. Trouillet, A. Welle, T. Junkers, *Exploring the Potential of metal-free ATRP*, Karlsruhe Nano Micro Facility (KNMF) User Meeting **2017**, Karlsruhe, Germany.

G. Ramakers, J. Laun, V. Trouillet, A. Welle, T. Junkers, *Exploring the Potential of metal-free ATRP*, Annual Meeting of the Belgian Polymer Group (BPG) **2017**, Houffalize, Belgium.

G. Ramakers, J. Laun, V. Trouillet, A. Welle, T. Junkers, *Exploring the Potential of metal-free ATRP*, Chemcys **2018**, Blankenberge, Belgium.

G. Ramakers, G. Wackers, V. Trouillet, A. Welle, P. Wagner, T. Junkers, *Optimizing MIP biosensors using surface-initiated and organocatalyzed photo-ATRP*, Annual Meeting of the Belgian Polymer Group (BPG) **2018**, Blankenberge, Belgium

Dankwoord

Afgelopen vier jaar waren onwaarschijnlijk. Al van sinds ik leerde lezen droomde ik ervan, naast enkele andere even onwaarschijnlijke dromen, om bij te dragen aan wetenschappelijk onderzoek. Het was een ambitie die echter pas tastbaar werd vanaf mijn bachelor thesis, waar ik mocht beginnen binnen de groep van Tanja. Na enkele maanden in het labo hoorden ik voor het eerst mijn naam en "doctoraat" in één zin. Ik stelde meteen mijn doelen bij toen ik besepte dat ik naar iets haalbaar streefde.

Het spreekt voor zich dat ik Tanja een enorme dank verschuldigd ben. Niet alleen vertrouwde ze mij in een doctoraatspositie, ook kreeg ik een chemisch onderwerp voorgeschoteld als iemand met een biomedische achtergrond. Tijdens onze eerste meeting omtrent het onderwerp vielen de woorden "a steep learning curve", woorden die mij herinnerde aan het feit dat niks vanzelf zou komen, het sporadisch falen vergoelijkte maar ook een blijvende motivatie waren. Tanja gaf verder het uitmuntend voorbeeld als wetenschapper, strevend naar correctheid en perfectie, maar ook bij haar dappere transitie waar ik enorm veel respect voor opbreng.

Of course, I also have to mention the experts from Germany, Alex for the ToF-SIMS measurements. Your "no mud, no glory" quote could've just as easily been used on the first page of this thesis. Vanessa, thanks for your many XPS measurements and Alex Krivcov many thanks for your AFM measurements. Good luck with your defense later this year.

Vervolgens ook bedankt aan Gideon en de groep van Prof. Patrick Wagner voor de impedantie metingen en het ontwikkelen van de sensor. Ook aan Gideon veel succes alvast met de verdediging!

Dankwoord

In het dagelijks werk kon ik altijd terugvallen op de collega's van PRD, bestaande uit onderstaande jolige groep. Allereerst zou ik graag de collega's die bij mij op het bureau hebben gezeten willen bedanken, namelijk Joachim en Benjamin. Beni, you were the perfect mentor during my first year. You lead by example concerning efficiency and planning, values that could be greatly improved in the beginning of my PhD. I also must thank you for the prank book you left behind. For the second part of my PhD, I could enjoy Jogi's company, the other "surface guy". Your ambition was contagious and I could always rely on you when I faced the limits of my knowledge. Thanks for being a walking chemistry book. Furthermore I really enjoyed how we shared the love for alcohol (it might be as bad as it sounds). You were, and still are, a great motivator, advisor and friend, which is something we all need from time to time. Het laatste jaar werd onze bureau vervolledigd door Maarten. Bedankt voor de bijdrage aan Chapter 4 en natuurlijk ook (vele) andere interessante discussies. Veel succes in Monash en blijven meeklappen op optredens! Dat ritmegevoel volgt wel ;).

Vervolgens zou ik graag mijn begeleiders (en later ook collega's) tijdens mijn bachelor en master thesis willen bedanken, namelijk Matthias en Joke. Het merendeel van mijn kennis heb ik opgedaan tijdens de stages, grotendeels vanwege mijn "uitmuntende" concentratievermogen tijdens de lessen.

En dan het team binnen het team, de helden van het unief, de eerste hulp, de stalen zenuwen van het GPC onderhoudsensemble. Matthias, Neomy, Joris en Jeroen. Druk verlagen? Geen probleem. Lampke fixen? Da's zeker! Tubing vervangen? Gisteren nog! Wel efkes aan Huub vragen. Heater high, pressure low (sorry boys).

Dan PRD-ers van 't hoger verdiep, Erika, de enthousiaste mede MIPper, Lowieke, de framboos van chemie. Merci voor de medewerking bij Chapter 5 en de vele ESI's samen met Joris. En Jeroen GPC Vrijzen, blijven naar Amenra luisteren daar wordt ge gelukkig van. Greg, Kirsten, Svieta (Svitlana), the Ukrainian sensation

en onze post-doc's Nok, Luk en Ya-Mi.

Dan natuurlijk ook de andere ex-PRDers: Evelien, Stephan (ik mis uw lab cleans) en Kayte. Tenslotte de lichting die naar Australië verhuisde, Drieske, ge waart een geweldige ontdekking als drummer, top kerel! Dan de immer onverstaanbare Axel-Laurenz, Jeroen DN en Joris. Natuurlijk heb ik ook enkele studenten onder mijn hoede gehad de afgelopen 4 jaar. Bedankt Senne, Jeroen DN, Jeroen L. Thomas, Joren en Emma (Team Resin) en Claudio (Chapter 6).

En dan de mannen en vrouwen van DSOS en heel OBPC. In het bijzonder de labgenoten Tom C., Jorne, Joris, Tom V., Mathias, Pieter voor de vele vragen en Raphael. Raphael bedankt om mij te tonen welke chemicaliën welke kleur vlam geven. Ook bedankt voor alle greased-out warhammer quotes op mijn trekkast. Ja ze staan daar nog steeds. Alleen geen glaswerk meer poetsen (nvdr). Ook bedankt aan Wouter VG, Jeroen DN (die daar toch al woonde) en Jogi om af en toe tot 22u te blijven zitten tot ik klaar was met mijn experimenten (regels zijn regels he).

Niet te vergeten, de NMR groep van Peter, Gunther en Koen. De werkdruk die die mannen aankunnen is ongezien. De mensen van didactiek Eugène, Hilde en Iris. Ik hoop voor jullie dat dat MIP practicum wordt opgedoekt. Gelukkig is groen nog een mooie kleur.

Dan natuurlijk mijn band buddies, waar ik af en toe omwille van deadlines repetities voor moest laten schieten. Bart, Dries, Jeroen, Ronald, Marnik, Brent, Niels, Staf, Jeff, Michiel en Sandro. De weirdo's van koalapanda Jeff, Bart, Marlies en Lisa. Jeff in het bijzonder merci om mij geduldig bij te staan m.b.t. de layout van de thesis en Indesign.

En dan nog mijn familie, Ma, Pa en Marieke. Het spreekt voor zich dat dit een

Dankwoord

onmogelijk bedoeling was geworden zonder jullie steun. En tenslotte Lisa, mijn vriendin, die dit allemaal al moet aanzien sinds de middelbare school. Lowie begrijpt nog altijd niet waarom jij nog met mij wilt samen zijn. Maar ik ben gewoon een feest. Zonder uw geduld, steun en (jawel) troostende woorden weet ik niet waar ik beland zou zijn. Bedankt voor de reality checks en de motivatie.